

Optimal Energy Management for Hybrid Electric Vehicles

DISSERTATION

to attain the academic degree

”DOKTOR DER TECHNISCHEN WISSENSCHAFTEN”

from



Institute of Electrical Measurement and Measurement Signal Processing
Inffeldgasse 23/II, 8010 Graz, Austria



supervisor: O. Univ.-Prof. Dipl.-Ing. Dr.techn. Georg Brasseur
co-supervisor: O. Univ.-Prof. Dipl.-Ing. Dr.techn. Kurt Schlacher
co-supervisor: Ao.Univ.-Prof. Dipl.-Ing. Dr.techn. Christian Magele

submitted by: Dipl.-Ing. Johannes Fuchs, BSc.

Graz, November 2016

Eidesstattliche Erklärung

Ich erkläre an Eides statt, dass ich die vorliegende Arbeit selbstständig verfasst, andere als die angegebenen Quellen/Hilfsmittel nicht benutzt und die den benutzten Quellen wörtlich und inhaltlich entnommene Stellen als solche kenntlich gemacht habe.

Graz, am _____

(Unterschrift)

Statutory Declaration

I declare that I have authored this thesis independently, that I have not used other than the declared sources / resources, and that I have explicitly marked all material which has been quoted either literally or by content from the used sources.

date

(signature)

Acknowledgement

I would like to express my gratitude to my supervisor Univ.-Prof. Dipl.-Ing. Dr.techn. Georg Brasseur for his guidance through the doctoral program as well as for his inputs and the given academic freedom.

Further, I thank Univ.-Prof. Dipl.-Ing. Dr.techn. Kurt Schlacher and Ao. Univ.-Prof. Dipl. Ing. Dr.techn. Christian Magele for accepting to be the co-examiners of my thesis.

I also would like to thank all colleagues of the *Institute of Electrical Measurement and Measurement Signal Processing* and the *Virtual Vehicle Competence Center*. A special thank goes to Dr. tech. Bernhard Schweighofer, Dr. tech. Hannes Wegleiter and Dr. tech. Gerald Kelz.

Additionally, I want to thank the 'COMET K2 Forschungsförderungs-Programm' of the Austrian Federal Ministry for Transport, Innovation and Technology (BMVIT), the Austrian Federal Ministry of Economics and Labour (BMWA), Österreichische Forschungsförderungsgesellschaft mbH (FFG), Das Land Steiermark, and Steirische Wirtschaftsförderung (SFG) for their financial support.

Finally, a big thank goes to my family and friends for their help and support.

Graz, November 2016

Johannes Fuchs

Abstract

The emission limits of vehicles have become stricter and stricter over the past years and have caused major challenges in the vehicle industry. Beside the improvements of conventional vehicles (CVs), alternative vehicle concepts such as hybrid electric vehicles (HEVs) or electric vehicles (EVs) have been established on the market. As the performance of EVs is still limited due to the low energy densities of the electrical energy storage, HEVs have gained more relevance in the last years. In contrast to CVs, HEVs contain at least two distinct energy sources, which are commonly represented by means of an internal combustion engine (ICE) and a battery. In order to exploit the benefits of HEVs like the recuperation of kinetic energy or shifting of operating points, an appropriate operating strategy is necessary. Furthermore, the scaling of components such as energy storages and energy sources represents an important task.

In the scope of this thesis, novel methodologies for calculating optimal operating strategies and component sizes are developed in the field of HEVs. The first part describes approaches that take the operating and life cycle costs of HEVs into account. For this purpose, not only the fuel costs but also costs due to battery aging and brake pad wear are included into the optimization problem. In addition to cost-optimizing operating strategies, further approaches are devised to consider thermal component limits as well as to reduce the number of start-stop operations of the ICE.

In order to obtain optimal operating strategies, the mathematical method of deterministic dynamic programming (DDP) is used in this work. The main benefit of this method is that it always provides the global optimum but unfortunately, calculation becomes slow for multidimensional state spaces. In order to reduce the calculation effort, a modified version of DDP based on iterative dynamic programming is applied. Beside the calculation of optimal operating strategies, DDP can also be used to determine optimal component sizes. The second part of this thesis describes methodologies for the optimal sizing of energy sources as well as electric traction motors.

All the methodologies developed in this thesis are demonstrated by means of simulation studies based on a model of a series hybrid bus. Due to their general formulation, the approaches can also be used in connection with other topologies and classes of HEVs.

Kurzfassung

Die im Laufe der Zeit strenger gewordenen Grenzwerte für Fahrzeugemissionen haben zu großen Veränderungen in der Fahrzeugindustrie geführt. Aus diesem Grund haben sich neben den Verbesserungen von konventionellen Fahrzeugen weitere, alternative Fahrzeugkonzepte wie Hybridelektrofahrzeuge oder Elektrofahrzeuge am Markt etabliert. Da jedoch die Leistungsfähigkeit von rein elektrischen Fahrzeugen aufgrund der geringen Energiedichten des Energiespeichers eingeschränkt ist, haben Hybridelektrofahrzeuge in den letzten Jahren zunehmend an Bedeutung gewonnen. Im Gegensatz zu konventionellen Fahrzeugen beinhaltet dieses Fahrzeugkonzept mindestens zwei unterschiedliche Energiewandler, welche typischerweise durch eine Kombination aus einer Verbrennungskraftmaschine und einer Batterie repräsentiert werden. Um die Vorteile von Hybridelektrofahrzeugen wie Rekuperation von Bremsenergie oder Lastpunktverschiebung nutzen zu können, ist eine passende Betriebsstrategie notwendig. Darüber hinaus stellt die Auslegung von Komponenten wie z.B. der Energiespeicher oder der Energiewandler eine wichtige Aufgabe dar.

Im Rahmen dieser Dissertation werden neuartige Methodiken für die Berechnung von optimalen Betriebsstrategien sowie für die Komponentenauslegung im Bereich der Hybridelektrofahrzeuge entwickelt. Der erste Teil beschreibt Ansätze für Betriebsstrategien, welche die Berücksichtigung von laufenden Kosten sowie Lebenszykluskosten erlauben. Dabei werden im Optimierungsproblem nicht nur die Treibstoffkosten, sondern auch die Kosten aufgrund von Batteriealterung und Bremsverschleiß in Betracht gezogen. Zusätzlich zu den kostenoptimalen Ansätzen werden weitere Betriebsstrategien beschrieben, welche thermische Komponentengrenzen einhalten sowie die Anzahl der Start- und Stoppvorgänge der Verbrennungskraftmaschine reduzieren.

Für die Berechnung der optimalen Betriebsstrategien wird in dieser Arbeit die mathematische Methode der deterministischen dynamischen Programmierung verwendet. Ein wichtiger Vorteil dieses Algorithmus liegt darin, dass immer das globale Optimum berechnet wird. Nachteilig wirken sich mehrdimensionale Zustandsräume aus, welche zu langsamen Rechenzeiten führen. Um den Rechenaufwand zu reduzieren, wird daher eine modifizierte Version der deterministischen dynamischen Programmierung auf Basis eines iterativen Ansatzes eingesetzt. Neben der Berechnung von optimalen Betriebsstrategien kann die deterministische dynamische Programmierung des Weiteren für die Bestimmung von optimalen Komponentenauslegungen verwendet werden. Der zweite Teil dieser Arbeit beschreibt Methodiken für die optimale Dimensionierung von Energiewandlern und elektrischen Antriebsmaschinen.

Die in dieser Arbeit entwickelten Methodiken werden anhand von Simulationsstudien basierend auf einem Modell eines seriellen Hybridbusses demonstriert. Die allgemeine Formulierung der Ansätze erlaubt jedoch auch die Verwendung von anderen Topologien und Hybridfahrzeugklassen.

Contents

1. Introduction	1
1.1. Motivation	1
1.2. Objectives	3
1.3. Contributions	3
1.4. Thesis Outline	4
2. Hybrid Electric Vehicles	5
2.1. Overview of Energy Storages	6
2.2. Architectures	8
2.2.1. Series Hybrid Electric Vehicles	8
2.2.2. Parallel Hybrid Electric Vehicles	9
2.2.3. Power-split Hybrid Electric Vehicles	10
2.2.4. Further Variants and Modifications	10
2.3. Classifications	10
2.3.1. Micro Hybrid	12
2.3.2. Mild Hybrid	12
2.3.3. Full Hybrid	12
2.3.4. Plug-in Hybrid	13
2.4. Summary	13
3. Operating Strategies for Hybrid Electric Vehicles	14
3.1. Rule-based Strategies	16
3.1.1. Deterministic Concepts	17
3.1.2. Fuzzy Concepts	19
3.1.3. Concepts for Plug-in Hybrid Electric Vehicles	20
3.2. Optimization-based Strategies	21
3.2.1. Fundamentals	21
3.2.2. Methods for Optimal Control	23
3.3. From Optimal to Real-time Strategies	27
3.3.1. Equivalent Consumption Minimization Strategy	27
3.3.2. Model Predictive Control	32
3.3.3. Use of Dynamic Programming Results	33
3.4. Summary	33
4. Dynamic Programming for Hybrid Electric Vehicles	34
4.1. Deterministic Dynamic Programming	36
4.1.1. Discretization and Interpolation	36
4.1.2. Modifications of Dynamic Programming	37
4.2. Stochastic Dynamic Programming	40
4.3. Summary	41

5. Model of a Hybrid Electric Bus	42
5.1. Vehicle	42
5.1.1. Model description	43
5.1.2. Characteristics	43
5.2. Tire and Gear Box	43
5.2.1. Model description	43
5.2.2. Characteristics	44
5.3. Electric Motor	44
5.3.1. Model description	44
5.3.2. Characteristics	45
5.4. Battery	46
5.4.1. Model description	46
5.4.2. Characteristics	46
5.5. Power Electronics	47
5.5.1. Model description	47
5.5.2. Characteristics	48
5.6. Engine-Generator Unit	48
5.6.1. Model description	48
5.6.2. Characteristics	49
5.7. Summary	49
6. Approaches for Optimal Energy Management	50
6.1. Reference Simulations	52
6.2. Sizing of Energy Sources	57
6.2.1. Methodology	57
6.2.2. Results	58
6.3. Sizing of Electric Motors	60
6.3.1. Methodology	60
6.3.2. Results based on a Battery	66
6.3.3. Results based on a Supercap	69
6.4. Cost-optimal Operating Strategies	72
6.4.1. Cyclic Battery Aging	73
6.4.2. Calendric Battery Aging	79
6.4.3. Brake Wear	82
6.5. Operating Strategies Including Thermal Effects	87
6.5.1. Methodology	87
6.5.2. Results	89
6.6. Operating Strategies for the Engine-Generator Unit	92
6.6.1. Methodology	92
6.6.2. Results	95
6.7. Summary	96
7. Summary and Conclusion	98
A. Rainflow Counting Algorithm	100
B. Mathematical Derivations	101
C. Simulation Results	105

D. Driving Cycles	113
E. List of Abbreviations	114
F. List of Symbols	115
Bibliography	119

List of Figures

1.1. Fleet average type-approval CO_2 emissions.	1
2.1. Forces acting on a simplified vehicle model.	5
2.2. Ragone-chart.	7
2.3. Overview of general topologies of HEVs.	9
2.4. Hybridization ratio of common hybrid vehicles.	11
3.1. Energies and power flows in HEVs.	15
3.2. Examples for rule-based operating strategies.	18
3.3. Examples for typical membership functions.	19
3.4. CDCS strategy for plug-in HEVs.	20
3.5. Illustration of the optimal state trajectory.	22
3.6. Cases of fuel equivalence.	28
3.7. Illustration of the equivalence factor estimation.	30
3.8. Simplified structure of a typical adaptive ECMS-Controller.	31
3.9. Two terms for an adaptive ECMS.	32
4.1. DP example: Finding the shortest path.	35
4.2. One-dimensional calculation step.	37
4.3. Two-dimensional calculation step.	38
4.4. Principle of IDP.	39
4.5. Boundary-line method.	39
5.1. Volvo 7700 hybrid bus.	42
5.2. Efficiencies and power loss of the EM.	45
5.3. Equivalent circuit model of the battery.	46
5.4. Discharge and charge curves of the battery.	47
5.5. Efficiency of the power electronics.	48
5.6. Efficiency of the EGU.	49
6.1. Simplified model of a series hybrid bus.	51
6.2. Convergence of the state of charge trajectories.	54
6.3. State of charge trajectories of different iterations.	55
6.4. Histogram of EGU efficiencies.	55
6.5. Minimum EGU power depending on the battery capacity.	58
6.6. Minimum fuel consumption depending on the battery capacity.	59
6.7. Efficiencies of the scaled EM.	61
6.8. Equivalent circuit of an EM.	61
6.9. Overloading and voltage dependencies of the EM.	62
6.10. Acceleration scenario of the bus.	63
6.11. Thermal model of the EM.	64
6.12. Power loss of the EM.	65

6.13. Temperatures of the EM.	67
6.14. Optimal sizes of the EMs.	68
6.15. Fuel consumption depending on the second gear.	68
6.16. Open-circuit voltage of the supercap.	70
6.17. Overview of the methodology.	74
6.18. Model used to describe cyclic battery aging.	75
6.19. Evaluation of a state of charge trajectory.	76
6.20. Influence of the weighting factor β	78
6.21. Variable fuel costs and battery costs over β	79
6.22. Minimum operating costs depending on the battery capacity.	80
6.23. Comparison of life cycle costs.	83
6.24. Brake model.	84
6.25. Internal battery resistance depending on the temperature.	88
6.26. Thermal battery model.	89
6.27. Cooling power and battery temperature for different driving cycles.	91
6.28. Approaches to consider start-stop operations of the engine.	93
6.29. Number of engine starts depending on the idle time.	95
6.30. Fuel consumption depending on the idle time.	96

List of Tables

2.1. Comparison of different HEV classifications.	11
5.1. List of vehicle parameters.	43
5.2. List of gear box and tire parameters.	44
5.3. List of EM parameters.	45
5.4. List of battery pack parameters.	47
5.5. List of power electronics parameters.	48
5.6. List of engine-generator unit parameters.	49
6.1. Characteristics of the driving cycles.	52
6.2. Variation of the configuration of a typical dynamic program.	56
6.3. List of characteristics of the EM.	62
6.4. Thermal parameters of the EM.	65
6.5. Comparison of EMs on the basis of a battery.	67
6.6. Parameters of the supercap.	69
6.7. Comparison of EMs on the basis of a supercap.	70
6.8. Comparison of EMs on the basis of optimum supercaps.	71
6.9. Comparison of cyclic battery aging.	77
6.10. Calendric battery aging.	81
6.11. Share of battery aging effects.	82
6.12. Total brake energy demands.	85
6.13. Share of operating and life cycle costs (1 €/liter and 500 €/kWh).	86
6.14. Share of operating and life cycle costs (2 €/liter and 200 €/kWh).	86
6.15. Results of parameter studies.	90
6.16. Transitions between the states of the state variable x_{ice}	94

1. Introduction

1.1. Motivation

Global economic growth in combination with an increasing consumption of fossil fuels has led to negative impacts on the environment. In order to reduce emissions and to improve sustainability, limits for all energy consuming sectors have been enacted by law. In the field of mobility and transportation, maximum values of vehicle emissions like NO_x , hydrocarbons or particles have been introduced. Furthermore, mandatory fleet average CO_2 standards have been defined for all manufactures. The limits described have become stricter over the past years for all types of vehicles and have caused major challenges in the vehicle industry. Beside the improvements of conventional vehicles, new vehicle concepts have been introduced into the market to fulfill the defined limits.

Typical CO_2 standards defined by legislation are depicted in Figure 1.1. The corresponding values for 2015 and 2020 which are defined by $130 \text{ g } CO_2/\text{km}$ and $95 \text{ g } CO_2/\text{km}$ are equivalent to $4.9 \text{ lit.}/100 \text{ km}$ and $3.58 \text{ lit.}/100 \text{ km}$ diesel fuel, respectively. In addition, the illustration shows the fleet average type-approval CO_2 emissions of newly registered light-duty vehicles in Germany over the past years. As only newly registered vehicles are considered, a delayed trend occurs in reality. Due to this circumstance and the increasing number of vehicles, the CO_2 emissions are still increasing [23].

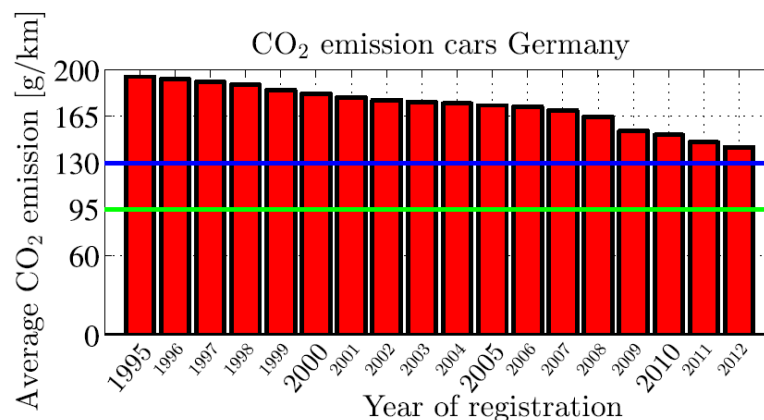


Figure 1.1.: Fleet average type-approval CO_2 emissions of newly registered light-duty vehicles during a series of years in Germany. The blue and green levels represent the target values for 2015 and 2020, respectively [23].

In order to avoid expensive penalties for exceeding emission target values, vehicle manufacturers aim to introduce novel vehicle concepts instead of conventional vehicles. These alternative vehicle types include for example hybrid vehicles or electric vehicles. In case of electric vehicles, it is assumed that this vehicle type offers the best future concept in terms of efficiency

and emissions. However, due to immature battery technology the performance of an electric vehicle is very limited. Hence, at least for the next few years hybrid vehicles will provide a practical alternative to the current vast number of conventional vehicles [115].

Conventional vehicles only use one energy source which is mostly an internal combustion engine (ICE) in combination with a fuel tank. In contrast, hybrid vehicles contain at least two distinct energy sources. A more general definition of this vehicle type is provided by the International Electrotechnical Commission [42]:

"A hybrid vehicle is defined as one in which propulsion energy, during specified operational missions, is available from two or more kinds or types of energy stores, sources, or converters."

Based on hybrid vehicle concepts, there are a variety of possible combinations between energy sources and energy storages. The main advantages of hybrid vehicles are summarized as follows:

- Recuperation of kinetic energy,
- Shifting of operating points of the ICE,
- Downsizing of the primary energy source (ICE),
- Reduction of idle losses through start-stop of the primary energy source (ICE),
- Zero-emission driving.

In contrast, the hybridization of a vehicle may lead to drawbacks like increased vehicle weight, higher costs and higher complexity.

The typical configuration is represented by the use of an ICE combined with an electric motor (EM). This type of hybrid vehicle belongs to the class of hybrid electric vehicles. Today, the energy storage used in addition to the fuel tank is usually a battery but other concepts with supercapacitors are also common. Due to this circumstance, this thesis focuses on hybrid electric vehicles with a battery as energy storage.

To exploit the advantages of hybrid electric vehicles, an appropriate control strategy for the energy management is necessary. The main task of such operating strategies is to minimize a cost function $L(\cdot)$ which is generally given by fuel consumption f_c over time. By means of optimization results, the power-split u_s between the energy sources is determined for occurring driving profiles. In addition, component limits such as the maximum power of the EM $P_{EM,max}$ or the minimum energy content of the battery $E_{BAT,min}$ have to be considered to prevent component damages and enhance the overall life span. Operating strategies of hybrid electric vehicles are generally classified into two categories, namely rule-based and optimal control concepts [23]. Rule-based strategies are especially suitable for real-time applications whereas optimal strategies can be used for component sizing as well as benchmarking.

In recent years several researches have been conducted to improve operating strategies in hybrid electric vehicles [83, 116, 90, 47, 38]. However, there are still challenges in terms of introducing cost functions $L(\cdot)$ that do not only consider the fuel consumption f_c . Minimizing the operating costs of hybrid electric vehicles would be an example therefore. This thesis focuses on the above mentioned task and provides novel approaches in the field of optimal energy management in hybrid electric vehicles.

1.2. Objectives

Besides the sizing of components, the use of an appropriate operating strategy is essential to reduce fuel consumption f_c of hybrid electric vehicles. In order to assess the applied operating strategy for a given vehicle configuration, the calculation of a globally optimal reference is of central interest. For this purpose, the energy management in hybrid electric vehicles is converted into an optimization problem which can be solved in different ways. Depending on the applied optimization algorithm, several constraints in terms of cost functions $L(\cdot)$ and modeling of components need to be taken into account. In order to calculate the optimal operating strategy the first approaches were based on linear programming (LP) [104]. Furthermore, it has been shown that quadratic programming (QP) [50] as well as the maximum principle of Pontryagin (PMP) which originates from optimal control theory can be applied [24, 47]. The mentioned algorithms are restricted to convex functions and models which can cause oversimplifications in some applications. To avoid these restrictions the use of dynamic programming (DP) in several variants has been recommended in later work [61, 44].

In related work [53, 101, 3, 92, 23, 38] the optimal operating strategies calculated by means of different algorithms were compared. Furthermore, the deviations between heuristic and optimal operating strategies were evaluated in detail. As these comparisons are assumed to be well-understood, this thesis focuses on other objectives which are described in the following.

The usual goal of an optimal energy management strategy in hybrid electric vehicles is to minimize fuel consumption f_c . In contrast, there are applications such as freight traffic where minimizing the operating or life cycle costs instead of fuel consumption f_c is more important. In this thesis, the objectives are defined by developing methodologies for obtaining optimal operating costs of hybrid electric vehicles. Other tasks are given by means of the integration of thermal effects or the number of start-stop operations into the optimization problem. Whereas the objectives described focus on operating strategies, the component sizing of hybrid electric vehicles depicts another challenge. For this purpose, further methodologies should be evolved within this thesis.

1.3. Contributions

The use of an algorithm that calculates the global optimum is essential to obtain the optimal operating strategy as well as to compare different vehicle and component variations in a "fair" way. To solve the corresponding optimization problems, deterministic dynamic programming (DDP) was finally chosen.

The contributions of this thesis are divided into two parts. The first part provides novel approaches in terms of optimal operating strategies of hybrid electric vehicles. The approaches developed consider cost-optimal operating strategies leading to minimum operating or life cycle costs. In order to determine these costs, the fuel consumption f_c as well as battery aging and brake pad wear are considered. Further approaches include critical component temperatures or the number of start-stop operations of the ICE into the optimization problem. The second part describes methodologies for the optimal sizing of energy sources and electric traction motors.

To summarize, this thesis provides novel approaches at the intersection of DDP and the modeling of hybrid electric vehicles. Parts of corresponding results have been published and can be found in [34, 35].

1.4. Thesis Outline

Chapter 2 gives a short introduction to hybrid vehicles and describes rechargeable energy storages, possible architectures as well as common classifications of this vehicle type.

In Chapter 3, a review of operating strategies for hybrid electric vehicles is shown and several examples for heuristic and optimal strategies are presented in detail. Since this thesis focuses on optimal operating strategies, the method of dynamic programming was chosen to obtain globally optimal results.

To get an insight into the algorithm, different variants and practical modifications applied in this thesis are shown in Chapter 4.

Chapter 5 presents a model of a hybrid electric bus which is used to demonstrate the methodologies of this thesis. For this purpose, the characteristics and parameters are depicted for several component models.

Chapter 6 represents the central part of this thesis. It describes the novel methodologies developed by the author as well as corresponding simulation results. These methodologies deal with optimal component sizing as well as optimal operating strategies in the field of hybrid electric vehicles.

The final Chapter 7 provides a conclusion of this thesis together with a short outlook.

2. Hybrid Electric Vehicles

This chapter gives an introduction to hybrid electric vehicles (HEVs) and outlines possible configurations, architectures and characteristics of this vehicle type. Before focusing on HEVs, a general description of the power at the wheels P_W for all vehicle types is introduced to analyze how energy consumption e_c can be reduced.

Figure 2.1 shows a schematic representation of forces acting on a simplified vehicle model.

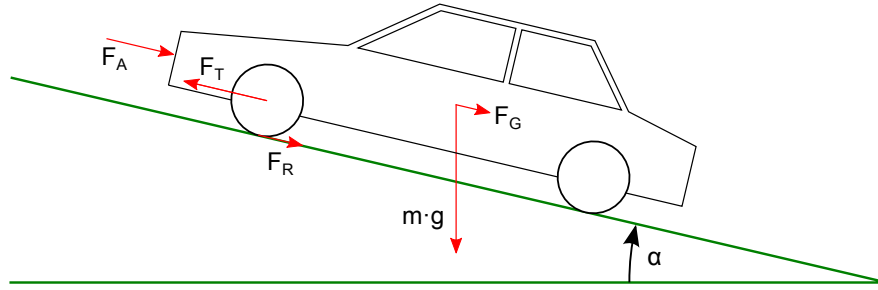


Figure 2.1.: Forces acting on a simplified vehicle model in order to describe the longitudinal vehicle dynamics. F_T represents the traction force at the wheels, F_G the force caused by gravity and gradients, F_A the aerodynamic friction and F_R the rolling friction.

By means of the forces depicted in Figure 2.1 the longitudinal vehicle dynamics can be derived as follows

$$m \cdot \dot{v} = F_T - (F_G + F_R + F_A), \quad (2.1)$$

where m represents the vehicle mass, \dot{v} the vehicle acceleration, F_T the traction force at the wheels, F_G the force caused by gravity and gradients, F_R the rolling friction and F_A the aerodynamic friction.

The forces in Equation 2.1 can be described in more detail by means of

$$F_G = m \cdot g \cdot \sin \alpha, \quad (2.2)$$

$$F_R = f_r \cdot m \cdot g \cdot \cos \alpha, \quad (2.3)$$

$$F_A = \frac{1}{2} \cdot \rho \cdot c_w \cdot A \cdot v^2, \quad (2.4)$$

where g represents the gravitational constant, α the road angle, f_r a coefficient for the rolling resistance, ρ the air density, c_w the drag coefficient, A the frontal area and v the vehicle velocity. Multiplying Equation 2.4 by the velocity v leads to the power at the wheels

$$P_W = \underbrace{m \cdot \dot{v} \cdot v}_{(1)} + \underbrace{m \cdot g \cdot \sin \alpha \cdot v}_{(2)} + \underbrace{f_r \cdot m \cdot g \cdot \cos \alpha \cdot v}_{(3)} + \underbrace{\frac{1}{2} \cdot \rho \cdot c_w \cdot A \cdot v^3}_{(4)}. \quad (2.5)$$

For simplicity, Equation 2.5 neglects a possible energy consumption e_c of auxiliary devices (AUX) like air condition and alternator. The terms contributing to the power at the wheels P_W can be distinguished by the following four parts:

- (1) Inertial power in order to describe the power to accelerate and decelerate the vehicle which is also equivalent to the change of kinetic vehicle energy.
- (2) Power to cope with changes of the potential vehicle energy resulting from gradients along a route.
- (3) Power to cope with rolling losses,
- (4) Power to cope with aerodynamic losses.

Equation 2.5 provides several approaches on how to reduce the required power at the wheels P_W in order to improve fuel economy. For example, the reduction of vehicle mass m as well as a lower rolling resistance f_r due to advanced tires and tire conditions lead to lower fuel consumption f_c . Furthermore, a reduced product of air drag coefficient c_w and frontal area A by means of an enhanced vehicle design contributes to an overall lower energy consumption e_c . In addition to modified vehicle parameters, the driving behavior also influences the power demand P_{DEM} . The driver can significantly reduce the energy consumption e_c by means of lower velocities v and accelerations \dot{v} . These mentioned improvements are described from a general point of view and hold for all types of vehicles.

In a further step, negative power demands P_{DEM} representing the braking case (power at the wheels $P_W < 0$) are analyzed. Conventional vehicles (CVs) with mechanical brakes convert braking energy into heat and are not able to recuperate energy. In contrast, hybrid vehicles (HVs) allow to store braking energy by means of one or more additional energy storages. The recuperated energy can be re-used in the propulsion case (power at the wheels $P_W > 0$) which significantly contributes to higher efficiencies η . For example, the hybridization of urban buses allows to reduce fuel consumption f_c by up to 30% [64, 14]. Beside other advantages which are itemized in Section 1.1, the recuperation of braking energy represents an important benefit of HVs. General applications with a high recuperation potential are driving scenarios with fast-changing velocities or steep up and downhill gradients.

As stated before, HVs contain at least two distinct on-board energy types with corresponding energy converters. There are several combinations of energy sources possible but in many cases the primary energy source is an ICE combined with a fuel tank. The choice of the second energy storage strongly depends on its application but mostly a battery fulfills the requirements. More sophisticated concepts may use more than two energy storages to exploit their advantages. Further HV concepts and possible energy storages in automotive applications are described in the next section.

2.1. Overview of Energy Storages

Beside the usually used fuel tank, HVs contain a second energy storage to allow recuperation of braking energy. The main characteristics of such devices are represented by energy density, power density, costs and safety issues. In special applications the volumetric energy and power density or the life span define further constraints.

Different energy storages are often compared in terms of energy and power densities leading to the well-known Ragone-chart. The energy and power densities of energy storages are

mainly influenced by means of corresponding operating points and losses, respectively. Thus, it is important to specify typical storage efficiencies η . This extension allows to exclude theoretical limits in terms of energy and power densities which are not usable in practical applications. Figure 2.2 depicts the Ragone-chart of common energy storages for automotive applications. The diagram considers an one-way storage efficiency η of 90% and is based on data sheets of the companies A123, Skeleton Technologies, Yunasko, Saft, Altair Nano, Panasonic, Sanyo, Kokam, Varta, Wima, Epcos, Nesscap, Maxwell, Compact Dynamics, Williams Hybrid Power, and CCM. Furthermore, the grey lines depict theoretical time spans in which the energy storage is fully charged or discharged. Since no thermal limits are taken into account in that case, significantly higher values of charge and discharge times are needed in "real life" to avoid overheating of the energy storage.

As can be seen from the chart, batteries provide an appropriate trade-off between energy and power density. More details, further comparisons and requirements of energy storages can be found in [45, 18, 52, 63, 78].

Due to relatively high power and energy densities, HVs generally contain beside the ICE a battery as second energy storage and one or more electric motors (EMs) as energy converter. Since the rechargeable energy is stored electrically, this type of HV is referred to as hybrid electric vehicle (HEV). Another concept for HEVs is given by the use of supercapacitors instead of batteries. This configuration is suitable for applications where low energy and high power requirements need to be fulfilled.

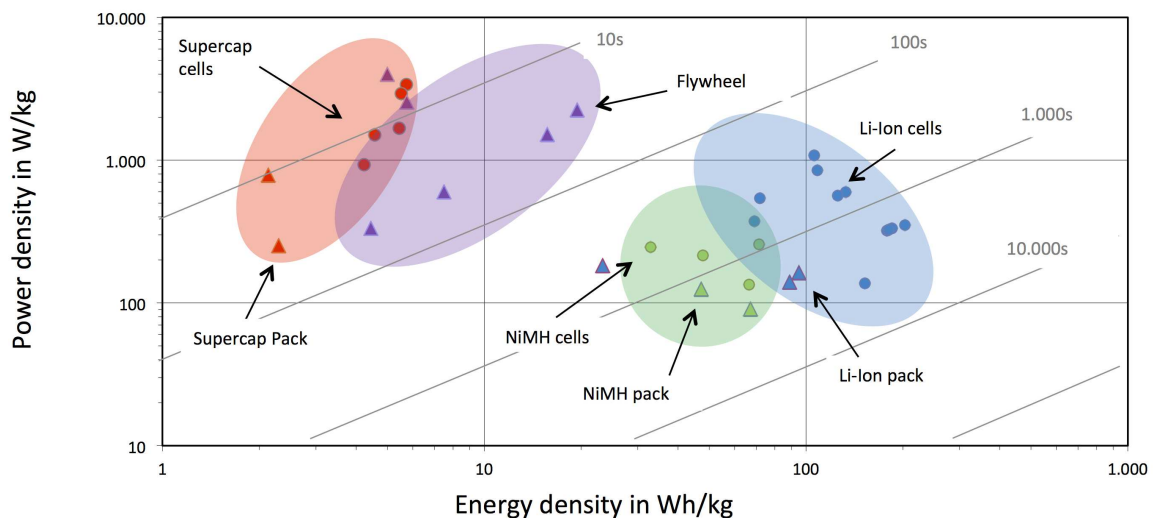


Figure 2.2.: Gravimetric Ragone-chart (at an one-way storage efficiency η of 90%) [114]. Blue: Li-Ion cells and modules, green: NiMH cells and modules, red: supercapacitor cells und modules, purple: flywheel modules. The grey lines depict time constants which are obtained by dividing the energy density by the power density. These time constants represent theoretical time spans in which the energy storage is fully charged or discharged. Since no thermal limits are taken into account in that case, significantly higher values of charge and discharge times are needed in "real life" to avoid overheating of the energy storage.

In practice, a few buses in public transport have been equipped with supercapacitors (e.g. [29, 111]) but this configuration is still rare due to the relatively high costs and space [82]. In addition to the hybrid vehicle configurations with batteries or supercapacitors rather non-

typical concepts for the second energy storage and corresponding energy converter of HVs can be designed as shown in [38]:

- Flywheel and electric motor (EM),
- Continuously variable transmission (CVT) and flywheel,
- CVT and torsion spring,
- Pneumatic pump/motor and accumulator,
- Hydraulic pump/motor and gas-filled accumulator,
- Superconductor coil and EM.

The following sections restrict the various configurations of HVs and focus on HEVs. Since nowadays the majority of all HEVs contains a battery as second energy storage, this hybrid configuration is used in the following.

2.2. Architectures

This section briefly describes and compares different architectures of HEVs. As stated in Section 2.1 the focus is put on HEVs that use an ICE as the main energy source and a battery as additional energy storage.

In general, there exist three different standard categories which are

- Series HEVs,
- Parallel HEVs,
- Power-split HEVs.

The corresponding illustrations of these architectures are depicted in Figures 2.3(a), 2.3(b), and 2.3(c).

2.2.1. Series Hybrid Electric Vehicles

In series HEVs the vehicle is exclusively propelled electrically. Thus, there is no direct mechanical connection between the ICE and the powertrain. The architecture of a series HEV can be described as a pure electric topology with an additional energy source. To convert the mechanical power of the ICE into electrical power a generator with corresponding power electronics (PE) is needed. The combination of ICE and generator is often denoted by an engine-generator unit (EGU) or auxiliary power unit (APU), and can be used for vehicle propulsion or recharging the battery. The mechanical decoupling of the generator unit allows its flexible positioning inside the vehicle. Furthermore, inefficient operating points can be avoided since the rotational speed of the ICE does not depend on the vehicle velocity v . In many applications, components of the conventional drive train such as clutch and gear box can be omitted.

In case of positive traction power an additional degree of freedom is given by the power-split u_s between EGU and battery. Depending on the operating strategy, the EM operates

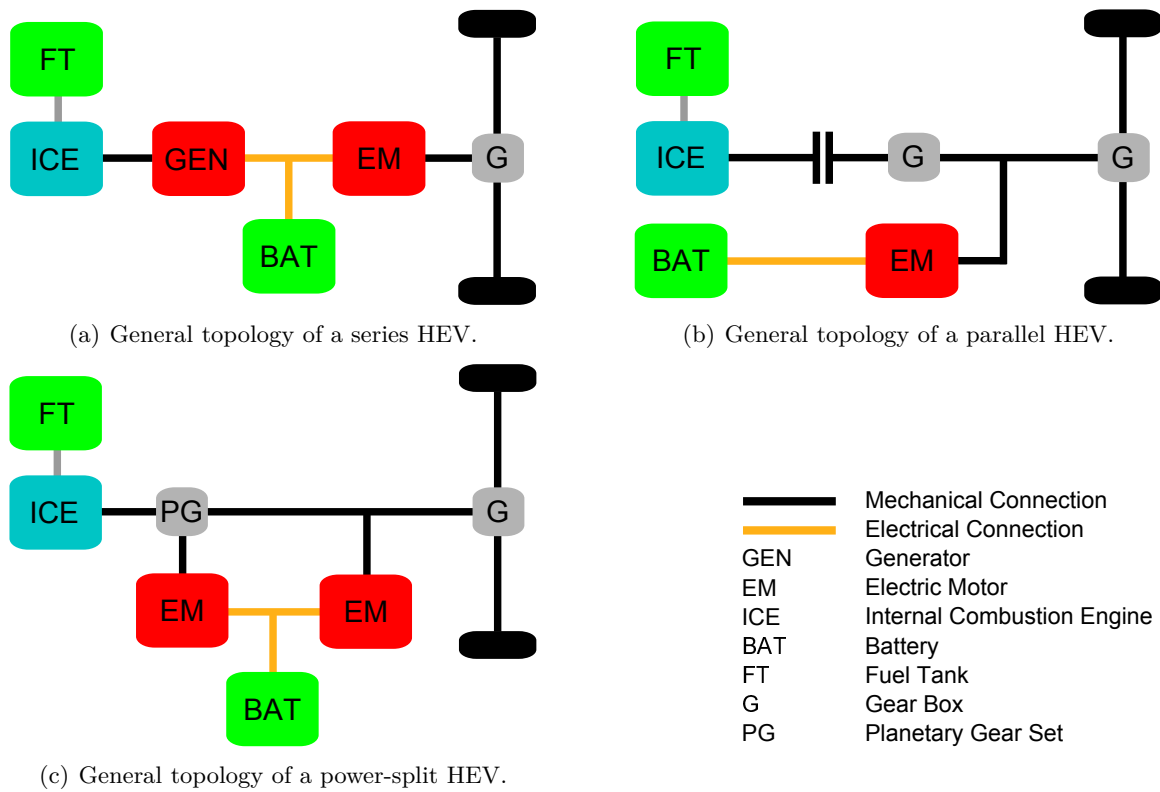


Figure 2.3.: Overview of general topologies of HEVs.

as generator in the braking case and the battery is used to store recuperation energy. One disadvantage of this architecture is the additional energy conversion: Instead of a direct mechanical connection between the ICE and the powertrain, two energy conversions are performed by means of a generator and EM, which may lead to overall lower efficiencies η . Further drawbacks arise from the generator, which leads to a higher vehicle mass and costs compared to a parallel architecture.

2.2.2. Parallel Hybrid Electric Vehicles

In parallel HEVs, the vehicle is propelled mechanically. The parallel architecture represents an extension of the topology of CVs and uses an EM as additional energy source. In contrast to series HEVs, there is a direct mechanical connection between ICE and powertrain which leads to a lower flexibility in terms of component positioning. Furthermore, the integration of components such as clutch and gear box is necessary. Due to the mechanical connection operating points of the ICE depend on vehicle velocity v . This circumstance does not allow to avoid operating points with poor efficiency η . However, the combination of EM and ICE allows to shift load points in regions with better efficiencies η . In parallel HEVs the ICE and EM can supply the propulsion power either alone or in combination. This fact leads to an additional degree of freedom for distributing the power flows in the vehicle. In the recuperation case, the EM acts as generator and charges the battery.

Predominantly, parallel HEVs may have a generally higher efficiency η than series HEVs since no energy conversion between ICE and powertrain is needed. Other characteristics in contrast to series HEVs are the integration of mechanical parts such as clutch and gear box into the powertrain and the omission of the generator.

2.2.3. Power-split Hybrid Electric Vehicles

In literature, the term *power-split* is also referred to as *combined* or *series-parallel*. This type of HEV is usually a parallel architecture with containing features of a series architecture and utilizes the advantages of both concepts. In general, a planetary gear set (PGS) is used for splitting the power flows between the propulsion systems. The drawbacks of this architecture lies in the higher control effort and possible circulating power flows.

2.2.4. Further Variants and Modifications

More advanced combinations of hybrid architectures which cannot be converted into the standard variants are described as complex hybrid architectures [38, 17]. In series HEVs, there are different variants for positioning one or more traction EMs. In the following, HEVs with only one driving axle are described but the principles can also be applied for a higher number of driving axles.

A common way is to use one central EM in combination with a differential to distribute the power to the traction wheels. Another option is using two EMs for one axle. This concept leads to advantages in terms of packaging, especially if the construction space is restricted. The use of wheel hub motors is a further option which has gained more attention since it provides a benchmark in terms of packaging and powertrain miniaturization. Drawbacks of this concept are the high costs as well as problems with increased, unsprung masses. In addition, the PGS needs to fulfill high requirements to cope with torque peaks introduced on uneven roads by the wheels to the significant inertia of the drive train. Due to the drawbacks mentioned above, only a few prototype vehicles have been equipped with this technology [73, 97].

2.3. Classifications

In this section general characteristics for the classification of HEVs are shown. The parameters introduced are independent of the hybrid architectures and allow to compare different configurations of HEVs. Firstly, the hybridization ratio h_r is defined by

$$h_r = \frac{P_{BAT}}{P_{TOTAL}} = \frac{P_{BAT}}{P_{BAT} + P_{ICE}}, \quad (2.6)$$

where P_{BAT} denotes the battery power at a defined, continuous C-rate (e.g. 3C), P_{ICE} the ICE power and P_{TOTAL} the total available power of battery and ICE. Other variants for describing the hybridization ratio h_r exist in literature (e.g. [78]) but the definition of Equation 2.6 is preferably used since it provides a normalized value between 0 and 1. The values of the hybridization ratio h_r for different vehicle categories can be classified into

- $h_r = 0$ for conventional vehicles,
- $0 < h_r < 1$ for hybrid vehicles,
- $h_r = 1$ for electric vehicles.

Secondly, the scaling of the energy storage represents another key parameter in the design process of HEVs. In Figure 2.4, the relation between these parameters is depicted for several HEVs and electric vehicles (EVs) available in 2013. It can be seen that higher values of the hybridization ratio h_r lead to increased storage capacities C_{STO} of the energy storage.

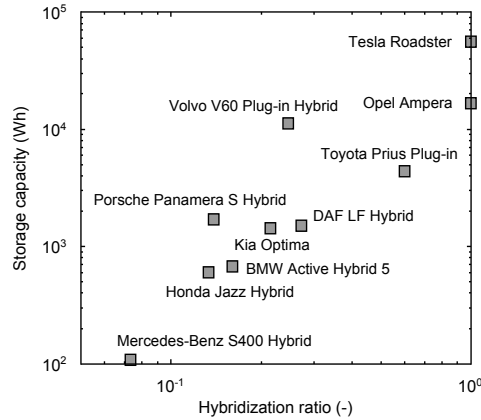


Figure 2.4.: Overview of storage capacity C_{STO} and hybridization ratio h_r for some HEVs and EVs available in 2013 [23].

Figure 2.4 shows that the values of the hybridization ratio h_r lie in a wide range between 0 and 1 in the field of HEVs. Due to this circumstance, a more accurate classification of HEVs by means of their functionality levels was introduced which has led to the following categories

- Micro hybrid,
- Mild hybrid,
- Full hybrid,
- Plug-in hybrid.

General characteristics of HEVs are implicitly given on the basis of these categories. In Table 2.1 the ranges of parameters such as the hybridization ratio h_r , electric motor power P_{EM} , battery energy content E_{BAT} and voltage level are listed for each category.

Table 2.1.: Comparison of different HEV classifications [40].

	Micro hybrid	Mild hybrid	Full hybrid	Plug-in hybrid
Hybridization ratio h_r (-)	< 0.05	0.05 - 0.1	0.1 - 0.5	0.3 - 0.8
Energy content E_{BAT} (kWh)	$\ll 1$	< 1	1 - 5	5 - 15
EM power P_{EM} (kW)	2 - 3	10 - 15	$\gg 25$	$\gg 25$
Voltage level (V)	12 - 48	48 - 150	> 200	> 200

In the following subsections the categories of HEVs are described in more detail.

2.3.1. Micro Hybrid

Micro hybrids are only a slight extension of CVs: This class of HEVs does not need an additional EM and uses the traditional alternator to perform the following operations:

- Recuperation of braking energy,
- Power supply to electrically driven auxiliaries.

In contrast to CVs, the idling losses and furthermore fuel consumption f_c of the ICE can be significantly reduced while the vehicle is stopped because the electronic control unit of the ICE turns off the fuel injection. This circumstance leads to many start-stop operations during typical driving scenarios (e.g. driving in the city). Thus, an intelligent battery management is necessary to ensure that the state of charge SOC of the battery is always sufficiently high to restart the ICE. Unlike other HEV concepts micro hybrids do not provide any traction force while the ICE is stopped. Beside the standard operations like starting, the alternator is generally designed to supply further electrical auxiliaries such as electrical fans or the electrically powered hydraulic steering. The recuperation of braking energy is possible with restrictions due to the low energy content of the battery E_{BAT} .

2.3.2. Mild Hybrid

The main difference between mild and micro hybrids consists in the fact that an additional EM contributes to the drivetrain. This component is used to assist the ICE while accelerating or to recuperate braking energy. Compared to micro hybrids the higher battery energy content E_{BAT} in combination with a higher EM power P_{EM} improves the recuperation of braking energy. However, pure electric propulsion is generally not possible due to low hybridization ratios h_r of 0.05 - 0.1.

2.3.3. Full Hybrid

In addition to the functions of mild hybrids such as electric boost and regenerative braking, full hybrid vehicles allow to start and drive with the EM only. Due to a higher energy content of the battery E_{BAT} compared to mild hybrids the recuperation of braking energy is enhanced. Full hybrids also provide the zero emission property (ZE) but as a result of the limited size of EM and battery, the pure electric driving range is limited. In contrast to plug-in hybrids, the battery can only be charged by means of the ICE combined with the EM. Generally, a charge-sustaining operating strategy is implemented since this type of hybrid cannot be charged externally. In contrast to a charge-depleting behavior, the charge-sustaining operating strategy keeps the battery's state of charge SOC at around a defined level. The difference between charge-depleting and charge sustaining operating strategies is outlined later in Section 3.1.3. In this thesis methodologies based on charge-sustaining operating strategies are developed which are suitable for both mild and full hybrids.

2.3.4. Plug-in Hybrid

Plug-in hybrids provide the same functionalities as full hybrids but have a higher energy content of the battery E_{BAT} . This characteristic allows pure electric driving for at least daily average urban distances (≈ 15 km - 100 km) [78]. As an additional feature to full hybrids the battery can be recharged from the grid. Thus, charge-depleting operating strategies in combination with recharging at a socket are meaningful options to reduce fuel consumption f_c . In order to achieve an overall reduction of CO_2 , the energy mix of the recharging current needs to be taken into account.

As an example, let us assume a vehicle's fuel consumption f_c of 5 lit./100 km. In addition, combustion of diesel fuel is considered which produces CO_2 emissions of 2.64 kg CO_2 /lit. The CO_2 emissions for producing electrical energy are 558 g/kWh according to the energy mix of the European Union in 2013 [32]. Furthermore, the transmission losses of electrical energy are neglected. Based on these specifications, the fuel consumption f_c and the electrical energy consumption e_{ec} can be compared as follows:

$$e_{ec} = \frac{5 \text{ lit./100 km} \cdot 2.64 \text{ kg}_{CO_2}/\text{lit.}}{0.558 \text{ kg}_{CO_2}/\text{kWh}} = 23.66 \text{ kWh/100 km.} \quad (2.7)$$

By means of Equation 2.7, a maximum electrical energy consumption $e_{ec,max}$ of the vehicle can be determined for a given fuel consumption f_c and energy mix. If the electrical energy consumption e_{ec} is higher than the calculated limit, then the use of electrified vehicles leads to higher CO_2 emissions compared to conventional vehicles.

A further category of HEVs based on pure EVs is called the range extended plug-in hybrid. This HEV type uses the EM as the only propulsion energy source but in contrast to EVs, a range extender (REX) or APU is integrated to recharge the battery if depleted to a specific minimum value. Range extended plug-in hybrids use a series hybrid topology which allows to decouple the REX from the drivetrain. One drawback of such series hybrid concepts is that the reliability of the whole electric drivetrain has to be at least as high as for standard ICE cars. The operating strategy of range extended plug-in hybrids is almost equivalent to strategies of EVs: if the level of the battery's state of charge SOC falls below a certain limit, the REX will be used to recharge the battery. By means of this strategy the overall range of the vehicle can be enhanced.

2.4. Summary

In this chapter an introduction to HEVs was given. After a short description of the power at the wheels P_W of vehicles, different classes of energy storages were shown. Furthermore, possible architectures of HEVs, their classification as well as the pros and cons were described. Overall, it can be seen that finding an optimal configuration for HEVs poses a complex task due to the high number of degrees of freedom which include for example the vehicle architecture, the scaling of components or the implemented operating strategy. This thesis focuses on the latter but also provides approaches in terms of optimal component sizing. In the following chapter different categories of operating strategies are outlined.

3. Operating Strategies for Hybrid Electric Vehicles

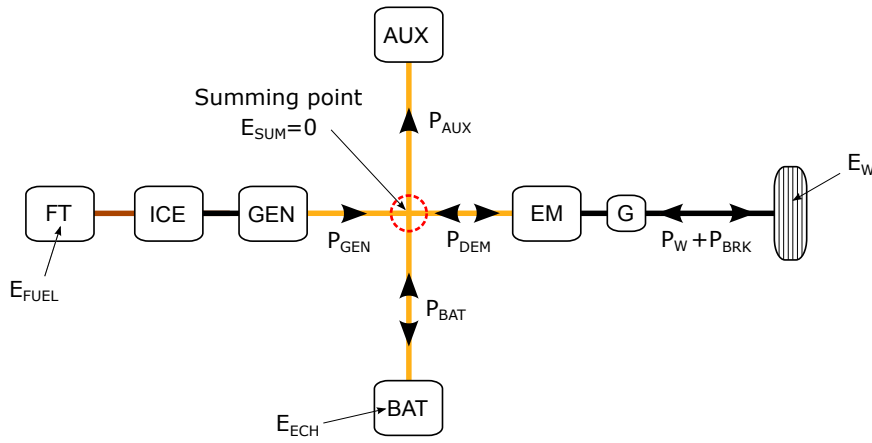
A control or operating strategy is used to execute several tasks in order to fulfill requirements of driver and vehicle components. Beside the consideration of component limits like maximum power or maximum temperature, its main goal is generally to achieve a lower energy consumption e_c of the vehicle. In contrast to conventional vehicles (CVs), operating strategies of hybrid electric vehicles (HEVs) are more complex due to a higher number of degrees of freedom and constraints. This chapter describes and classifies several control strategies for HEVs and outlines their pros and cons.

Since HEVs use two or more distinct energy sources, the main task of an operating strategy is to split the power flows from the energy sources under defined vehicle operating conditions (e.g. velocity v , acceleration \dot{v} , temperatures ϑ or power demand P_{DEM}) in order to reduce fuel consumption f_c .

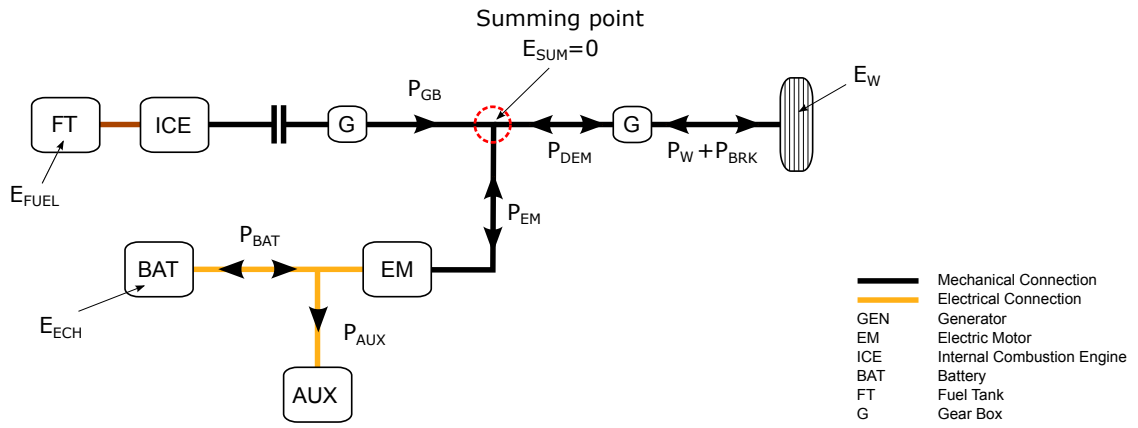
Firstly, the basics and challenges of operating strategies for HEVs are described by means of taking a closer look at the power flows in the vehicle. Figures 3.1(a) and 3.1(b) show the main components such as energy sources and energy converters for a series as well as a parallel HEV. In addition, component energies as well as power flows are depicted for selected parts of the HEV. In order to mathematically describe the energy distribution between energy sources and energy consumers it is necessary to define a summing point. As this summing point cannot store energy, not only the energy but also the sum of all power flows remains zero at this point. Thus, an equation can be set up to describe the power balance in the HEV.

Secondly, the power balance at the summing point needs to be specified in more detail. For this purpose, the power of all energy sources and energy consumers is related to the summing point by means of mathematical component models which may significantly differ in terms of complexity and accuracy. The model complexity can vary from oversimplified approaches containing constant efficiencies to highly sophisticated approaches considering for example thermal effects, component limits, time lags or moments of inertia. The choice of component models mainly depends on the application and affects the trade-off between accuracy and computational effort. Although the calculated power flows at the summing point are strongly influenced by means of the component models, the sum of all power flows always remains zero. The resulting power balance at the summing point represents a central part in terms of optimizing the operating strategies for HEVs.

In the following, the power balances at the summing points of Figures 3.1(a) and 3.1(b) are described in detail.



(a) Energies and power flows in a series HEV.



(b) Energies and power flows in a parallel HEV.

Figure 3.1.: Energies and power flows in series and parallel HEVs. Both figures depict energies and power flows of selected components where E_{FUEL} denotes the energy contained in the fuel tank, E_{ECH} the stored electrical energy of the battery, E_W the energy stored in the inertia of the wheels, P_{GEN} the power of the generator, P_{AUX} the power of the electrical auxiliaries, P_{BAT} the available power at the battery terminal, P_{DEM} the power demand due to the driving cycle, P_W the power at the wheels, P_{BRK} the power of the mechanical brakes, P_{GB} the power at the gear box output and P_{EM} the mechanical power of the EM. The relations between these energies and power flows are defined by means of component models. In addition, a summing point is depicted for each topology. As the summing points cannot store energy, an equation can be set up in order to describe the power balance. This equation represents a central element in terms of optimizing the operating strategies of HEVs.

In case of a series hybrid topology shown in Figure 3.1(a), the power balance at the summing point E_{SUM} can be derived as follows:

The energy at the summing point E_{SUM} is always zero and consequently, the sum of power flows remains also zero.

$$E_{SUM} = 0 \quad (3.1)$$

$$\frac{d}{dt}(E_{SUM}) = 0 \quad (3.2)$$

$$P_{GEN} + P_{BAT} - P_{AUX} - P_{DEM} = 0, \quad (3.3)$$

where P_{GEN} denotes the power of the generator, P_{BAT} the available power at the battery terminal, P_{AUX} the power of the auxiliaries and P_{DEM} the power demand due to the driving cycle. In order to determine the power demand P_{DEM} , the power at the wheels P_W and the power of the mechanical brakes P_{BRK} are taken into account.

The energy balance at the summing point of a parallel hybrid topology shown in Figure 3.1(b) can be derived as follows:

Again, the sum of power flows at the summing point is zero.

$$E_{SUM} = 0 \quad (3.4)$$

$$\frac{d}{dt}(E_{SUM}) = 0 \quad (3.5)$$

$$P_{GB} + P_{EM} - P_{DEM} = 0, \quad (3.6)$$

where P_{GB} denotes the output power of the gear box, P_{EM} the power of the electric motor and P_{DEM} the power demand due to the driving cycle. The power demand P_{DEM} considers the power at the wheels P_W as well as the power of the mechanical brakes P_{BRK} . In contrast to the series topology, the power of auxiliaries P_{AUX} is not taken into account at the summing point but implicitly considered by means of the electric motor power P_{EM} .

Until now, the energy balance in a HEV was demonstrated by means of a series and parallel hybrid topology. The principle can also be used for more complex topologies but in that case the summing point needs to be adjusted accordingly.

Based on the power flow analysis described above, operating strategies can be derived for HEVs. In general, there are two main categories of operating strategies which are either classified into rule-based or optimization-based concepts. Both concepts are divided into further sub-categories that differ for example in terms of optimality, complexity or in the use of predicted data. In the following, these categories of operating strategies are described in more detail.

3.1. Rule-based Strategies

Rule-based strategies use heuristics to define the power-split u_s in a HEV. Hence, this type of concept is also referred to as heuristic strategies [38]. The main idea of this type of operating strategy is to apply "if-then" rules that assign a combination of state variables x and control variables u to corresponding power-splits u_s . The derivation of rules can be done by means of intuition, human expertise as well as mathematical models. Typical rules are for example:

- If the state of charge (SOC) is below a defined limit, then the ICE is additionally used for recharging,
- If the SOC is above a defined limit, then the EM is preferably used,
- If the velocity v of the vehicle is low, then only the EM is used,
- If high power demands P_{DEM} occur, then the EM assists the ICE.

In the next step, these "if-then" conditions are transformed into mathematical relations. For this purpose, concepts usually based on boolean or fuzzy logic are applied to describe the operating strategy. Since no knowledge about future driving conditions is used, the resulting rules are causal and especially suitable in real-time applications. The main drawback of this concept is that these operating strategies are sub-optimal in nearly all applications. The reason for this sub-optimality is that no future data about the driving profile can be taken into account. For example, the information about future downhill gradients cannot be used in order to prefer electric propulsion. To summarize, rule-based strategies cannot be applied to assess the minimum fuel consumption f_c for given vehicle configurations and driving cycles. However, the extension and optimization of rules is possible and can be considered to improve the fuel economy of defined scenarios. The following subsections provide a brief overview of rule-based control strategies. Further details can be found in [38, 87].

3.1.1. Deterministic Concepts

In the deterministic or boolean approach the rule-based operating strategy is usually implemented by means of look-up tables. Thus, the power-split u_s used to describe the split between the power of the battery P_{BAT} and the engine P_{ICE} is defined for a given combination of state variables x and control variables u . For example, the power-split u_s can depend on the state of charge SOC, the total power demand P'_{DEM} given by the sum of power demand due to the driving cycle P_{DEM} and electrical auxiliaries P_{AUX} , the total torque demand M'_{DEM} given by the sum of torque demand due to the driving cycle M_{DEM} and generator M_{GEN} , or the velocity v .

The power-split u_s is defined as follows

$$u_s = \frac{P_{BAT}}{P_{DEM} + P_{AUX}} = \frac{P_{BAT}}{P'_{DEM}}, \quad (3.7)$$

where P_{BAT} denotes the battery power, P_{DEM} the power demand due to the driving cycle, P_{AUX} the power demand of electrical auxiliaries and P'_{DEM} the total power demand. In other words, the power-split u_s provides the ratio of pure electric power to the total power demand P'_{DEM} . Furthermore, a positive battery power P_{BAT} discharges the battery and a negative battery power P_{BAT} charges the battery.

In case of propulsion ($P_{DEM} > 0$ or $M_{DEM} > 0$) a power-split u_s of 1 represents pure electric driving. In this scenario the battery delivers the power for propulsion and for the auxiliaries. In addition, pure propulsion by means of the engine is described with a power-split u_s of 0. In that case, the power of the electrical auxiliaries P_{AUX} is only provided by the generator. The use of both energy sources, battery and engine, is considered by means of power-splits of $0 < u_s < 1$. In case of braking ($P_{DEM} < 0$ or $M_{DEM} < 0$), recuperation of braking energy is described by means of a power-split u_s of 1. Obviously, charging of the battery is only

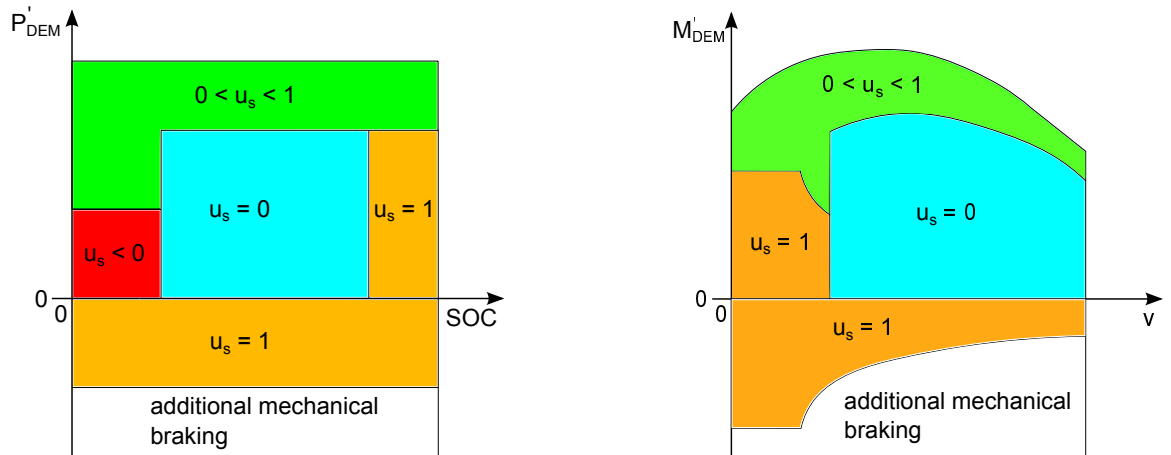
possible if the power demand of electrical auxiliaries P_{AUX} is lower than the recuperation power.

Until now, the driving scenarios only require power-splits u_s that lie between 0 and 1. However, the value ranges of the power-split u_s need to be extended in order to take into account further scenarios. Whereas a power-split of $u_s < 0$ considers recharging during propulsion, a power split of $u_s > 1$ supports recharging in case of braking.

To summarize the power-split u_s can be classified into the following value ranges

- $u_s = 0$ ICE propulsion (generator provides electric power of the auxiliaries P_{AUX}),
- $u_s = 1$ Electric propulsion / electric braking,
- $0 < u_s < 1$ ICE and electric propulsion,
- $u_s < 0$ Recharging in case of propulsion,
- $u_s > 1$ Additional recharging in case of electric braking.

In the next step, control maps can be designed on the basis of driving scenarios and corresponding power-splits u_s . Figures 3.2(a) and 3.2(b) show typical control maps for heuristic operating strategies. The illustrations also depict the variety of combinations to define the size and shape of power-split regions. These regions are mainly restricted by means of component limits such as maximum engine power P_{ICE} or maximum charge or discharge power of the battery P_{BAT} and can be seen as a reference for the power-split u_s . In practical applications, the power-split u_s determined by the control maps needs to be adjusted if further component limits like temperatures are exceeded.



(a) Control map depending on the battery's state of charge SOC and total power demand P'_{DEM} given by the sum of power demand due to the driving cycle P_{DEM} and electrical auxiliaries P_{AUX} .

(b) Control map depending on velocity v and total torque demand M'_{DEM} given by the sum of torque demand due to the driving cycle M_{DEM} and generator M_{GEN} .

Figure 3.2.: Examples for rule-based operating strategies (based on [98, 38]). The power-split u_s is categorized in: recharging in case of propulsion ($u_s < 0$), ICE propulsion ($u_s = 0$), electric propulsion / braking ($u_s = 1$), ICE combined with electric propulsion ($0 < u_s < 1$). A more detailed explanation can be found in the text above.

Regions with preferable recharging ($u_s < 0$) can contain very low values of the power split u_s especially if the total power demand P'_{DEM} is small. Hence, a lower constraint of the power-split u_s in this region needs to be considered in practical implementations. As depicted in Figures 3.2(a) and 3.2(b) the different regions of the power-split u_s are divided by means of boundaries. In that case, limit cycles and "chattering" can occur if operating points of state variables x and control variables u exactly lie on these boundaries. To avoid these problematic effects as well as to obtain a stable behavior of the controller, the implementation of hystereses and the smoothing of the power-split map are recommended.

3.1.2. Fuzzy Concepts

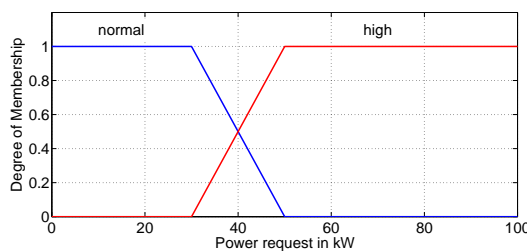
Another approach for rule-based operating strategies relies on fuzzy logic. The main advantages of these methods are the following [87]:

- Robustness, since they are tolerant to imprecise specifications, measurements and component variations,
- Ideal "Man-Machine Interface", since the fuzzy rules can be easily defined and tuned if necessary.

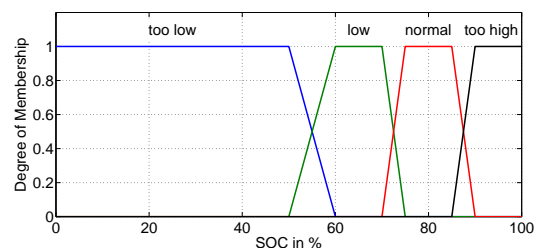
Fuzzy logic represents a practical control concept especially if the system model is unknown or only partly described. However, there are also drawbacks which are for example:

- Manual tuning of rules in case of large-scale applications which may be time-consuming,
- Plurality of rules for a higher number of input variables which may not fulfill real-time requirements,
- Stability proofs are only available for certain classes of fuzzy logic systems [33, 100, 105].

Compared to the deterministic case, the fuzzy logic allows to use descriptions such as *slightly*, *fairly*, *low*, *normal*, *high*, *cold* or *warm* in the implementation of control rules. The mapping of fuzzy rules into mathematical relations is carried out by means of membership functions. For given sets of control variables u , corresponding degrees of memberships are calculated. Figures 3.3(a) and 3.3(b) depict examples how to define membership functions in the context of HEVs.



(a) Membership functions that assign the power request to the degree of membership for the descriptions *normal* and *high*.



(b) Membership functions that assign the state of charge SOC to the degrees of membership for the descriptions *too low*, *low*, *normal* and *too high*.

Figure 3.3.: Examples for typical membership functions in fuzzy control of HEVs [86].

Finally, the degrees of membership are "defuzzified" by means of weighting functions together with fuzzy logic to obtain corresponding power-splits u_s and control variables u . Representative examples for the implementation of fuzzy logic in operating strategies of HEVs and further references can be found in [87, 16, 89, 39].

3.1.3. Concepts for Plug-in Hybrid Electric Vehicles

Until now, the mentioned rule-based operating strategies provide a charge-sustaining behavior which is necessary to fulfill the power demands P_{DEM} of different scenarios over a longer period of time. However, a pure charge-sustaining strategy is not desirable for plug-in HEVs in terms of fuel economy. As stated in Section 2.3.4, plug-in HEVs can be charged from the grid and have a higher battery energy content E_{BAT} compared to other HEV categories. Thus, a more efficient operating strategy that exploits the external recharging of the battery should be applied. This strategy can be described as follows: At the beginning of each driving scenario, electric propulsion is preferably used until a minimum limit of the state of charge SOC is reached. This part of the strategy can be denoted as charge-depleting mode which is also the operating strategy of EVs. If the state of charge SOC falls below a defined threshold the charge-sustaining mode is activated to maintain the functionality of HEVs. The combination of both modes described above leads to the charge-depleting / charge-sustaining operating strategy (CDCS) [120] depicted in Figure 3.4.

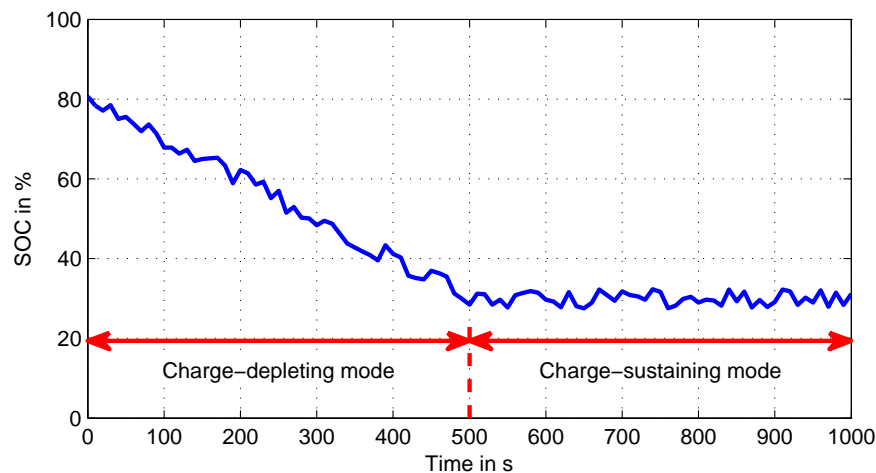


Figure 3.4.: Charge-depleting / charge-sustaining operating strategy for plug-in HEVs. In the charge-depleting mode the vehicle is mainly propelled electrically until a lower threshold of the state of charge SOC is reached. Then, the charge-sustaining mode is activated to keep the state of charge SOC around a defined level.

For shorter driving cycles, the CDCS operating strategy maximizes the part of pure electric driving since the ICE is only activated for power demands P_{DEM} that exceed the maximum EM power P_{EM} . This circumstance significantly improves the fuel economy if the charge-depleting mode is activated. In addition, the overall emissions can be reduced if the current for recharging the battery comes from renewable energy sources.

3.2. Optimization-based Strategies

A further class of operating strategies in HEVs is based on different optimization concepts. In contrast to rule-based strategies, the power demand P_{DEM} of a driving scenario is assumed to be known in advance. Thus, it is possible to calculate for a given vehicle configuration the globally optimal control strategy, which is especially useful to perform the following tasks:

- Calculating a benchmark for an operating strategy,
- Comparing different vehicle concepts and component sizes.

Representative methods to determine the global optimum are dynamic programming (DP) [8], the maximum principle of Pontryagin (PMP) [36] or linear programming (LP) [106]. The resulting operating strategies have a-causal behavior since the calculation considers future data. Consequently, these strategies are not directly applicable in real-time applications but, by means of appropriate modifications, parts of the results can be re-used. Concepts based on modified optimal strategies are for example model predictive control (MPC) [15] or equivalent consumption minimization strategies (ECMS) [75]. Unfortunately, these methods generally lead to sub-optimal solutions over a whole driving scenario due to the lack of sufficient future data.

3.2.1. Fundamentals

The goal of an optimization method is to find the optimal control variable u^* that minimizes a defined performance index J of the general form

$$J(x_0, u) = \int_{t_0}^{t_f} L(t, x, u) dt, \quad (3.8)$$

where J denotes the performance index, x_0 the initial state, u the control variables, t_0 the initial time, t_f the final time and $L(\cdot)$ the cost function that may depend on time t , state variables x and control variables u . If the performance index J is to be maximized, then only the sign of the cost function $L(\cdot)$ has to be inverted.

Furthermore, the optimization may consider system dynamics $f(\cdot)$, final values of the state variable x_f as well as constraints of both state and control variables:

$$\dot{x} = f(t, x, u) \quad (3.9)$$

$$x(t_f) = x_f, \quad (3.10)$$

$$u_{min} \leq u \leq u_{max}, \quad (3.11)$$

$$x_{min} \leq x \leq x_{max}, \quad (3.12)$$

$$x \in \mathcal{X}, \quad (3.13)$$

$$u \in \mathcal{U}. \quad (3.14)$$

The solution of Equation 3.8 leading to the optimal performance index $J^*(x_0, u)$ is described by means of the optimal control variable u^* .

In a further step, the function

$$\mathcal{J}(t, x_t) = \min_{u([t, t_f])} \int_t^{t_f} L(\tau, x, u) d\tau, \quad (3.15)$$

is introduced. The function describes the optimal cost-to-go depending on time as well as on corresponding state variables x_t . Further references and more detailed information in terms of optimization theory and optimal control can be found in [23, 38, 87].

In order to obtain the optimal control variable u^* the following "principle of optimality" taken from [6] must hold:

"An optimal policy has the property that whatever the initial state and initial decision are, the remaining decisions must constitute an optimal policy with regard to the state resulting from the first decision."

The "principle of optimality" states that if the performance index $J(x_0, u^*([t_0, t_f]))$ is optimal, then the performance index $J(x^*(t_1), u^*([t_1, t_f]))$ of a truncated control variable $u^*([t_1, t_f])$ is optimal, too. The justification of this fact is proved by contradiction. Supposing that the optimal control variable over time $u^*(t)$ is not optimal in a truncated interval $[t_1, t_f]$, another solution would exist and improve the performance index $J(x^*(t_1), u^*([t_1, t_f]))$ of the sub-problem. Obviously, the assumption that the control variable over time $u^*(t)$ describes the optimal solution, is not valid any longer. A graphical description of the principle of optimality is shown in Figure 3.5.

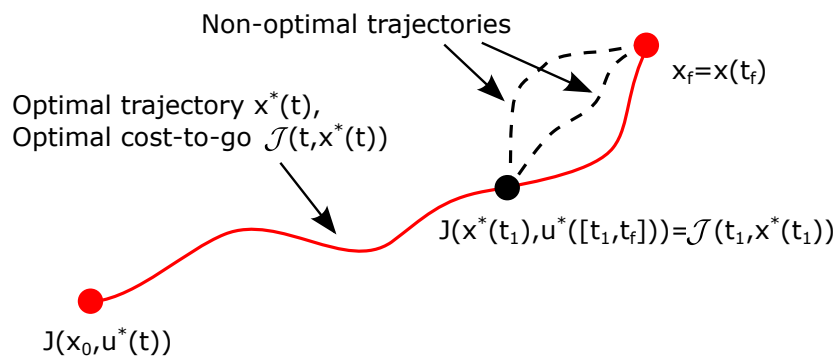


Figure 3.5.: Illustration of the trajectory of the optimal state variable $x^*(t)$ from initial state x_0 to final state x_f and corresponding optimal cost-to-go $\mathcal{J}(t, x^*(t))$. As described in the principle of optimality [6], the trajectory of the state variable $x^*(t)$ in the sub-interval $t = [t_1, t_f]$ has to be optimal, too.

By means of the "principle of optimality" the Hamilton-Jacobi-Bellman equation (HJBE) can be derived which is briefly shown in Appendix B.1. Additional information is also provided in [8].

The HJBE is defined by means of a partial differential equation

$$\frac{\partial}{\partial t} \mathcal{J}(t, x) + \min_{u \in \mathcal{U}} \left(L(t, x, u) + \frac{\partial}{\partial x} \mathcal{J}(t, x) \cdot f(t, x, u) \right) = 0, \quad (3.16)$$

where $\mathcal{J}(\cdot)$ denotes the optimal cost-to-go, $L(\cdot)$ the cost function and $f(\cdot)$ the system dynamics. The optimal control variable u^* is given by means of the solution of Equation 3.16 but generally an analytical expression cannot be found in practical cases. However, the HJBE represents a powerful tool to find optimal solutions with the help of numerical methods.

Another analytic approach for calculating optimal solutions is given by minimizing the Hamiltonian function

$$H(t, x, u, \lambda) = L(t, x, u) + \lambda \cdot f(t, x, u) \quad (3.17)$$

where $L(\cdot)$ denotes the cost function and $f(\cdot)$ the system dynamics. In addition, the symbol λ represents weighting factors that are denoted as Lagrange multipliers [49]. In contrast to solving the HJBE, this approach allows to significantly reduce the computational time.

In the following, both approaches for calculating the optimal control variable u^* are described in more detail.

3.2.2. Methods for Optimal Control

In the previous section the optimal control problem was introduced from a mathematical point of view which has led to the Hamiltonian function $H(\cdot)$ as well as to the HJBE. Based on these derivations, two optimization methods are commonly used to solve the optimal control problem:

- 1.) Dynamic Programming,
- 2.) Pontryagin's maximum principle.

The former represents a numerical method to calculate the solution of the HJBE, whereas the latter depicts an analytical approach based on minimizing the Hamiltonian function $H(\cdot)$.

As an alternative, approximations of the cost function $L(\cdot)$ of Equation 3.8 allow to use further optimization techniques such as linear programming (LP) or quadratic programming (QP). Although the computational effort can be substantially reduced, the necessary discretization as well as simplifications of the optimization problem generally lead to approximations of the optimal solutions.

Dynamic Programming

Dynamic programming (DP) [6] is a numerical method for solving multistage decision-making problems and has been applied in many areas of science [62, 8, 9]. This method calculates optimal solutions for problems of various complexity. Depending on the formulation of the optimization problem, the algorithm also allows to determine globally optimal solutions. Further, DP is a suitable method for solving the HJBE that has been introduced in Section 3.2.1 and for calculating an optimal operating strategy for HEVs.

The calculation of a DP has polynomial complexity and is efficient for a low number of state variables x and control variables u :

If we assume an optimization problem containing N stages and N_u discretized values of the control variable u , then a "brute-force" search will lead to

$$N_{BF} = N_u^{N-1} \quad (3.18)$$

possible solutions. Instead of evaluating all variants, which needs exponential computational time, and afterwards taking the optimum, DP can handle such problems with polynomial

complexity. If we assume that the state variable is discretized into N_x values then the calculation effort can be estimated by means of

$$N_{DP} = (N - 1) \cdot N_x \cdot N_u. \quad (3.19)$$

Unfortunately, for multidimensional state spaces \mathcal{X} the calculation becomes slow due to the "curse of dimensionality" [8] but this effect can be reduced through the use of approximation techniques.

As stated before, DP represents a powerful tool for solving the HJBE and obtaining the global optimum. For the sake of completeness, the relation between the HJBE and DP is provided in Appendix B.3.

The goal of the DP algorithm is to calculate the optimal control policy

$$\pi = \{u_0^*, u_1^*, \dots, u_{N-1}^*\}, \quad u_k^* \in \mathcal{U}_k \quad (3.20)$$

that minimizes the performance index $J(x_0, \pi)$.

Since DP is a numerical method, the continuous cost function $L(\cdot)$ of Equation 3.8 needs to be discretized leading to the performance index

$$J(x_0, \pi) = L_N(x_f) + \sum_{k=0}^{N-1} L_k(x_k, u_k), \quad k = 0, 1, \dots, N - 1, \quad (3.21)$$

where $L_N(x_f)$ denotes the costs for deviations from a desired final state x_f and $L_k(\cdot)$ the discrete cost function. Furthermore, the continuous system dynamics $f(\cdot)$ are discretized by means of

$$x_{k+1} = f_k(x_k, u_k), \quad k = 0, 1, \dots, N - 1. \quad (3.22)$$

In order to describe the discrete system dynamics $f_k(\cdot)$, several approaches like the methods of Euler or Runge-Kutta can be taken into account [49].

In Section 3.2.1 the principle of optimality has been described. It states that sub-trajectories of an optimal path have to be also optimal. Hence, the original optimization problem of Equation 3.21 is parted into a sub-problem

$$J(x_i, \pi([i, N - 1])) = L_N(x_f) + \sum_{k=i}^{N-1} L_k(x_k, u_k), \quad (3.23)$$

which is minimized by the truncated optimal control policy $\pi([i, N - 1]) = \{u_i^*, u_{i+1}^*, \dots, u_{N-1}^*\}$.

In the next step the discrete function $\mathcal{J}(i, x_i)$ is introduced to express the truncated performance index $J(x_i, \pi([i, N - 1]))$. This function describes the corresponding sum of minimum costs between stages i and N .

By means of Equation 3.23 the central calculation step of DP can be derived in order to find the optimal control variable

$$u_k^* = \arg \min_{u_k \in \mathcal{U}_k} \left(L_k(x_k, u_k) + \mathcal{J}(k + 1, f_k(x_k, u_k)) \right), \quad (3.24)$$

$$k = N - 1, N - 2, \dots, 1, 0.$$

Finally, the optimal control policy π can be obtained by proceeding from state x_0 to x_f . Based on the principle of optimality, the optimal control variable u_k^* that minimizes the cost-to-go $\mathcal{J}(k, x_k^*)$ is chosen at each stage index k .

In order to use DP for calculating the optimal operating strategies of HEVs, the cost function $L(\cdot)$ as well as the state variables x and control variables u have to be defined accordingly. The number of stages N is often given by means of the time discretization of the driving cycle but the use of a discretized distance provides another option. Usually, the state of charge SOC of the battery defines the state variable x and the battery power P_{BAT} is used as control variable u . In addition, disturbances w over time are included in order to consider the power demand P_{DEM} of the driving cycle.

Since DP is a central topic of this thesis, Chapter 4 provides a more detailed description and compares different variants and adaptations in terms of its implementation.

Maximum Principle of Pontryagin

The maximum (or sometimes denoted as minimum) principle of Pontryagin states that an optimal control variable u^* minimizes the Hamiltonian function $H(\cdot)$ defined in Equation 3.17. Thus, the following inequality must hold:

$$H(t, x^*(t), u^*(t), \lambda^*(t)) \leq H(t, x^*(t), u, \lambda^*(t)). \quad (3.25)$$

The minimization of the Hamiltonian function $H(\cdot)$ provides a simplification of the HJBE and allows to drastically reduce the calculation effort. However, the minimization only uses necessary conditions and consequently, it is possible that the calculated optimal control variable u^* just leads to locally optimal solutions.

In addition to Equation 3.25, the minimization of the Hamiltonian function $H(\cdot)$ can be described as follows

$$u^*(t) = \arg \min_{u \in \mathcal{U}} H(t, x^*(t), u, \lambda^*(t)). \quad (3.26)$$

Based on Equation 3.26, the Pontryagin's maximum principle (PMP) can be derived, which leads to the following set of differential Equations 3.27 - 3.28.

$$\dot{x}^*(t) = \frac{\partial H}{\partial \lambda}(t, x^*(t), u^*(t), \lambda^*(t)), \quad (3.27)$$

$$\dot{\lambda}^*(t) = -\frac{\partial H}{\partial x}(t, x^*(t), u^*(t), \lambda^*(t)). \quad (3.28)$$

$$H(t, x^*(t), u^*(t), \lambda^*(t)) \leq H(t, x^*(t), u, \lambda^*(t)). \quad (3.29)$$

A brief derivation of the conditions of Equations 3.27 - 3.28 is provided in Appendix B.2. Additional information and formal proofs about the PMP can be found in [36, 49, 8].

The set of coupled differential Equations 3.27 and 3.28 describes a two-point boundary value problem with boundary conditions on the basis of the initial state variable $x(t_0)$ and final co-state $\lambda(t_f)$, respectively. Instead of using a fixed state at the final time t_f , it is possible to include an additional term $\varphi(\cdot)$ which penalizes deviations from a defined final state x_f . By means of the additional term $\varphi(\cdot)$, $\lambda(t_f)$ is implicitly determined, which leads to the following relation

$$\lambda(t_f) = \left(\frac{\partial}{\partial x} \varphi(x(t)) \right)_{t=t_f}. \quad (3.30)$$

Usually, the Hamiltonian function $H(\cdot)$ contains the mass flow rate of fuel \dot{m}_f as cost function and the time derivative of the state of charge \dot{SOC} as system dynamics $f(\cdot)$. The weighting between these terms is given with the help of the generally time-dependent co-state $\lambda(t)$ and the control variable u is defined by means of the battery power P_{BAT} .

In previous work, the behavior of the co-state λ has been investigated in detail [23, 47, 55]. It has been shown that the co-state λ is continuous and monotonically decreasing over time for unconstrained optimization problems [23]. If possible limits of state variables (x_{min} , x_{max}) are reached, the co-state λ becomes discontinuous. In case of reaching the maximum limit of the state of charge SOC, the co-state λ will discontinuously decrease to preferably use battery power P_{BAT} . In [55], for example, a method to handle such constraints is described. It appropriately divides the optimization problem into sub-problems and uses an iterative approach. The approach stops if all sub-trajectories stay within the state limits. In contrast, the work of [48] presents a method which adds a quadratic penalty term to the Hamiltonian function $H(\cdot)$ to avoid the exceeding of limits of the state variable x .

If the system dynamics $f(\cdot)$ does not depend on the state of charge SOC, then a constant co-state λ is obtained since

$$\dot{\lambda}(t) = -\frac{\partial}{\partial SOC} \left(L(P_{BAT}(t), P_{DEM}(t)) + \lambda(t) \cdot f(P_{BAT}(t)) \right) = 0. \quad (3.31)$$

As shown in [38], this assumption can be used if a charge-sustaining behavior of the battery in combination with small charge and discharge swings is assumed. Then, the Hamiltonian function $H(\cdot)$ acquires a new meaning and can be depicted as a sum of power terms

$$P_F(u, P_{DEM}(t)) + s \cdot P_{ECH}(u) = \dot{m}_f(u, P_{DEM}(t)) \cdot H_{LV} + s \cdot P_{ECH}(u), \quad (3.32)$$

where s denotes the equivalence factor that can be seen as the weight between the use of fuel power P_F and electrochemical power P_{ECH} . Whereas the fuel power P_F is given by means of the mass flow rate of fuel \dot{m}_f multiplied by the lower heating value H_{LV} , the electrochemical power P_{ECH} of the battery is determined by means of the sum of terminal battery power P_{BAT} and power loss $P_{LOSS,BAT}$. In addition, the battery power P_{BAT} or the power-split u_s can be used as control variable u . Obviously, a higher value of the equivalence factor s leads to a preferred use of the ICE and vice-versa. This approach provides the basis for the causal equivalent consumption minimization strategy (EMCS) which will be described in the next Section 3.3.

Further Algorithms

In addition to DP and PMP, further optimization techniques such as linear programming (LP) and quadratic programming (QP) can be used to obtain the optimal operating strategies for HEVs. One thing both variants have in common is that a discrete version

$$J(x_0, \pi) = \sum_{k=k_0}^{k_f} L_k(x_k, u_k) \quad (3.33)$$

of Equation 3.8 is used. This approximation allows to reduce excessive memory usage and furthermore leads to low calculation times while handling a multidimensional state space \mathcal{X} . Depending on the algorithm, special requirements in terms of the cost function $L(\cdot)$ as well

as the model formulations and system dynamics $f(\cdot)$ must be taken into account. In general, these simplifications lead to sub-optimal results compared with DP or PMP.

LP has been successfully used for optimizing the control strategy of HEVs in [104]. The authors applied a number of transformations to obtain a linear program in standard form. As an example, the relation between fuel consumption f_c and engine power P_{ICE} as well as the mathematical description between electrical and mechanical power of the EM are assumed to be linear. Further work based on LP can be found in [99, 7].

In contrast to LP, the method of QP includes quadratic relations in the cost function $L(\cdot)$ in combination with linear constraints and calculates solutions that are close to the global optimum [23]. For example, the framework of QP allows to consider a quadratic approximation between fuel consumption f_c and engine power P_{ICE} . Representative work has been performed by [5, 50, 119].

3.3. From Optimal to Real-time Strategies

After an introduction to heuristic and optimal control laws in Sections 3.1 and 3.2, respectively, a further category of operating strategies is introduced that uses adapted optimal concepts in real-time applications. Obviously, these approaches lead to sub-optimal solutions due to the assumption that the whole driving cycle is not known in advance. Typical methods of such online controllers are the equivalence consumption minimization strategy or model predictive control. Although some of these methods use predicted data, this category is assigned to causal control methods [38].

3.3.1. Equivalent Consumption Minimization Strategy

The equivalent consumption minimization strategy (ECMS) was firstly introduced by [75] with the help of a heuristic concept. This strategy is suitable for HEVs in the charge-sustaining mode and uses the fact that consumption of electrical energy can be converted into an equivalent amount of fuel.

In Section 3.2 the PMP, which can also serve for deriving the ECMS from an optimal point of view, has been introduced. In that case, the co-state λ represents the equivalence factor s . In contrast to the PMP, the ECMS reduces the global optimization problem to an instantaneous minimization problem without any use of information regarding the future.

The battery can be seen as an auxiliary, reversible fuel tank that is never refilled externally. In order to keep the state of charge SOC charge-sustaining, the electricity used during the battery discharge phase must be replenished later by means of the fuel from the tank in combination with the ICE and the generator. If the state of charge SOC is higher than a defined reference, the use of electrical energy will save an equivalent amount of fuel in the future. In both scenarios a virtual fuel consumption can be determined by means of the use of electrical energy and fuel consumption f_c . As described in [83], an instantaneous virtual fuel consumption is obtained which can be converted into an equivalent power P_{EQV} leading to

$$P_{EQV}(t, u, s) = P_F(u, P_{DEM}(t)) + s \cdot P_{ECH}(u), \quad (3.34)$$

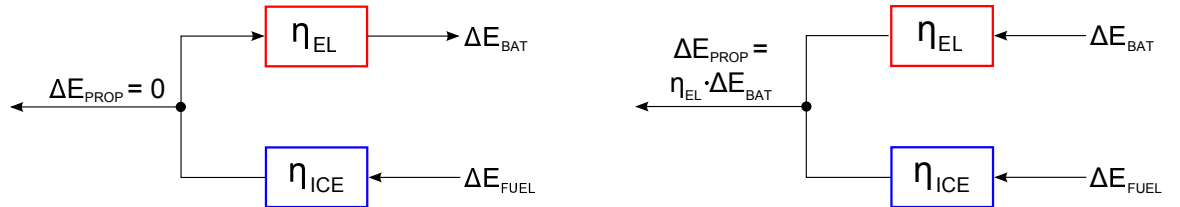
which is equal to the definition of Equation 3.32. The equivalence factor s that can be seen as the weight between the use of fuel power P_F and electrochemical power P_{ECH} . Whereas the fuel power P_F is given by means of the mass flow rate of fuel \dot{m}_f multiplied by the lower

heating value H_{LV} , the electrochemical power P_{ECH} of the battery is determined by means of the sum of terminal battery power P_{BAT} and power loss $P_{LOSS,BAT}$. In terms of the power loss $P_{LOSS,BAT}$, specifications of the battery as for example thermal limits need to be considered. The goal of the ECMS is to minimize the equivalent power P_{EQV} in Equation 3.34 at each time instant. In order to obtain an improved fuel economy, an appropriate estimation of the equivalence factor s is necessary.

Estimation of equivalence factors

The equivalence factor s plays an important role since it influences the fuel consumption f_c and the use of battery power P_{BAT} . In the following, several methods for the estimation of the equivalence factor s are presented that are either based on heuristic or optimal approaches. These methods include model-based, PMP-based as well as DP-based approaches.

The value of the equivalence factor s depend on the driving cycle and affects the fuel consumption f_c of the vehicle. Furthermore, the battery tends to be discharged if the equivalence factor s is too low (charge-depleting behavior), or to be charged if it is too high (charge-increasing behavior) [83]. In the simplest implementation the value of the equivalence factor s is only represented by means of a constant. In other variants a set of at least two equivalence factors $\{s_1, \dots, s_n\}$ is used that consider the chain of efficiencies through which the fuel power P_F is transformed into electrochemical power P_{ECH} and vice-versa. If constant efficiencies η are assumed, then two equivalence factors s_{ch} and s_{dis} are needed to describe the battery charge and discharge modes. The following Figures 3.6(a) and 3.6(b) depict both modes.



(a) Discharge mode: To compensate a discharge battery energy ($\Delta E_{BAT} < 0$), an equivalent amount of fuel energy $\Delta E_{BAT}/(\eta_{EL} \cdot \eta_{ICE})$ is needed.

(b) Charge mode: The use of a charge battery energy ($\Delta E_{BAT} > 0$) saves an equivalent amount of fuel energy $\Delta E_{BAT} \cdot \eta_{EL}/\eta_{ICE}$.

Figure 3.6.: Cases for describing the fuel equivalence of energy storages by means of constant efficiencies η (based on [38]).

The resulting equivalence factors for discharging s_{dis} and charging s_{ch} can be approximated by

$$s_{dis} = \frac{1}{\eta_{EL} \cdot \eta_{ICE}}, \quad (3.35)$$

$$s_{ch} = \frac{\eta_{EL}}{\eta_{ICE}}. \quad (3.36)$$

Another method to estimate the equivalence factors s_{ch} and s_{dis} has been shown in [90]. In contrast to the previous approach, no knowledge about the component efficiencies is needed.

Instead, several simulations with different (constant) power-splits u_s are carried out for a defined driving cycle. By means of the results, the energy content of the battery E_{BAT} and the energy content of the fuel tank E_{FUEL} are compared, which leads approximately to two piecewise linear functions. The gradients of these functions represent the equivalence factors s_{ch} and s_{disch} , respectively.

As stated before, the ECMS can also be derived from an optimal point of view by means of the PMP. In Section 3.2 it has been shown that an optimal control variable u^* minimizes the Hamiltonian function $H(\cdot)$:

$$u^*(t) = \arg \min_{u \in \mathcal{U}} H(t, x^*(t), u, \lambda^*(t)). \quad (3.37)$$

This knowledge is used again to derive the ECMS. Instead of solving a set of differential Equations 3.27 - 3.28 to obtain the global optimum, the ECMS only calculates the optimal control variable u^* at each time instant and can be applied in real-time applications. Since future driving conditions are assumed to be unknown the ECMS generally calculates sub-optimal but causal solutions compared to the PMP.

The following Equations 3.38 and 3.39 provide a comparison of the Hamiltonian function

$$H(t, x, u, \lambda) = L(t, x, u) + \lambda \cdot f(t, x, u) \quad (3.38)$$

and the equivalent power

$$P_{EQV}(t, u, s) = P_F(u, P_{DEM}(t)) + s \cdot P_{ECH}(u). \quad (3.39)$$

It can be seen that the equivalent power P_{EQV} of Equation 3.39 depicts a specific formulation of the general Hamiltonian function $H(\cdot)$ of Equation 3.38. Due to this fact the results of PMP can be re-used to estimate the equivalence factor s . Generally, the equivalence factor s and the co-state λ differ by means of a constant factor which needs to be considered accordingly. Based on the PMP, it is possible to calculate reference trajectories of the equivalence factor s for several driving scenarios. Further comparisons between PMP and ECMS are presented in [93, 47].

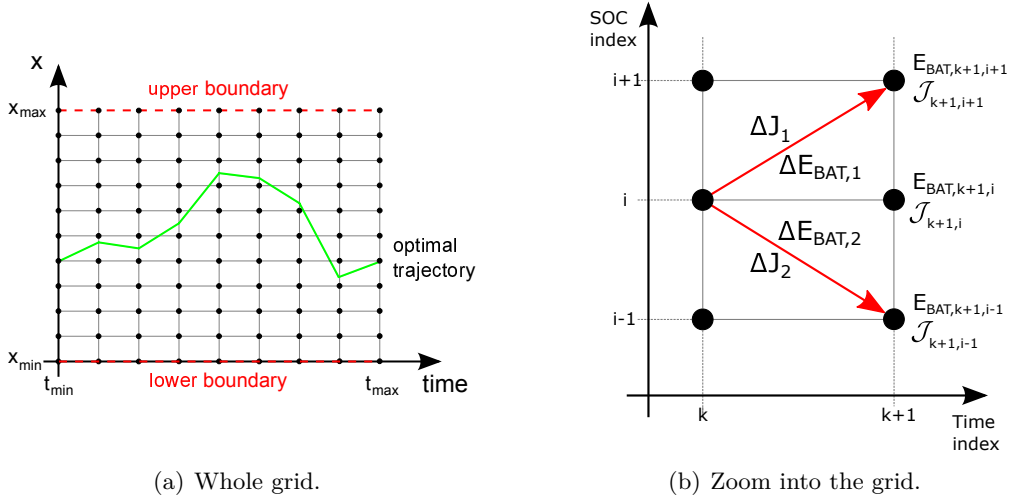
By means of the necessary conditions of optimality, which state that an optimal control variable u^* should minimize the Hamiltonian function $H(\cdot)$, it is possible to derive another relation for calculating the equivalence factor s :

$$\frac{\partial H}{\partial u} = \frac{\partial H}{\partial P_{BAT}} = \frac{\partial P_F}{\partial P_{BAT}} + s \cdot \frac{\partial P_{ECH}}{\partial P_{BAT}} \stackrel{!}{=} 0, \quad (3.40)$$

where P_F is the fuel power (mass flow rate \dot{m}_f times lower heating value H_{LV}), P_{BAT} the battery power and P_{ECH} the electrochemical power. Finally, this leads to

$$s = - \frac{\partial P_F}{\partial P_{ECH}}. \quad (3.41)$$

The DP algorithm calculates the optimal cost-to-go \mathcal{J} that in the following example describes the optimal fuel consumption f_c over time index k and state of charge SOC. The values of the cost-to-go \mathcal{J} at the grid points can be used to estimate the equivalence factor s . In Figure 3.7 a small part of the cost-to-go \mathcal{J} is depicted to show the change of fuel power P_F



(a) Whole grid.

(b) Zoom into the grid.

Figure 3.7.: Illustration of the estimation of the equivalence factor s by means of a two-dimensional grid. The indices k and i represent the discretized time and state of charge SOC, respectively. Additionally, the values of the optimal cost-to-go \mathcal{J} and the energy content of the battery E_{BAT} are stored at each grid node. Whereas the left figure generally depicts the whole grid, the right figure shows a small part in order to graphically sketch the estimation of the equivalence factor s .

and electrochemical power P_{ECH} for one given grid point. As the state grid is limited as shown in Figure 3.7(a), the equivalence factor s cannot be calculated directly at the boundaries of the state variables (x_{min} , x_{max}).

The estimation of the equivalence factor s for a given time index k and SOC index i can be mathematically described as follows:

$$s = -\frac{\partial P_F}{\partial P_{ECH}} \approx -\frac{\Delta P_F}{\Delta P_{ECH}} = -\frac{\frac{\Delta J_1}{\Delta t} - \frac{\Delta J_2}{\Delta t}}{\frac{\Delta E_{BAT,1}}{\Delta t} - \frac{\Delta E_{BAT,2}}{\Delta t}} = -\frac{\mathcal{J}_{k+1,i+1} - \mathcal{J}_{k+1,i-1}}{E_{BAT,k+1,i+1} - E_{BAT,k+1,i-1}} \quad (3.42)$$

Based on this relation, the optimal trajectory of the equivalence factor s over time can be obtained by means of the DP results.

Implementations of Equivalent Consumption Minimization Strategies

As described before, the equivalence factor s strongly influences the optimality of an ECMS. A-causal methods based on optimal control concepts allow to calculate meaningful ranges and optimal trajectories for the equivalence factor s but the results are only valid for predefined scenarios. Since the future driving conditions are generally not known in advance, only parts of the calculated off-line solutions such as initial values of the equivalence factor s_0 can be used for real-time applications. An important task of the ECMS is to appropriately adjust the equivalence factor s depending on driving situations to achieve results that are close to the optimal solution. This general approach is defined as adaptive-ECMS (A-ECMS) strategy and has been implemented in several variants [3, 38, 72, 94].

A representative sketch of an adaptive ECMS is depicted in Figure 3.8. In the central element

of this structure *Power-split*, the split between the two energy sources, ICE and battery, is calculated for a given power demand P_{DEM} and equivalence factor s . In case of the power-split u_s , lower values of the equivalence factor s lead to a preferable use of the battery and vice-versa.

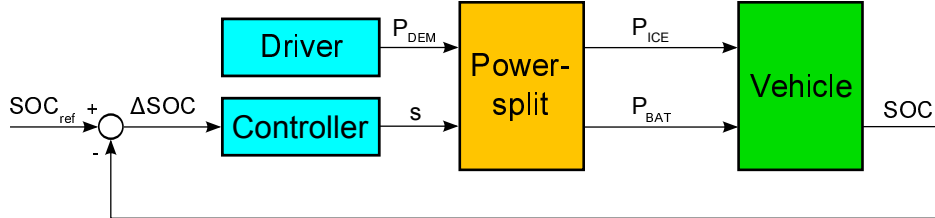


Figure 3.8.: Simplified structure of a typical adaptive ECMS-Controller. Depending on the actual battery's state of charge SOC, the controller adjusts the equivalence factor s and weights the power split between ICE and battery.

The controller is usually a PI-controller which accordingly adapts the equivalence factor. The input of the controller ΔSOC is represented by the difference between the reference SOC_{ref} and the actual SOC. Instead of PI-controllers, it is possible to use weighting functions $h(\cdot)$ for penalizing high values of ΔSOC .

As an example, the author of [51] recommended the following weighting function $h(SOC(t))$ that are similar to the form of PI-controllers:

$$h(SOC(t)) = p_p \cdot p_i = \left(1 + \left(\frac{SOC_{ref} - SOC(t)}{SOC_{ref} - SOC_{min}} \right)^{2 \cdot n_{SOC} + 1} \right) \cdot \left(1 + \tanh \left(\frac{h_{SOC_I}(SOC(t))}{SOC_{tol}} \right) \right), \quad (3.43)$$

$$h_{SOC,I}(SOC(t)) = 0.99 \cdot h_{SOC,I}(t - \Delta t) + 0.01 \cdot (SOC_{ref} - SOC(t)), \quad (3.44)$$

where p_p denotes the proportional term, p_i the integral term, SOC_{ref} the reference value of SOC, SOC_{min} the minimum value of SOC, n_{SOC} the function order, SOC_{tol} the tolerance of the hyperbolic tangent function and Δt the sampling time.

Equation 3.43 consists of two sub-functions that represent the P-correction term p_p and the I-correction term p_i , respectively. The latter contains a moving average function (Equation 3.44) to weight the effects of past deviations from SOC_{ref} . In Figures 3.9(a) and 3.9(b) variations of the proportional and integral correction terms p_p and p_i are depicted for different orders n_{SOC} and tolerance factors SOC_{tol} . The values of SOC_{ref} and SOC_{min} were defined with 65% and 50%, respectively.

Other implementations of A-ECMS integrate data of past, present or future driving conditions to improve the estimation of the equivalence factor s [91, 74, 54, 2, 107]. One technique that uses data from the past is based on the principle of pattern recognition [37, 43]. Optimal values of the equivalence factor s are pre-calculated off-line for a set of representative driving patterns, which are composed of representative driving scenarios [91]. By means of characteristic parameters such as average velocity, total time and stand-still time, the algorithm decides which representative driving pattern is closest to the current driving scenario and chooses the corresponding value of the equivalence factor s .

If predictive data such as altitude profiles of the route is available, the additional information

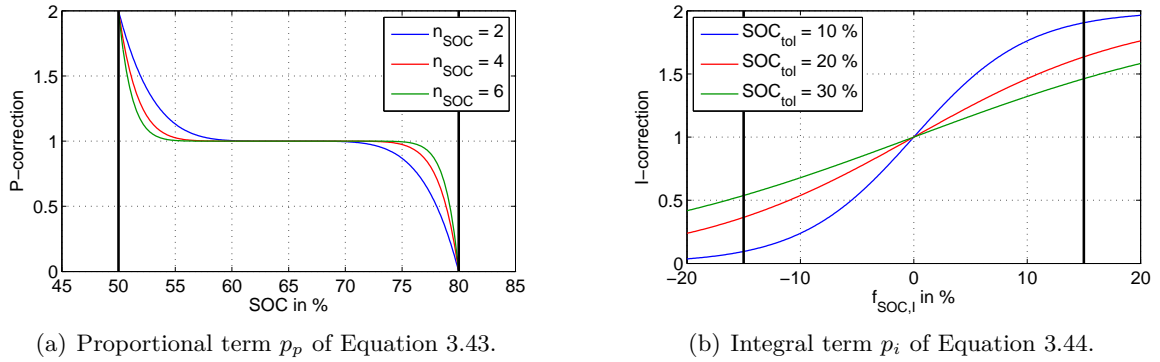


Figure 3.9.: The proportional and integral terms p_p and p_i for an adaptive ECMS and different parameters (based on [51]).

can be used to adapt the equivalence factor s . Since the slope information is a function of the distance, a velocity profile has to be defined in order to obtain the power demand P_{DEM} over time. Furthermore, information about speed limits or traffic conditions can be included to increase the accuracy of the estimation. The adaptations by means of predicted data can be characterized as a concept based on model predictive control, which is described in the following.

3.3.2. Model Predictive Control

The use of information of future driving conditions leads to the concept of model predictive control (MPC). The term MPC defines a range of control methods which make explicit use of a model of the process to calculate the control signal. The ideas, appearing in greater or lesser degree in the predictive control family, are basically [15]:

- Explicit use of a model to predict the process output at future time instants,
- Calculation of a control sequence minimizing an objective function,
- Receding strategy, so that the horizon is displaced towards the future at each instant.

The principle of MPC is to use predicted information for a given time horizon to minimize an objective function. Since it is a receding strategy, only the first control signal of the calculated sequence is applied. Afterwards, the time horizon is shifted by one time step and the optimal control strategy is calculated again with updated state and prediction information. The quality of the solution mainly depends on the predicted information as well as the applied model complexity. In terms of real-time implementations, there is a trade-off between the time horizon of predicted data and the corresponding computational effort.

As presented in Section 3.2, there are several algorithms that calculate the optimal control strategy for HEVs. In previous work, DP has been applied to solve the MPC problem for HEV applications [3]. Although non-linearities are properly handled, the solutions can only be obtained for short time horizons due to the high computational effort. Other approaches use LP and corresponding variants such as mixed-integer LP [85] to obtain the optimal control strategy. In contrast to DP, the calculation effort of such methods is quite low but in general this framework does not allow to integrate cost functions $L(\cdot)$ with higher complexity.

A meaningful compromise between model complexity and computational effort is provided by QP. It has been shown in previous work (e.g. [50]) that QP is a recommended technique for MPC in real-time operating strategies of HEVs.

3.3.3. Use of Dynamic Programming Results

Another approach for obtaining a real-time strategy is to use the optimal results of DP. For this purpose, the knowledge acquired from DP simulations over different driving conditions is statistically analysed in terms of control variables u and state variables x . In the next step, rules are extracted to construct a causal control strategy. According to the rule-based strategies described in Section 3.1, look-up tables can be used to relate typical state variables x and control variables u such as state of charge SOC, vehicle speed v , power demand P_{DEM} or power-split u_s [121, 12, 10, 11]. Although this approach is based on the optimization of several cycles, the control strategies generally represent neither optimal nor charge-sustaining behavior. To reduce these drawbacks, stochastic dynamic programming (SDP) has been applied in related work [60, 67, 27]. The corresponding results show that SDP leads to an improved operating strategy for general driving conditions.

Further approaches propose the use of concepts based on machine learning [70, 69]. By means of the results of DP, neural networks are trained to describe the operating strategy as well as to predict future driving conditions.

3.4. Summary

In this chapter the categories of state-of-the-art operating strategies for HEVs together with their pros and cons were outlined. The classification includes rule-based and optimization-based strategies as well as causal approaches for real-time applications. Since this thesis focuses on calculating different benchmarks of optimal operating strategies, only methods that allow to obtain the global optimum are suitable for this purpose. Another restriction is given by non-linear component models and cost functions $L(\cdot)$ used to describe optimization problems. Among the methods mentioned in this chapter, only the framework of DP fulfills these requirements. Due to this circumstance, DP was chosen as numerical method to solve the optimization problems. The next chapter provides a more detailed description of different variants of DP and presents the implemented DP-method of this thesis.

4. Dynamic Programming for Hybrid Electric Vehicles

In the previous chapter several methods for obtaining the optimal operating strategy of hybrid electric vehicles (HEVs) were described and compared. It has been shown that only the method of dynamic programming (DP) allows to calculate the globally optimal operating strategy for non-linear objective functions and component models. For this reason, the DP algorithm was chosen in this thesis to solve optimization problems which are presented later in Chapter 6.

This chapter focuses on the method of DP and provides an introduction to different variants and modifications in the field of HEVs. Further details and extensive derivations of several approaches can be found in [8, 9].

As stated in Equation 3.2, the DP algorithm calculates the optimal control policy

$$\pi = \{u_0^*, u_1^*, \dots, u_{N-1}^*\} \quad (4.1)$$

that minimizes the performance index

$$J(x_0, \pi) = L_N(x_f) + \sum_{k=0}^{N-1} L_k(x_k, u_k, w_k), \quad k = 0, 1, \dots, N-1, \quad (4.2)$$

where $J(x_0, \pi)$ denotes the performance index, $L_N(x_f)$ the costs of deviations from a desired final state x_f and $L_k(\cdot)$ the discrete cost function. In addition, the system dynamics of the discrete form

$$x_{k+1} = f_k(x_k, u_k, w_k), \quad k = 0, 1, \dots, N-1 \quad (4.3)$$

are integrated into the optimization problem. For this purpose, an Euler forward approximation is used in this work. In contrast to the definition in Section 3.2, additional disturbances w in the cost function $L(\cdot)$ and system dynamics $f(\cdot)$ are considered. For the classification of deterministic and stochastic dynamic programming, the properties of disturbances w are of high importance for the calculation of the optimal solution.

The definition of Equation 4.2 represents the so-called backward approach, which means that the trajectory of the optimal state variable x^* is calculated from the final state x_f to the initial state x_0 . The direction of calculation can be reversed but then the given system dynamics $f(\cdot)$ as shown in Equation 4.3 have to be inverted too. This task can be complicated if the inversion of the system dynamics $f(\cdot)$ is not unique or not analytically solvable. For example, the inversion of the system dynamics

$$x_{k+1} = x_k^2 + u_k^2, \quad (4.4)$$

leads to two solutions

$$x_k = \pm \sqrt{x_{k+1} - u_k^2}, \quad (4.5)$$

if no further restrictions of the state space \mathcal{X} are taken into account. Due to the drawbacks described above, the backward approach is denoted as the standard method of DP.

Basic Example

Before focusing on DP for HEVs, a basic example for calculating the shortest path is shown in the following. Figure 4.1(a) depicts a simple road network with representative towns A - H and corresponding distances between these towns. The goal is to calculate the shortest route between the towns A and H by means of the DP algorithm.

Instead of evaluating all possible variants, which needs exponential computational time, and afterwards taking the total minimum distance, DP can handle such problems with polynomial complexity. The reduction of calculation time is based on the principle of optimality [6] which states that all sub-trajectories of an optimal trajectory have to be optimal, too. In Figure 4.1(b) the calculation as well as the reconstruction process of the shortest path problem is shown. The algorithm starts at the final state (town H), but in this example the calculation direction can be reversed. At each town only the saved optimal cost-to-go \mathcal{J} of the previous towns and distances to reach these towns are needed to calculate the optimal path. To give an example: In town E the possible candidates of the previous towns are represented by F and G with corresponding optimal cost-to-go of $\mathcal{J}(F) = 80$ and $\mathcal{J}(G) = 90$, respectively. Thus, the overall cost-to-go \mathcal{J} at town E are either 110 (E-F) or 140 (E-G). Obviously, the minimum value is chosen to obtain the minimum distance. At the node of town E the optimal value of the cost-to-go $\mathcal{J} = 110$ as well as the previous town (F) are saved. After the last calculation step at town A, the optimal cost-to-go $\mathcal{J}(A)$, which also represents the best performance index J , are obtained and the shortest path can be easily reconstructed. Finally, the optimal sequence leading to the minimum distance between A and H is given by A-B-E-F-H.

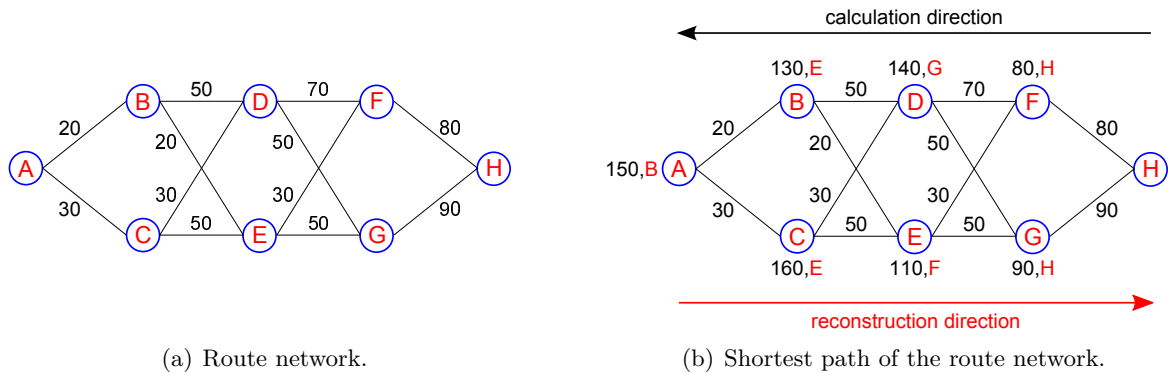


Figure 4.1.: Principle of DP: Finding the shortest path of a road network between the towns A and H.

Example for Hybrid Electric Vehicles

In the next step, the method of DP is described for HEV applications. Generally, the discretized time is chosen to define the number of stages N but the use of the discretized distance is also an option. The general formulation of Equations 4.2 and 4.3 is determined according to the requirements of HEVs.

A specific configuration of a dynamic program for obtaining the optimal operating strategy of HEV is listed in the following:

- x : State of charge SOC of the battery,
- u : Battery power P_{BAT} ,
- w : Power demand P_{DEM} ,
- $L(\cdot)$: Fuel consumption f_c .

In this example the system dynamics $f(\cdot)$ describes the state of charge at the following stage SOC_{k+1} as a function of the current state of charge SOC_k and the battery power P_{BAT} . An additional function is used to convert the engine power P_{ICE} , which depends on the power demand P_{DEM} as well as on the battery power P_{BAT} , to an equivalent fuel consumption f_c . Further, successful implementations of different DP variants for HEV applications can be found for example in [61, 76, 112].

4.1. Deterministic Dynamic Programming

The main characteristic of deterministic dynamic programming (DDP) lies in the fact that all disturbances w are known in advance. In contrast to stochastic dynamic programming, the power demand P_{DEM} of a driving scenario is exactly defined, which is the general approach for benchmarking a vehicle configuration or operating strategy.

The central calculation step of DDP is defined by minimizing the cost-to-go

$$\mathcal{J}(k, x_k) = \min_{u_k \in \mathcal{U}_k} \left(L_k(x_k, u_k, w_k) + \mathcal{J}(k+1, f_k(x_k, u_k, w_k)) \right) \quad (4.6)$$

where \mathcal{J} denotes the cost-to-go, k the index of the stage variable, $L(\cdot)$ the cost function, $f(\cdot)$ the system dynamics, x the state variables, u the control variables and w the disturbances. These calculations represent the main computational effort of the algorithm. Since the introduction of DP, the main challenge has been the high calculation effort to solve the optimization problems. Over the past decades, several approaches have been developed to reduce the computational time by means of approximation techniques. The following sections provide a brief overview of such methods in the field of HEVs. Further, more general information can be found in [38, 8, 9, 56, 62].

4.1.1. Discretization and Interpolation

Since DP is a numerical method, the discretization of state variables x and control variables u as well as the number of stages N significantly influences the calculation effort. In general, a higher discretization leads to a more accurate solution together with a higher computational time and vice-versa. By means of Equation 4.6, the complexity \mathcal{O} of a deterministic dynamic program containing one state and control variable can be determined with

$$\mathcal{O}((N-1) \cdot p \cdot q), \quad (4.7)$$

where N denotes the number of stages. Furthermore, p and q represent the discretization of the state variable x and control variable u , respectively.

If it is assumed that more than one equally discretized state variables x as well as control variables u are used, the corresponding complexity \mathcal{O} is given by

$$\mathcal{O}((N-1) \cdot p^n \cdot q^m). \quad (4.8)$$

By means of Equation 4.8, it can be seen that the complexity \mathcal{O} significantly increases. In literature, this drawback is referred to as the "curse of dimensionality" [8] but the effect can be reduced by means of approximation methods that are outlined later in Section 4.1.2.

The main calculation step of DDP that is described in Equation 4.6 consists of two terms $L_k(x_k, u_k, w_k)$ and $\mathcal{J}(k+1, f(x_k, u_k, w_k))$ which represent the costs for reaching the previous stage $k+1$ and the corresponding cost-to-go $\mathcal{J}(k+1, x_{k+1})$, respectively. Whereas the first term can be determined by the cost function $L(\cdot)$, the latter value is usually obtained by means of interpolating the cost-to-go $\mathcal{J}(k+1, x_{k+1})$. If all control variables u cause state variables x_{k+1} that exactly lie on the grid nodes of stage $k+1$, then the interpolation can be avoided and consequently, the calculation effort is reduced. The described variants of the calculation step are depicted in Figures 4.2(a) and 4.2(b).

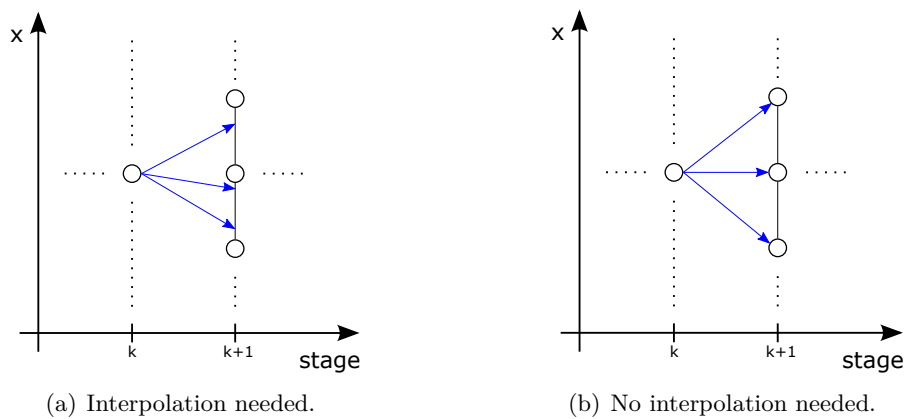


Figure 4.2.: Two possible cases can occur during a one-dimensional calculation step at stage k : In general, the cost-to-go $\mathcal{J}(k+1, x_{k+1})$ have to be interpolated but if the control variables u cause state variables x_{k+1} that exactly lie on the grid nodes of stage $k+1$, then the interpolation can be avoided.

Until now, the central calculation step of DDP has been described for one state and control variable but the principles remain the same for state spaces \mathcal{X} with higher dimensions. In Figures 4.3(a) and 4.3(b) the possible variants to determine the cost-to-go $\mathcal{J}(k+1, x_{k+1})$ are depicted for two state variables x and control variables u .

4.1.2. Modifications of Dynamic Programming

To reduce the impact of the "curse of dimensionality", several methods were developed which include for example the approach of iterative dynamic programming as well as the boundary-line method. All of these modifications have in common that they reduce the calculation effort to solve the optimization problem. Unfortunately, most of these methods cannot guarantee the global optimality. However, modifications of DP provide a trade-off between the accuracy of the calculated solution and the computational time and therefore are of central interest in many applications [80, 8, 9, 62].

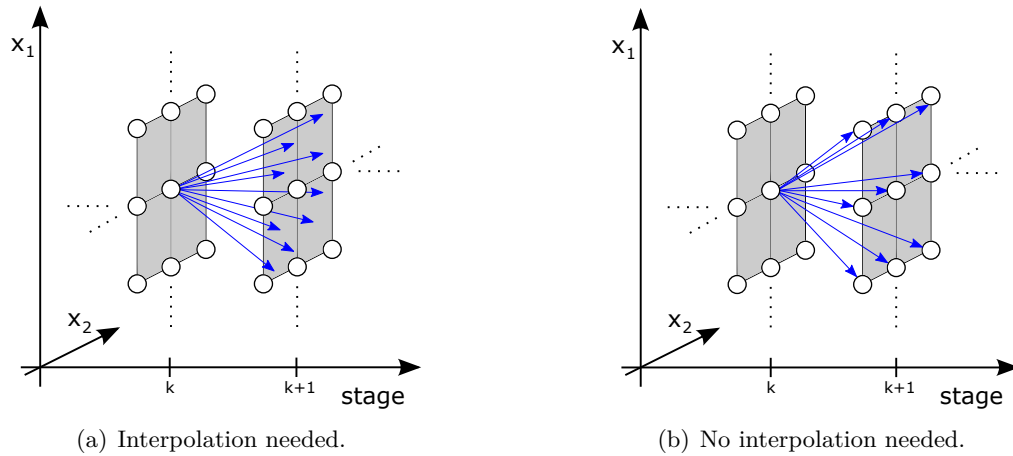


Figure 4.3.: Two-dimensional calculation step at stage k : As the one-dimensional case the cost-to-go $\mathcal{J}(k+1, x_{k+1})$ of the stage $k+1$ have to be interpolated in general but if the control variables u cause state variables x_{k+1} that exactly lie on the grid nodes of stage $k+1$, then the interpolation can be avoided.

Iterative Dynamic Programming

Compared to the classic DDP approach, the concept of iterative dynamic programming (IDP) reduces the calculation time as well as the memory usage. It has been successfully applied in different areas of science [62, 56] including the optimization of HEVs [113].

The basic idea of this method is to start with a coarse grid and calculate the corresponding optimal trajectory. In the next step, the grid around the previous optimal trajectory is restricted by means of an adjustable grid reduction factor. The next iteration refines the reduced grid and calculates the optimal trajectory again. This procedure is repeated until a sufficient convergence of the solution is obtained. Instead of calculating the solution by means of a very fine grid, this method allows to efficiently reduce the calculation time. The definition of the grid reduction factor strongly influences the convergence as well as the optimality of the method. In general, a high value of the grid reduction factor provides a fast convergence with a higher deviation of the global optimum and vice-versa. In Figures 4.4(a) - 4.4(d), the principle of IDP is sketched by means of different iterations.

Boundary-line method

Another method to extend the classical DP approach is to use the boundary-line method [101]. In contrast to other modifications of DP, this method not only reduces the calculation time but also allows to calculate the global optimum. Starting from the initial state x_0 as well as from the end state x_f , the algorithm calculates the boundaries of feasible state space regions by means of applying the minimum and maximum control variables (u_{min} , u_{max}), respectively. Afterwards, a new grid excluding infeasible states is defined and used for the optimization. Especially for a small number of stages N the boundary-line method significantly reduces the computational effort. Figure 4.5 depicts the principle of the boundary-line method for one state variable x . In addition, it has been shown that the boundary-line algorithm can also be applied to a state space \mathcal{X} with higher dimensions [26, 28]. For this purpose, the boundaries of the state variable (x_{min} , x_{max}) are described by means of level-set functions.

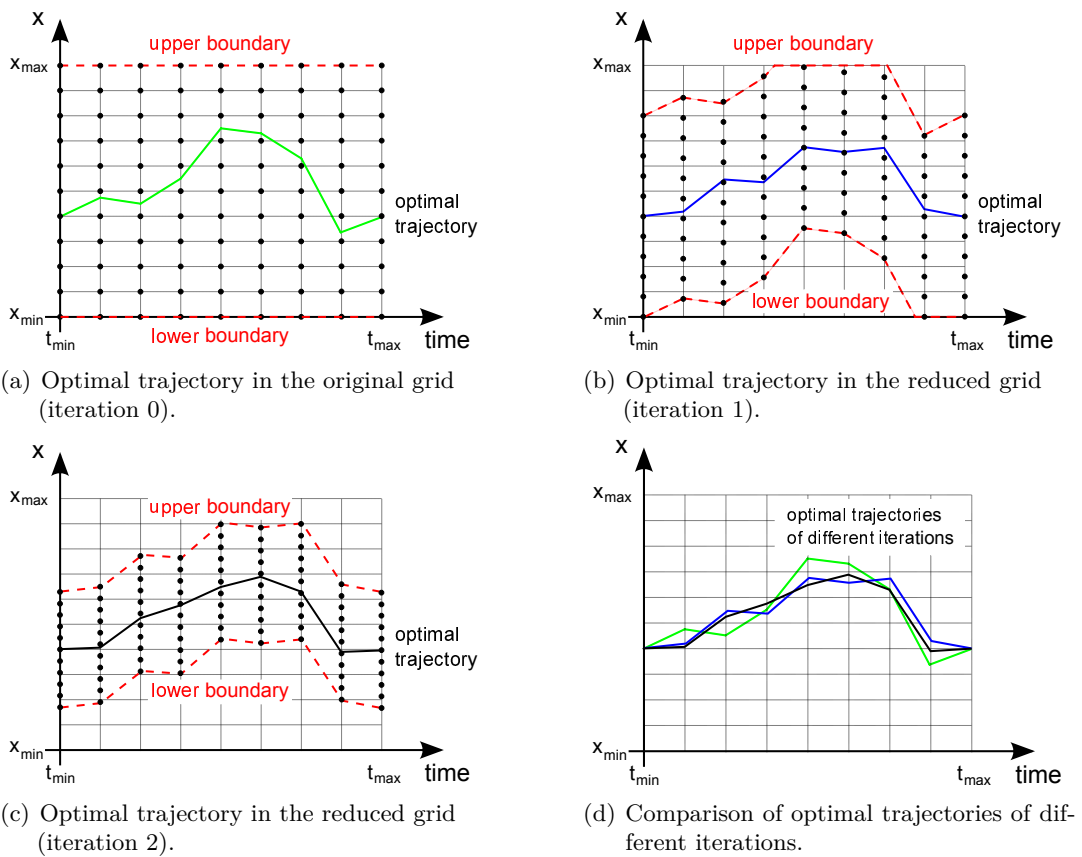


Figure 4.4.: Principle of IDP. Firstly, the optimal trajectory is calculated by means of a coarse grid. In the following iterations the state space \mathcal{X} is reduced and refined around the previous trajectory. Compared to a fine discretization of the whole grid, this method allows to reduce the calculation time.

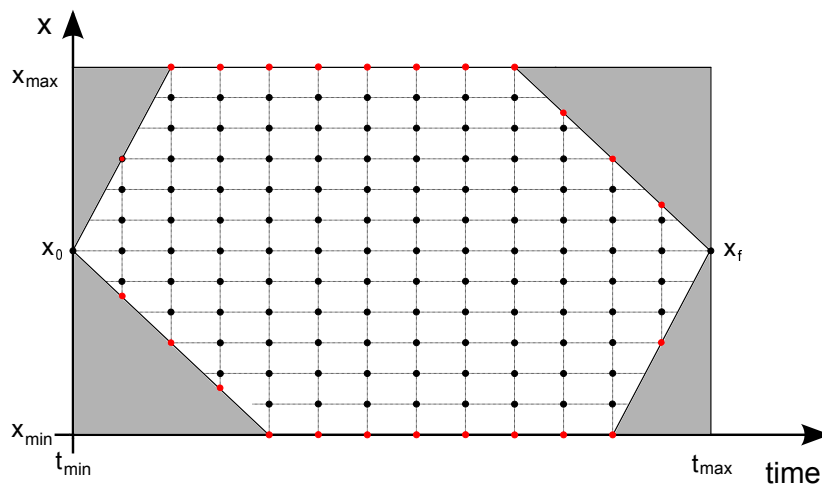


Figure 4.5.: Boundary-line method for one state variable x . The algorithm calculates extremal state values that describe the boundaries of the feasible state space \mathcal{X} . The grey regions are not feasible and consequently excluded in the optimization. Usually, the boundary line is integrated into the new grid (red points).

Further Variants

A further class of DP methods approximates the cost-to-go \mathcal{J} of all grid points in order to obtain a lower computational time as well as to reduce the memory requirements [80]. By means of polynomials the shape of the cost-to-go matrix can be fitted and instead of saving the whole grid, only the corresponding coefficients have to be stored. Especially if the matrix has a convex shape, a low order of the polynomials is sufficient to obtain high accuracy. Based on these approximations with polynomials, it has been shown that the central calculation step of DP (Equation 4.6) can be transformed into a local optimization problem [57]. By means of this approach it is possible to avoid the evaluation of all discretized control variables $u \in \mathcal{U}$ and directly calculate the optimal control variable u^* . The demonstration by means of one state variable x shows a significantly lower computation time and an accuracy which is still close to the global optimum.

A further method described in [113] avoids to save the path matrix containing the optimal control variables u^* of each grid point. As this path matrix is mainly used to reconstruct the trajectories of the optimal state variable x^* , another approach is taken into account. For this purpose, the optimal control variable u^* is obtained by means of the cost-to-go matrix together with a local optimization problem. This approach is related to MPC and needs, especially in combination with an approximated cost-to-go matrix, very low memory compared to the reference case.

4.2. Stochastic Dynamic Programming

DDP assumes that all disturbances w are exactly defined for a given optimization problem. If only the stochastic properties of occurring disturbances w are known, which represents a more general approach, another method called stochastic dynamic programming (SDP) is recommended to obtain optimal solutions. As a restriction, it is assumed that the disturbances w can be described by means of Markov chains. For this purpose, all corresponding transition probabilities have to be known in advance.

The goal of the optimization is to obtain a control policy $\pi(x_k)$ which considers probabilities in terms of the disturbances w . As an example in the field of HEVs, the authors of [84] use the following performance index

$$J(x_0, \pi(x_k)) = E_{w_k} \left\{ L_N(x_N) + \sum_{k=0}^{N-1} L_k(x_k, \pi(x_k), w_k) \right\}, \quad (4.9)$$

where $E\{\cdot\}$ denotes the expected value, L the cost function, x the state variable, w the disturbances and $\pi(x_k)$ the control policy for a given state variable x .

For high values of the number of stages N , the Functional 4.9 can be seen as an infinite horizon problem. In such problems, the optimal costs do not depend on the initial state x_0 as the resulting costs determined by means of the performance index are always the same. Thus, a stationary cost-to-go $\mathcal{J}_k(x_k)$ can be calculated which is not a function of time [27, 9]:

$$\mathcal{J}(k, x_k) = \mathcal{J}(k + 1, x_k). \quad (4.10)$$

The intermediate calculation step of the SDP becomes implicit with

$$\mathcal{J}(k, x_k) = \min_{\pi(x_k)} \left(E_{w_k} \left\{ L_k(x_k, \pi(x_k), w_k) + \gamma \cdot \mathcal{J}(k, f_k(x_k, \pi(x_k), w_k)) \right\} \right), \quad (4.11)$$

where γ , $0 < \gamma < 1$, is usually used as discount factor to ensure the convergence of $\pi(x_k)$.

To solve Equation 4.11 as well as to obtain the optimal stationary control policy $\pi(x_k)$, an iterative method is usually chosen. Amongst several approaches, representative algorithms are based on value iteration or policy iteration. Whereas the latter shows a faster convergence, the former guarantees global optimality. Further information and derivations are provided by [9].

Based on simulation results, it has been successfully shown that SDP can be applied to obtain optimal control strategies for HEVs [84, 44, 59, 67]. The calculated stationary control policies $\pi(\cdot)$ are stored by means of look-up tables which can be easily integrated within a simulation framework. Beside the reduction of fuel consumption f_c , further approaches were implemented to minimize a weighted sum of emissions [60]. In addition to simulation studies, the author of [27] also validated the control strategy by means of a hybrid bus and demonstrated the use of SDP in practice.

4.3. Summary

In this chapter different variants of DP were described. Since prescribed driving cycles are used for different case studies, the stochastic approach was excluded in this thesis and DDP was chosen to calculate the globally optimal operating strategy.

In order to fulfill the requirements of several optimization problems, a general framework for DDP was set up. In addition, the method of IDP was included to reduce the calculation effort. As in various related work the code was written in MATLAB[®], but unfortunately this language is known to be quite slow in terms of handling for-loops. This fact leads to very high computational times for optimization problems with high-dimensional state spaces \mathcal{X} . To reduce this drawback as well as to keep the flexibility of MATLAB[®], the core of the algorithm was written in C/MEX code. It turned out that especially in case of parameter studies the overall calculation time was reduced by a factor of up to 20 compared to a complete implementation in MATLAB[®].

5. Model of a Hybrid Electric Bus

A model of a HEV is used in order to assess the performance of operating strategies by means of simulations. Due to the generality of the operating strategies derived within this work, the vehicle type as well as the hybrid topology can be selected without any limits.

This thesis focuses on optimal operating strategies of HEVs for defined driving cycles. As the resulting strategies are optimized for these driving scenarios, a vehicle type used for similar driving cycles over the total life span depicts a representative application. In order to fulfill this requirement, a model of a hybrid bus in public transport was chosen.

Hybrid buses usually use either a parallel (e.g.[110]) or a series hybrid topology (e.g.[31]). Since the methodologies developed in this thesis do not directly depend on hybrid topologies, a series topology was selected. The bus model consists of several components and describes its main functionalities such as power split, recuperation and given component limits.

The following sections depict the parameters and characteristics of the considered component models in detail.

5.1. Vehicle

Figure 5.1 shows a photograph of the vehicle model which is based on a *Volvo 7700* hybrid bus in a two-axle configuration.



Figure 5.1.: Photograph of a Volvo 7700 hybrid bus [14]. The corresponding parameters are used for the vehicle model of this thesis.

5.1.1. Model description

The total weight of the bus model is defined as a constant parameter. Due to this assumption, the influence of different numbers of passengers is neglected. Furthermore, the total weight is defined for a reference configuration with corresponding sizes of battery and engine-generator unit. In order to consider energy sources that differ from these reference sizes, the total weight of the vehicle needs to be adapted accordingly. The consideration of scaled components is particularly important in terms of determining the optimal sizes of energy sources.

5.1.2. Characteristics

Table 5.1 shows the parameters of the vehicle model used in this work and lists the corresponding values of vehicle mass m , drag coefficient c_w , reference area A as well as maximum velocity v_{max} .

Table 5.1.: List of vehicle parameters.

constant parameters	symbol	value	unit
vehicle mass	m	18.9	t
drag coefficient	c_w	0.9	-
reference area	A	8.1	m ²
maximum velocity	v_{max}	80	km/h

5.2. Tire and Gear Box

This section describes the parameters of tire and gear box which are part of the drivetrain.

5.2.1. Model description

The tire model of the hybrid bus contains a kinematic approach. Hence, the tire parameters are defined by means of the wheel radius r and the rolling friction coefficient f_r . The tire model used is sufficient for the analysis of power flows and neglects further effects like slips due to differences between bus and wheel speeds.

Based on the maximum speed of the electric traction motors ($n_{max} = 10000$ rpm) and the bus ($v_{max} = 80$ km/h), the gear ratio i_g of the three-speed gear box is calculated as follows

$$i_g = \frac{10^4 \text{ rpm} \cdot \pi \cdot 0.45 \text{ m} \cdot 3.6}{30 \cdot 80 \text{ km/h}} = 21.2 . \quad (5.1)$$

Furthermore, a brake model is necessary in order to fulfill negative power demands of the driving cycles which exceed the maximum recuperation power. Because of safety reasons, it is assumed that the mechanical brakes provide all requested torque demands M_{DEM} if no recuperation is considered. Due to this simplified brake model, effects such as brake pad wear are neglected.

5.2.2. Characteristics

Table 5.2 depicts the parameters of gear box and tire.

Table 5.2.: List of gear box and tire parameters.

constant parameters	symbol	value	unit
ratio of the three-speed gear box	i_g	21.2	-
gear box efficiency	η_g	0.92	-
wheel radius	r	0.45	m
rolling friction coefficient	f_r	0.007	-

5.3. Electric Motor

The bus model consists of one driving axle which contains two identical electric traction motors in order to propel the bus as well as to recuperate energy.

5.3.1. Model description

The model of the electric motor (EM) is based on measurement data and has a maximum speed n_{max} of 10000 rpm. In order to obtain a more general model, the maximum continuous torque $M_{cont,max}$ depicts a scalable parameter. As the model of the EM is only given for the propulsion mode, an extension is necessary to represent the generator mode. The maximum torque curves over speed are assumed to be symmetric in both modes. In order to determine the efficiencies of the generator mode η_{gen} , symmetric losses $P_{LOSS,EM}$ are taken into account. The following Equations 5.2 - 5.6 briefly describe the approach.

$$P_{LOSS,EM,gen} = P_{LOSS,EM,mot}, \quad (5.2)$$

$$P_{MECH,gen} - P_{EL,gen} = P_{EL,mot} - P_{MECH,mot}, \quad (5.3)$$

Furthermore, the absolute values of the mechanical power $P_{MECH,mot}$ and $P_{MECH,gen}$ are assumed to be the same.

$$P_{MECH} - \eta_{gen} \cdot P_{MECH} = \frac{P_{MECH}}{\eta_{mot}} - P_{MECH}, \quad (5.4)$$

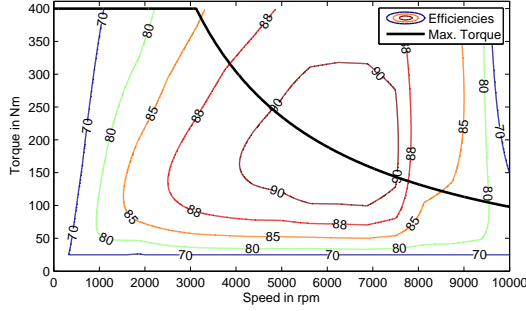
$$1 - \eta_{gen} = \frac{1}{\eta_{mot}} - 1, \quad (5.5)$$

$$\eta_{gen} = 2 - \frac{1}{\eta_{mot}}. \quad (5.6)$$

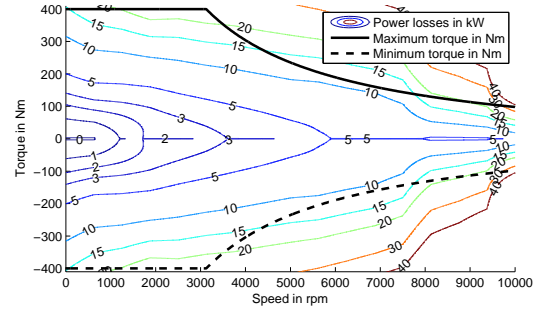
On the basis of Equation 5.6, the efficiencies between motor mode η_{mot} and generator mode η_{gen} can be converted. However, the use of efficiency maps leads to the drawback that undefined efficiency values η occur for a mechanical power P_{MECH} of zero. To avoid this circumstance, maps containing power loss $P_{LOSS,EM}$ over speed n and torque M are used in this work. For this purpose, the efficiency maps are converted into power loss maps. In order to determine the power loss $P_{LOSS,EM}$ on the axes (speed $n = 0$, torque $M = 0$), the original power loss map is extrapolated accordingly.

5.3.2. Characteristics

Figure 5.2(a) shows the efficiency map and the maximum continuous torque curve of the electric motor. Figure 5.2(b) depicts the power loss map of the motor and generator modes. As described before, symmetric maximum torque curves over speed as well as symmetric power loss $P_{LOSS,EM}$ are assumed.



(a) Efficiency map of the EM (propulsion mode).



(b) Power loss map of the EM.

Figure 5.2.: Efficiencies η and power loss $P_{LOSS,EM}$ of the EM. The left figure depicts the efficiency map of the EM in the propulsion mode. The generator efficiencies η_{gen} are calculated by means of symmetric power loss $P_{LOSS,EM}$. As the efficiencies η cannot be defined for a mechanical power P_{MECH} of zero, the power loss map of the right figure is used. The power loss $P_{LOSS,EM}$ on the axes (speed $n = 0$, torque $M = 0$) are obtained by means of extrapolating the original map.

Table 5.3 depicts the parameters of the EM. Whereas the number of traction motors N_{EM} and the maximum speed n_{max} are constant, the maximum continuous torque $M_{cont,max}$ represents the scalable parameter. As the corner speed n_{cor} of the EM remains constant, the maximum continuous power $P_{EM,cont,max}$ is implicitly defined.

Table 5.3.: List of EM parameters.

constant parameters	symbol	value	unit
number of traction motors	N_{EM}	2	-
maximum speed	n_{max}	10^4	rpm
corner speed	n_{cor}	3120	rpm
scaled parameters	symbol	reference value	unit
maximum continuous torque	$M_{cont,max}$	400	Nm
maximum continuous power	$P_{EM,cont,max}$	130.7	kW

5.4. Battery

Besides the engine-generator unit, the battery represents the second energy source of the hybrid electric bus.

5.4.1. Model description

In order to model the electrical behavior of the battery, a pack based on a single cell type "Kokam SLPB 100216216H" [25] is built. As the nominal voltage U_{NOM} of the vehicle's electrical system is defined by 360 V, the number of serial cells is implicitly given by 96. In order to describe the battery dynamics, a equivalent circuit model is used. It contains the open-circuit voltage U_{OC} as well as an internal resistance R_{BAT} and is depicted in Figure 5.3.

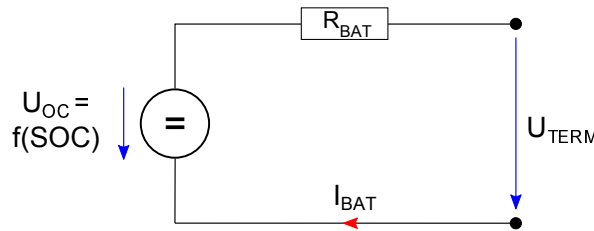


Figure 5.3.: Equivalent circuit model of the battery.

Figure 5.4(a) shows the measured terminal voltage U_{TERM} of the cell over the depth of discharge for different C-rates. By means of these discharge curves, the internal resistance R_{BAT} is estimated which leads to the following equation

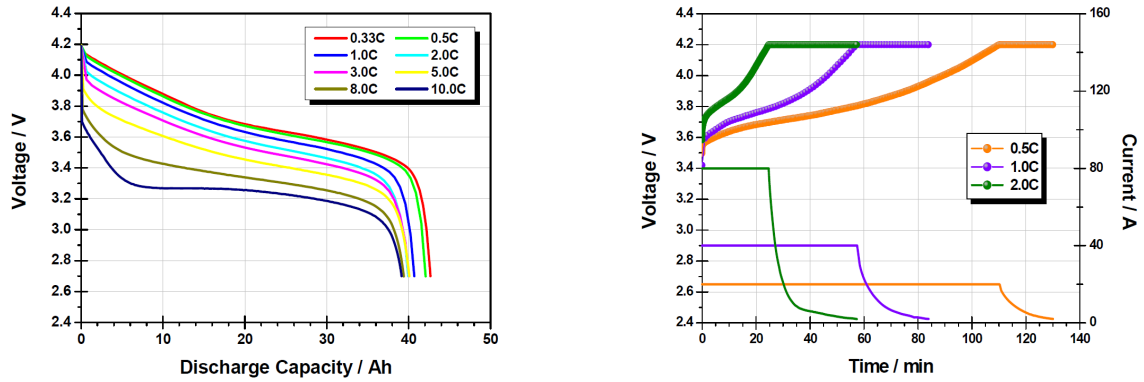
$$\hat{R}_{BAT} = \frac{\Delta U}{\Delta I} = \frac{U_{C_1} - U_{C_2}}{(C_1 - C_2) \cdot C_{BAT}}, \quad (5.7)$$

where U_C denotes the terminal voltage U_{TERM} at a corresponding C-rate and C_{BAT} the capacity of the battery. The mean value of the estimated internal resistances \hat{R}_{BAT} is used to determine the internal resistance R_{BAT} as well as to calculate the power loss $P_{LOSS,BAT}$ of the battery. In contrast to related work [38, 101], the charging of the battery is modeled in more detail. For this purpose, the maximum charge current I_{CH} depends not only on the maximum charging C-rate C_{CH} but also on the maximum open-circuit voltage $U_{OC,max}$. Figure 5.4(b) shows the described characteristic for different C-rates.

5.4.2. Characteristics

Figure 5.4(a) depicts typical measured discharging curves of the cell for different C-rates. The open-circuit voltage U_{OC} is estimated by means of the terminal voltage U_{TERM} of the lowest C-rate corrected by the corresponding voltage drop at the internal resistance R_{BAT} . Figure 5.4(b) shows the reduction of the charge current I_{CH} as well as the limited terminal voltage U_{TERM} over time. This behavior is also included into the battery model.

Table 5.4 depicts the parameters of the battery pack. The maximum C-rate for charging C_{CH} and discharging C_{DIS} , the number of serial cells N_{CELLS} , the minimum voltage U_{min} , the nominal voltage U_{NOM} , the maximum voltage U_{max} and the specific heat capacity c_p are



(a) Discharge curves for different C-rates [25].

(b) Charge curves for different C-rates [25].

Figure 5.4.: Discharge and charge curves for different C-rates of the battery.

assumed to be constant. To obtain a scalable battery model, the capacity C_{BAT} is considered as adjustable parameter. The internal resistance R_{BAT} as well as the mass m_{bat} are implicitly scaled by means of the battery capacity C_{BAT} .

Table 5.4.: List of battery pack parameters.

constant parameters	symbol	value	unit
maximum C-rate (discharge)	C_{DIS}	10	1/h
maximum C-rate (charge)	C_{CH}	3	1/h
number of cells	N_{CELLS}	96	-
minimum voltage	U_{min}	270.3	V
nominal voltage	U_{NOM}	360	V
maximum voltage	U_{max}	417.8	V
specific heat capacity	c_p	650	J/(kg · K)
scaled parameters	symbol	reference value	unit
capacity	C_{BAT}	40	Ah
internal resistance of a 40 Ah cell	R_{BAT}	134.4	mΩ
mass of the battery pack	m_{bat}	130	kg

5.5. Power Electronics

The component power electronics (PE) represents the link between the EM and the high-voltage vehicle's electrical system.

5.5.1. Model description

The model considers the efficiency η as function of the input power P_{PE} . By means of the power flow direction, the input power P_{PE} is either taken from the vehicle's electrical system

in case of propulsion or from the EM in case of recuperation. Furthermore, the model uses the same efficiency characteristics for both power flow directions.

5.5.2. Characteristics

Figure 5.5 shows the generic function which describes the efficiency η of the PE depending on the input power P_{PE} . In order to obtain a scalable model, the maximum input power $P_{PE,max}$ can be adjusted. Table 5.5 depicts the corresponding reference value.

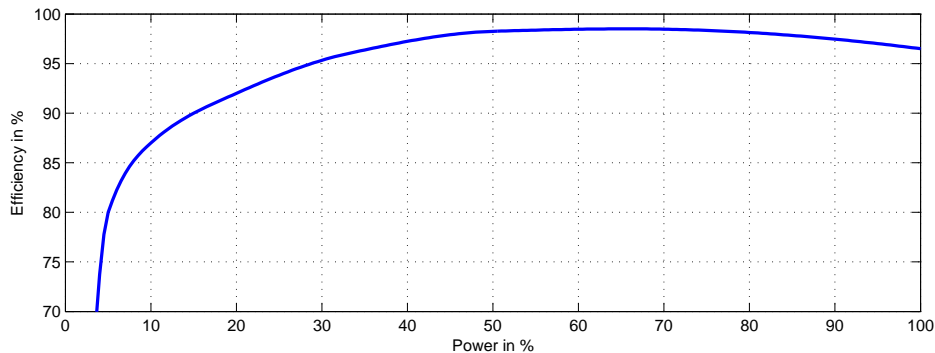


Figure 5.5.: Efficiency η of the power electronics depending on the input power P_{PE} .

Table 5.5.: List of power electronics parameters.

scaled parameters	symbol	reference value	unit
maximum input power	$P_{PE,max}$	200	kW

5.6. Engine-Generator Unit

Due to the chosen series topology of the hybrid bus, the primary energy source is represented by means of the engine-generator unit (EGU).

5.6.1. Model description

The EGU consists of an ICE, gear box, generator and PE. The gear box converts torques M as well as rotational speeds n between ICE and generator. Based on the maximum torque curves of ICE and generator, the ratio of the gear box i_g is defined by 0.5. The generator and the PE are modeled as described in Sections 5.3 and 5.5, respectively.

Due to the series hybrid topology, the EGU is decoupled from the vehicle speed v . Thus, the combination of torque M and speed n to obtain a required electrical EGU power P_{EGU} can be chosen arbitrarily. In terms of a low fuel consumption f_c , the load point with the maximum efficiency η_{max} is selected for a demanded electrical EGU power P_{EGU} . This approach provides an optimal relation between electrical EGU power P_{EGU} and maximum efficiency η_{max} .

5.6.2. Characteristics

Figure 5.6(a) depicts the efficiency map of the EGU. For this purpose, all component efficiencies η of the package are projected to the efficiency map of the ICE. In addition to the calculated efficiencies η of the EGU, the optimal load points leading to minimum fuel consumption f_c are depicted for a given electrical EGU power P_{EGU} . Figure 5.6(b) shows the corresponding function which represents the maximum efficiency η_{max} over the electrical EGU power P_{EGU} .

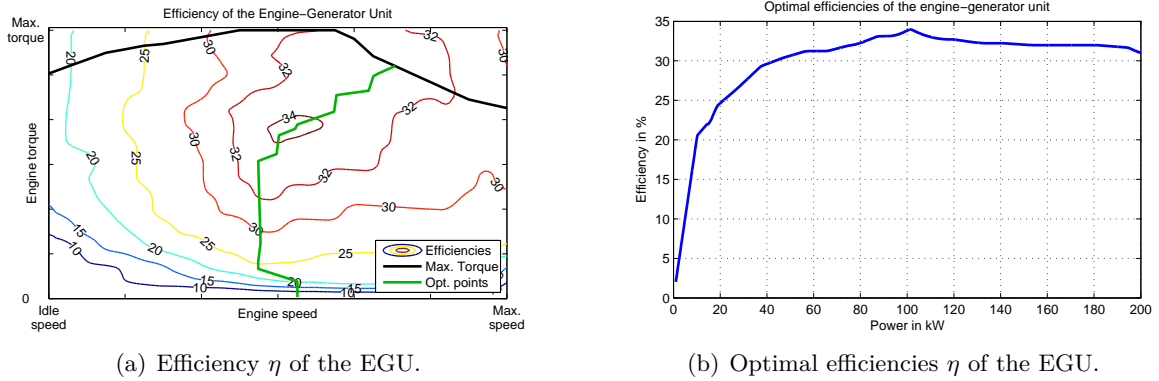
(a) Efficiency η of the EGU.(b) Optimal efficiencies η of the EGU.

Figure 5.6.: Efficiency η of the EGU. Based on the efficiencies of the overall package, the load points with maximum efficiency η_{max} for a given electrical EGU power P_{EGU} are used.

Table 5.6 shows the parameters used to obtain different sizes of the EGU. By means of the maximum electrical EGU power $P_{EGU,max}$, the function of Figure 5.6(b) as well as the mass m_{EGU} of the package are linearly scaled.

Table 5.6.: List of engine-generator unit parameters.

scaled parameters	symbol	reference value	unit
maximum electrical EGU power	$P_{EGU,max}$	200	kW
mass	m_{egu}	440	kg

5.7. Summary

In this chapter, the component models of a hybrid electric bus were described which include the vehicle, tire, gear box, EM, battery, EGU and PE. For this purpose, the characteristics of the models as well as the scalable and constant parameters of each component were presented. In the next chapter, the bus model is applied to demonstrate novel approaches in terms of optimal operating strategies and component sizing.

6. Approaches for Optimal Energy Management

The previous Chapter 5 has described the components of a series hybrid bus in detail and specified the characteristics, the parameters as well as the possible scaling of components. The current chapter demonstrates novel approaches of optimal energy management for hybrid electric vehicles by means of simulation studies.

In order to provide the reader a brief overview, the sections of this chapter can be categorized as follows:

- Section 6.1 focuses on the optimization method and defines a set of reference parameters used in the methodologies of this work,
- Section 6.2 and 6.3 deal with the optimal component sizing of energy sources and electric motors, respectively,
- The remaining sections describe approaches for optimal operating strategies which consider cost-optimal (Section 6.4) as well as energy-optimal approaches including component limits (Section 6.5 and 6.6).

As methodologies for optimal operating strategies and component sizing are developed in this thesis, an algorithm to calculate the global optimum is mandatory. Since no simplifications of the component models described in Chapter 5 are taken into account, only the method of dynamic programming (DP) guarantees the calculation of the global optimum.

All the methodologies of this work which either deal with optimal component sizing or optimal operating strategies are described on the basis of stand-alone approaches. These approaches can be combined in order to define further optimization problems but in that case, limits of the optimization method like the "curse of the dimensionality" need to be taken into account.

In this work, a model of a series hybrid bus is used to demonstrate the developed methodologies by means of simulation studies. Figure 6.1 sketches a simplified version of the bus model and graphically highlights the components and effects considered by the methodologies. According to the description of Section 5.6, Figure 6.1 considers a general representation of the EGU which contains a gear box. However, if the maximum power of ICE and generator is obtained at the same rotational speeds n , then the gear box can be removed leading to an improved efficiency η .

Although a model of a series hybrid bus is applied for the simulation studies, the framework of the methodologies developed in this work also allows to integrate further hybrid topologies and vehicle types. For this purpose, the number of components as well as their corresponding parameters need to be adjusted appropriately.

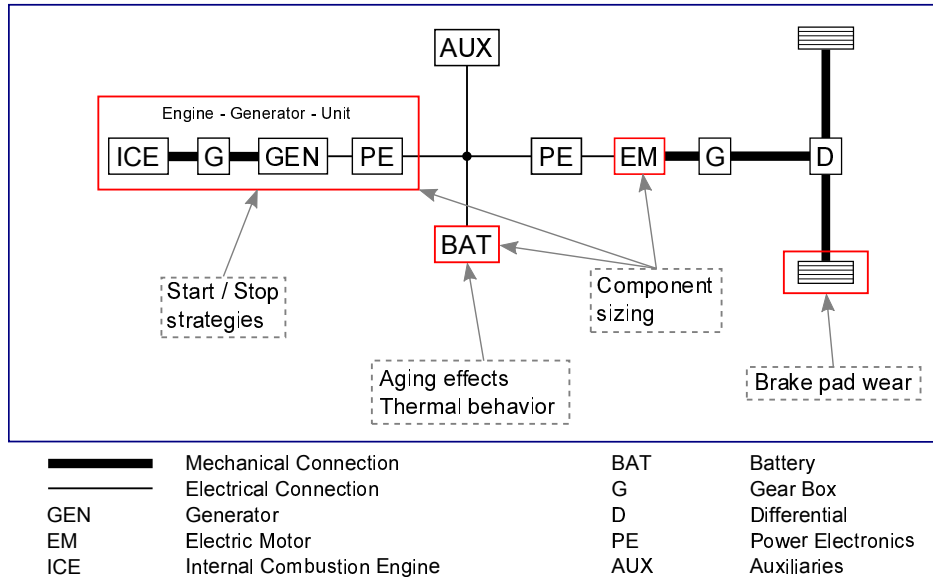


Figure 6.1.: Simplified model of a series hybrid bus. The figure highlights the components which are used to demonstrate the methodologies developed in this thesis.

In the following, the structure of this chapter is outlined:

- **Section 6.1: Reference simulations**

A reference configuration of the hybrid bus is used to evaluate the influence of specific parameters of the dynamic program. Furthermore, parameters such as the initial state of charge SOC_0 or the discretizations of state variables Δx and control variables Δu are determined for the simulation studies.

- **Section 6.2: Sizing of energy sources**

This section presents a methodology for the optimal sizing of the traction energy sources. For the demonstration, a set of optimal sizes of EGU and battery is calculated. By means of further parameters like initial component costs ($c_{comp,egu}$, $c_{comp,bat}$) or fuel costs c_{fuel} , the optimal configuration can be selected.

- **Section 6.3: Sizing of electric motors**

In addition to the sizing of energy sources, this section deals with the optimal sizing of EMs in HEV applications. The methodology is demonstrated by means of sizing the electric traction motors on the basis of standard operating modes.

- **Section 6.4: Cost-optimal operating strategies**

In this section, cost-optimal operating strategies are calculated in order to minimize operating costs c_{op} and life cycle costs c_{life} of HEVs. Beside the fuel consumption f_c , the approach considers cyclic and calendaric battery aging as well as brake pad wear.

- **Section 6.5: Operating strategies including thermal effects**

A further approach for optimal operating strategies is developed which not only minimizes the fuel consumption of HEVs but also considers temperature limits of the battery.

- **Section 6.6: Operating strategies for the engine-generator unit**

The last section deals with optimal operating strategies for the EGU. The methodology allows to penalize the number of engine starts N_{START} by means of a time-based approach.

6.1. Reference Simulations

This section presents the results of different reference simulations in order to determine specific parameters of the DP algorithm. As described before, the simulation model is based on a series hybrid electric bus and uses a reference configuration containing

- A battery capacity C_{BAT} of 40 Ah,
- A maximum power of the engine-generator unit $P_{EGU,max}$ of 160 kW,
- A constant power P_{AUX} of 10 kW to consider auxiliary devices.

Furthermore, representative driving cycles for buses were chosen by means of the *Braunschweig city driving cycle*, the *Manhattan bus cycle* and the *Orange County bus cycle*. The corresponding velocity profiles over time are shown in Appendix D.

Table 6.1 compares representative characteristics of these driving cycles such as mean power, maximum power, maximum velocity or length. The value of the mean power is an important parameter to roughly estimate the fuel consumption f_c . Compared to the other driving cycles, the Manhattan bus cycle contains the lowest mean power and lowest maximum velocity.

Table 6.1.: General characteristics of the driving cycles used in this thesis.

characteristic	unit	Braunschweig bus cycle	Manhattan bus cycle	Orange County bus cycle
mean power [†]	kW	32.2	17.7	28.3
maximum power	kW	229.2	220.8	191.6
mean velocity	km/h	22.5	11.0	19.8
maximum velocity	km/h	58.2	40.5	65.4
duration	s	1740.0	1089.0	1909.0
length	km	10.9	3.3	10.5
idling time	s	442.0	374.0	407.0

[†] The mean value of the power at the wheels P_W combined with no recuperation of braking energy is taken into account.

The DP algorithm is applied in order to calculate the global optimum of operating strategies and component sizes. Unfortunately, the initial parameters of a dynamic program such as the discretization of state variables Δx and control variables Δu are not known in advance and strongly depend on the optimization problem. Fine discretizations lead to a higher accuracy of the solution as well as to higher calculation times and vice-versa. Therefore, these contrary items, accuracy and low computational effort, should be taken into account to appropriately configure a dynamic program. By means of comparing the results of several parameter variations, a set of initial parameters is determined. The initial and final values of the battery's state of charge (SOC_0 and SOC_f) depict further parameters which influence the calculation of the operating strategy.

The optimization problem of this section is summarized as follows:

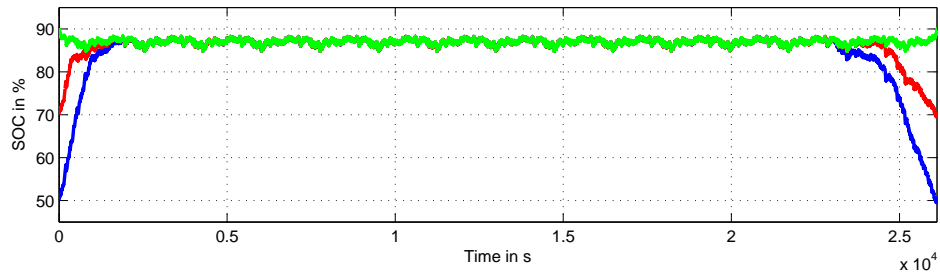
$$\begin{aligned}
& \min_{u_k \in \mathcal{U}_k} \sum_{k=0}^{N-1} \dot{m}_f(u_k, x_k, w_k) \cdot \Delta t \\
& \text{s.t.} \\
& x_{k+1} = \frac{u_k \cdot \Delta t}{C_{BAT} \cdot 3600} + x_k \\
& 0 \leq x_k \leq 1 \\
& -120 \leq u_k \leq 400 \\
& x_0 = SOC_0 \\
& x_f = SOC_0 \\
& x_k \in \mathcal{X}_k \\
& u_k \in \mathcal{U}_k
\end{aligned}$$

The battery current I_{BAT} is used as control variable u_k , the battery's state of charge SOC as state variable x_k and the power demand P_{DEM} as disturbance w_k . In addition, limits of the control and state variables as well as a sampling time Δt of 1 s are considered. The initial state of charge SOC_0 depicts a parameter which is optimized in this section.

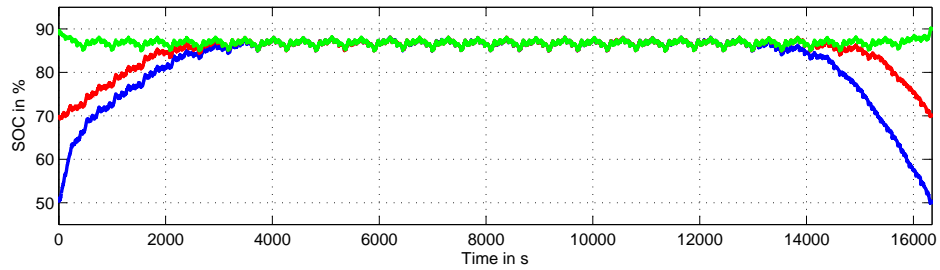
As the battery of the modeled bus cannot be charged externally, charge-sustaining operating strategies need to be implemented, which leads to equal values of the initial and final state of charge (SOC_0 and SOC_f). In order to obtain these values, the use of a periodic continuation of driving cycles is proposed. By means of this approach, the trajectory of the state of charge SOC as well as its initial value SOC_0 and final value SOC_f converge. Figures 6.2(a) - 6.2(c) depict the state of charge SOC over time for different driving cycle profiles and initial values. The driving cycles are repeated fifteen times with defined values of the initial state of charge SOC_0 of 50 %, 70 % and 90 %. All the scenarios have in common that a convergence of the state of charge SOC is obtained after a few periods of the driving cycles despite different initial values. The results show that the trajectories tend to high values of the state of charge SOC in order to exploit higher discharging as well as charging powers of the battery.

As the maximum terminal voltage U_{TERM} of the battery is limited by means of the maximum open-circuit voltage $U_{OC,max}$, the charging power of the battery and implicitly the recuperation potential decrease for very high values of the state of charge SOC. Due to these contrary effects, a convergence of the state of charge trajectory is finally obtained for each vehicle configuration. Based on the results, the initial and final value of the state of charge (SOC_0 and SOC_f) are defined by 85 %. These values are further used to substitute a higher number of periodical scenarios by only one driving cycle, which allows to significantly reduce calculation time.

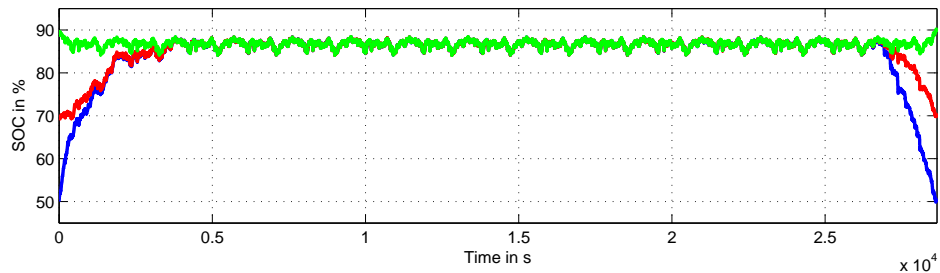
As described in Chapter 4, a general framework for applying the DP algorithm was built. In order to determine the specific parameters of the dynamic program, a number of variations were calculated. Table 6.2 compares the corresponding results in terms of accuracy and calculation time for different driving cycles. To calculate the benchmark for each driving cycle, a very fine discretization of the state variable state of charge ($\Delta SOC = 10^{-5}$) and control variable battery current ($\Delta I_{BAT} = 0.125$ A) was used. It can be seen that the IDP approach (five iterations, initial state of charge discretization $\Delta SOC = 10^{-3}$, battery current discretization $\Delta I_{BAT} = 0.5$ A) represents a good compromise in terms of accuracy and



(a) Trajectories of the state of charge based on the Braunschweig city driving cycle.



(b) Trajectories of the state of charge based on the Manhattan bus cycle.



(c) Trajectories of the state of charge based on the Orange County bus cycle.

Figure 6.2.: State of charge (SOC) trajectories over time for different driving cycles and initial values. In order to obtain a convergence of the SOC, the driving cycle profiles are repeated fifteen times. According to the simulation results, the initial value of the SOC was finally defined by 85 % for all driving cycles.

calculation time. Hence, these parameters are used as reference in order to configure several dynamic programs in the following sections.

Figure 6.3 depicts the results of different iterations of the IDP approach on the basis of the Braunschweig city driving cycle. Every iteration restricts the state space \mathcal{X} by means of a grid reduction factor of 0.5. The remaining state space \mathcal{X} is refined for the next iteration, which improves the accuracy of the solution. Instead of using a very fine discretization, IDP allows to reduce the calculation effort while still providing a high accuracy of the result.

Figure 6.4 shows the split of EGU efficiencies η for different driving cycles by means of a histogram. For this purpose, the ratio of operating points depending on the efficiencies η is depicted for different driving cycles. It can be seen that the optimal operating strategies only switch between idling ($\eta = 0\%$) and high efficiencies ($\eta > 30\%$) and strictly avoid inefficient load points of the EGU.

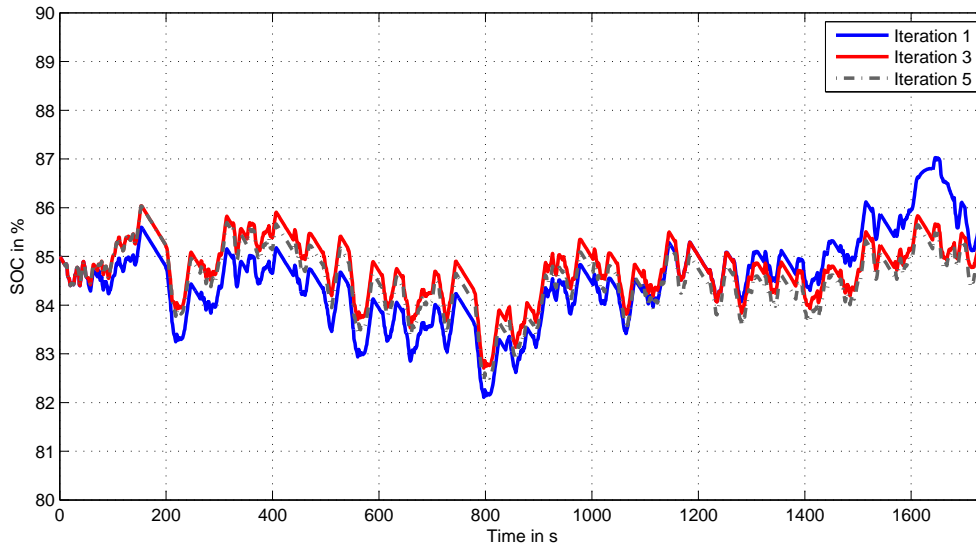


Figure 6.3.: State of charge trajectories of different iterations. The method of IDP is applied to calculate optimal trajectories of the state of charge SOC. For this purpose, a grid reduction factor of 0.5 is used. After each iteration, the restricted state space \mathcal{X} is refined to improve the accuracy of the solution.

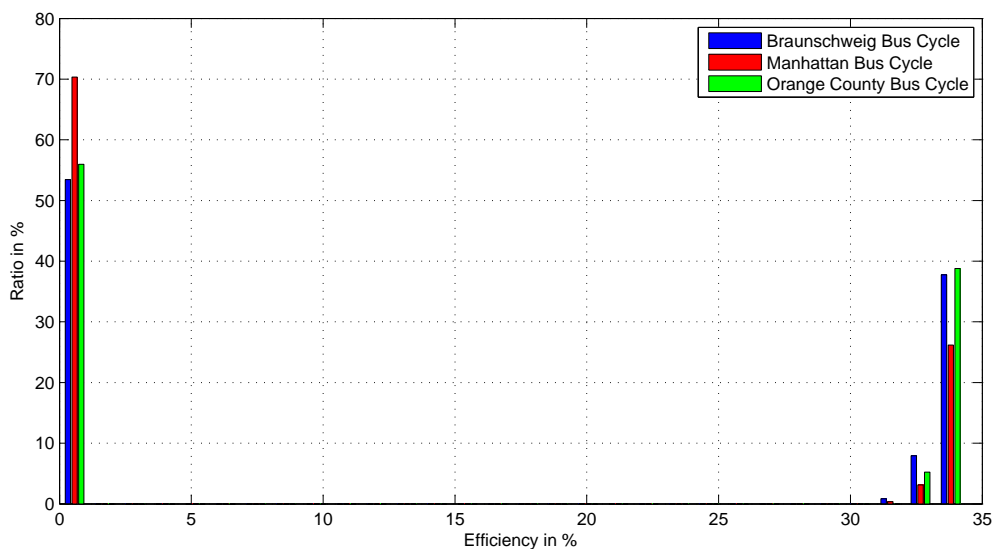


Figure 6.4.: Histogram of EGU efficiencies η . The figure shows the ratio of operating points depending on the efficiencies η for three different driving cycles. The optimal operating strategies only switch between idling ($\eta = 0\%$) and high efficiencies ($\eta > 30\%$) and avoid the use of inefficient load points.

Table 6.2.: Variation of the configuration of a typical dynamic program used in this thesis. The dynamic program contains the battery's state of charge SOC as state variable x as well as the battery current I_{BAT} as control variable u and minimizes the fuel consumption f_c . Characteristic parameters like the accuracy and the calculation time are compared for different discretizations of the state of charge ΔSOC , discretizations of the control variable ΔI_{BAT} and driving cycles. To obtain a reference result, very fine discretizations of the state of charge ΔSOC and battery current ΔI_{BAT} are used. Furthermore, the results of the iterative dynamic programming (IDP) approach containing a grid reduction factor of 0.5 are depicted for the first and last iteration. The comparisons show that the iterative approach (five iterations, initial state of charge discretization $\Delta SOC = 10^{-3}$, battery current discretization $\Delta I_{BAT} = 0.5$ A) provides a meaningful trade-off in terms of accuracy and calculation time.

	state of charge dis- cretization ΔSOC	iteration (total iterations)	battery current dis- cretization ΔI_{BAT}	fuel consumption f_c	calculation time [†]
unit	-	-	A	lit.	s
Braun-	$1.000 \cdot 10^{-3}$	1 (5)	0.500	6.403 (+ 0.14 %)	304
schweig	$6.250 \cdot 10^{-5}$	5 (5)	0.500	6.399 (+ 0.08 %)	1520
bus	$6.250 \cdot 10^{-5}$	1 (1)	0.500	6.398 (+ 0.06 %)	4394
cycle	$3.125 \cdot 10^{-5}$	1 (1)	0.125	6.394 (100.00 %)	32733
Manhattan	$1.000 \cdot 10^{-3}$	1 (5)	0.500	2.431 (+ 0.37 %)	181
bus	$6.250 \cdot 10^{-5}$	5 (5)	0.500	2.425 (+ 0.12 %)	903
cycle	$6.250 \cdot 10^{-5}$	1 (1)	0.500	2.425 (+ 0.12 %)	2752
	$3.125 \cdot 10^{-5}$	1 (1)	0.125	2.422 (100.00 %)	20817
Orange	$1.000 \cdot 10^{-3}$	1 (5)	0.500	6.300 (+ 0.17 %)	335
County	$6.250 \cdot 10^{-5}$	5 (5)	0.500	6.293 (+ 0.06 %)	1677
bus	$6.250 \cdot 10^{-5}$	1 (1)	0.500	6.293 (+ 0.06 %)	4793
cycle	$3.125 \cdot 10^{-5}$	1 (1)	0.125	6.289 (100.00 %)	36039

[†] The calculations were performed on an Intel Core i5-3470 CPU with 3.20 GHz and 8 GB RAM on a 64-bit operating system.

This section outlined the influence of different discretizations of state variables x and control variables u as well as the benefits of IDP by means of a reference simulation model. Furthermore, useful values of the initial and final state of charge (SOC_0 and SOC_f) for periodical driving cycles were defined. Based on the results obtained, a general configuration of a dynamic program was determined which is applied in the following sections in order to calculate optimal operating strategies and component sizes.

6.2. Sizing of Energy Sources

The model of the hybrid electric bus used in this work contains an EGU and a battery as energy sources. In order to fulfill the power demand P_{DEM} of given driving scenarios, these components need to be sized accordingly. Representative parameters of driving cycles such as mean power and maximum power mainly influence the sizes of energy sources. For example, the sum of the battery and EGU powers must cover a desired maximum power of the driving cycle. As described in Section 2.3, the hybridization ratio h_r depicts a further degree of freedom in terms of sizing the energy sources.

In this section, the optimal sizes of energy sources are determined for different vehicle configurations and driving cycles. By means of the DP algorithm, the minimum power of the EGU $P_{EGU,min}$ is calculated for several battery capacities C_{BAT} . Based on the results obtained, optimal design rules for the energy sources can be derived.

6.2.1. Methodology

The minimum power of the EGU $P_{EGU,min}$ is calculated with the help of an iterative approach which consists of two parts: Firstly, the DP algorithm calculates the optimal fuel consumption f_c and guarantees that the vehicle configuration covers the power demands P_{DEM} of the driving cycle. Secondly, the maximum power of the EGU $P_{EGU,max}$ is iteratively adapted according to the previously calculated results. If no feasible solution exists, then the maximum EGU power $P_{EGU,max}$ is increased and vice-versa. The described approach is repeated until the maximum EGU power $P_{EGU,max}$ sufficiently converges.

Since different sizes of battery and EGU affect the overall vehicle mass m , the masses of energy sources need to be scaled. For this purpose, corresponding gravimetric power densities are determined on the basis of the parameters described in Sections 5.4 and 5.6, respectively. These gravimetric power densities are used to linearly scale the masses of the energy sources for different sizes.

The following optimization problem is solved for a given set of battery capacity C_{BAT} and maximum power of the engine-generator unit $P_{EGU,max}$:

$$\begin{aligned}
 & \min_{u_k \in \mathcal{U}_k} \sum_{k=0}^{N-1} \dot{m}_f(u_k, x_k, w_k, C_{BAT}, P_{EGU,max}) \cdot \Delta t \\
 & \text{s.t.} \\
 & x_{k+1} = \frac{u_k \cdot \Delta t}{C_{BAT} \cdot 3600} + x_k \\
 & 0 \leq x_k \leq 1 \\
 & -3 \cdot C_{BAT} \leq u_k \leq 10 \cdot C_{BAT} \\
 & x_0 = 0.85 \\
 & x_f = 0.85 \\
 & x_k \in \mathcal{X}_k \\
 & u_k \in \mathcal{U}_k
 \end{aligned}$$

where the battery current I_{BAT} is used as control variable u_k , the battery's state of charge SOC as state variable x_k and the power demand P_{DEM} as disturbance w_k . In addition, limits of the control and state variables as well as a sampling time Δt of 1 s are considered. By means

of the defined optimization problem, the minimum size of the EGU is determined for a given battery capacity C_{BAT} .

6.2.2. Results

Before focusing on optimal combinations of energy sources, two extreme limits can be considered:

- If the battery capacity C_{BAT} is very small, then the EGU has to fulfill the maximum power demand $P_{DEM,max}$ of the driving cycle,
- If the battery capacity C_{BAT} is very high, then the EGU only needs to provide the mean power demand \bar{P}_{DEM} of the driving cycle.

In order to determine these limits, only the power of the driving cycle P_{DEM} is taken into account. Thus, the results obtained provide a rough estimate in terms of sizing the energy sources and can be used for plausibility checks. To improve the accuracy for the sizing of energy sources, the efficiencies η of all vehicle components need to be included into the optimization problem. The previously described methodology fulfills this requirement and calculates the minimum power of the EGU $P_{EGU,min}$ for a given battery capacity C_{BAT} .

Figure 6.5 shows the minimum power of the EGU $P_{EGU,min}$ depending on the battery capacity C_{BAT} for different driving cycles. The results represent a set of optimal solutions which can also be denoted as Pareto front [102, 68]. Additionally, the figure shows that the EGU power P_{EGU} converges for higher battery capacities C_{BAT} . This trend can be justified by means of the limited recuperation potential of the driving cycles. If initial component costs of the EGU as well as the battery ($c_{comp,egu}$ and $c_{comp,bat}$) are known, then the cost-optimal configuration of the set of optimal solutions can be determined.

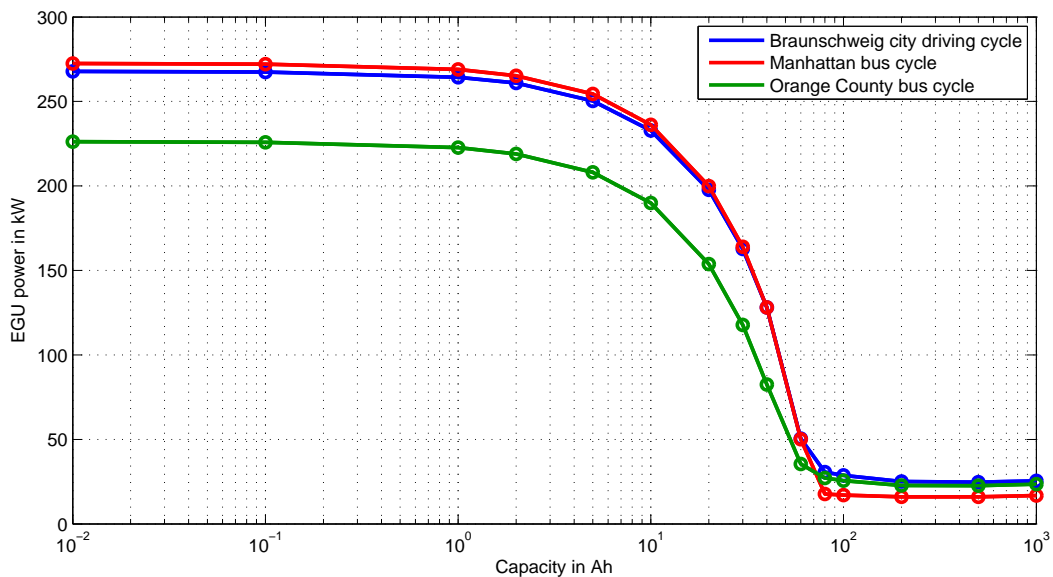


Figure 6.5.: Minimum EGU power $P_{EGU,min}$ depending on the battery capacity C_{BAT} for three driving cycles. The figure depicts possible combinations of battery capacity C_{BAT} and EGU power P_{EGU} which fulfill the power demands P_{DEM} of the driving cycles.

Figure 6.6 shows the corresponding fuel consumption f_c of the previously determined combinations of energy sources. The figure shows that the fuel consumption f_c decreases until a battery capacity C_{BAT} of approximately 100 Ah. For higher battery capacities C_{BAT} , the fuel consumption f_c slightly increases due to influences of higher battery masses m_{bat} together with the limited recuperation potential. The results shown in Figures 6.5 and 6.6 allow to define further optimization problems that include for example combinations of initial component costs ($c_{comp,egu}$ and $c_{comp,bat}$) and fuel consumption f_c .

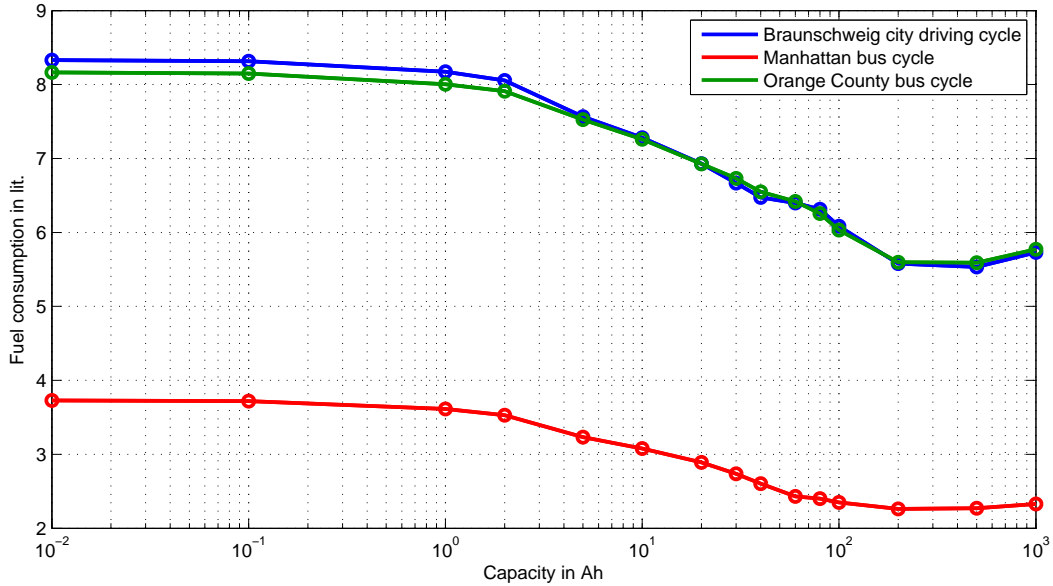


Figure 6.6.: Minimum fuel consumption f_c depending on the battery capacity C_{BAT} for different driving cycles. For each battery capacity C_{BAT} , the minimum power of the EGU $P_{EGU,min}$ is used to calculate the corresponding fuel consumption f_c .

In this section, optimal configurations of the energy sources EGU and battery were calculated. The results obtained provide a set of optimal solutions which can also be denoted as Pareto front. Furthermore, the minimum fuel consumption f_c was calculated for all optimal configurations. Based on the results, it is possible to determine the optimal combination of energy sources, which minimizes parts of the life cycle costs c_{life} .

6.3. Sizing of Electric Motors

This section presents a novel approach for the optimal sizing of electric motors (EMs) in hybrid electric vehicles (HEVs). EMs are usually scaled with the help of standardized duty cycles in order to fulfill desired requirements of power, torque and speed. For example, the international standard IEC 60034-1 [41] defines ten operating modes containing eight periodical (S1 - S8) and two aperiodical (S9 - S10) duty cycles. This work focuses on two commonly used duty cycles and sizes the EMs on the basis of the S1 and S2 modes. According to [41], these modes are defined as follows:

”Duty type S1 – Continuous running duty:

Operation at a constant load maintained for sufficient time to allow the machine to reach thermal equilibrium.”

”Duty type S2 – Short-time duty:

Operation at constant load for a given time, less than that required to reach thermal equilibrium, followed by a time de-energized and at rest of sufficient duration to re-establish machine temperatures within 2K of the coolant temperature.”

In general, the sizing of EMs in terms of the S1 and S2 modes is carried out with the help of defined limits like continuous power, continuous torque, maximum power over a certain time span or maximum torque over a certain time span. However, the scaling of EMs in HEVs depicts a more complex task as parameters like the hybridization ratio h_r , the driving cycle or the operating strategy need to be considered.

In related work [19, 58, 76, 101, 109], the EM is modeled by means of a maximum torque curve over speed. The limits of this maximum torque curve are usually determined with the speed and torque demands due to driving cycles. Furthermore, the work of [79] restricts the maximum torque curve over speed on the basis of the maximum and minimum battery current I_{BAT} . All of these approaches do not distinguish between the S1 and S2 modes and assume that thermal limits of the EM are not exceeded.

In contrast, the methodology of this work considers thermal effects and calculates optimal specifications in terms of the S1 and the S2 modes for EMs in HEVs.

6.3.1. Methodology

Firstly, the same reference configuration of the hybrid electric bus is used as shown in Section 6.1. In order to demonstrate the approach proposed in this section, the electric traction motors are optimized in terms of the S1 and S2 modes. As the approach needs a scalable EM model, the model of Section 5.3 is expanded by considering the effects caused due to overloading and voltage dependencies. Figure 6.7 depicts the original efficiency map defined for the S1 mode of the EM. In order to obtain the efficiencies η in case of the S2 mode as well as overloading, a quadratic extrapolation of the power loss $P_{LOSS,EM}$ is carried out for several speeds n as shown for example in [23].

The EM provides in case of overloading a higher torque M than in the continuous S1 mode. In literature [81, 20, 21, 98, 96] several approaches are taken into account to consider the ratio between maximum S2 torque M_{max} and continuous S1 torque M_{cont} . These approaches strongly differ among the manufacturers, EM types as well as the corresponding power electronics. In

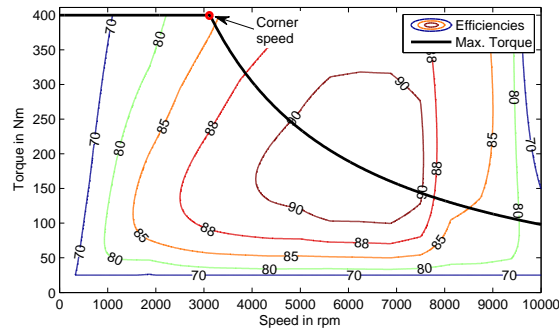


Figure 6.7.: Efficiency map of the scaled EM based on the continuous S1 mode. In order to obtain the efficiencies η in case of overloading as well as the S2 mode, an extrapolation of the power loss $P_{LOSS,EM}$ is carried out by means of a quadratic approach.

order to describe overloading effects, this work takes into account the characteristic equivalent circuit model of an EM as shown in Figure 6.8. The equivalent circuit model is given by means of the resistance R_{EM} , the inductance L_{EM} and the voltage due to the counter-electromotive force U_{EMF} which is proportional to the speed n . As the EM current I_{EM} is proportional to the torque M , the overloaded EM leads to higher voltage drops ΔU at the resistance R_{EM} . Therefore, lower voltages U_{EMF} and corner speeds n_{cor} are obtained in case of an overloaded EM.

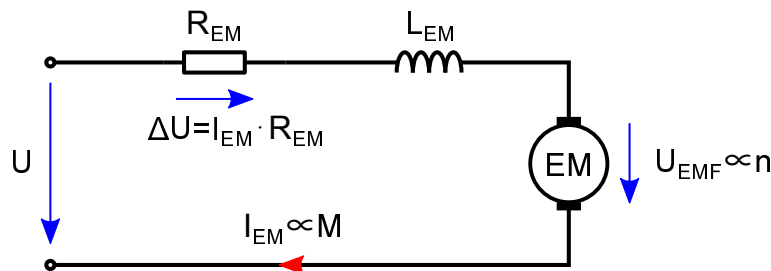


Figure 6.8.: Equivalent circuit of an EM. The EM is modeled by means of a resistance R_{EM} , an inductance L_{EM} and a voltage due to the counter-electromotive force U_{EMF} which is proportional to the speed n . Furthermore, U denotes the voltage of the high-voltage vehicle's electrical system and I_{EM} the current of the EM which is proportional to the torque M . In case of overloading, lower voltages U_{EMF} and corner speeds n_{cor} are obtained as the current I_{EM} causes higher voltage drops ΔU .

If the EM is operated on its maximum S2 torque M_{max} , the corresponding corner speed $n_{cor,max}$ decreases compared to the corner speed $n_{cor,cont}$ of the S1 mode. In order to determine the corner speed in case of overloading, the efficiency η at the continuous corner speed $n_{cor,cont}$ and continuous S1 torque M_{cont} is taken into account. As shown in Figure 6.7, the corresponding efficiency η at this load point is 86%. Furthermore, it is assumed that the overall power loss $P_{LOSS,EM}$ (14%) can be divided into electrical and mechanical losses which are

estimated by 10% and 4%, respectively. By means of this approximation, the ratio of the voltage drop ΔU to the voltage U is determined by 10%.

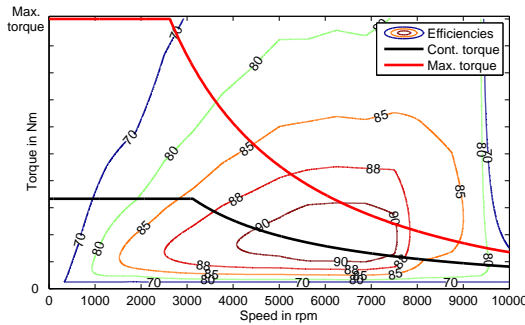
For example, it is assumed that the EM can be overloaded by means of a factor c_{ov} of three below the corner speed n_{cor} for short time spans. In that case, the EM current I_{EM} also increases by this factor which causes an additional voltage drop of $2 \cdot \frac{\Delta U}{U} = 20\%$. Thus, the voltage U_{EMF} and the corner speed $n_{cor,max}$ decrease by 20% in this example. In order to describe the behavior for speeds n that exceed the corner speed n_{cor} , an affine reduction of the maximum S2 torque M_{max} is applied based on data sheets of [21, 96].

As stated in Section 5.3, the maximum speed n_{max} as well as the continuous corner speed $n_{cor,cont}$ of the EM are defined by 10000 rpm and 3120 rpm, respectively. In order to include the voltage dependencies of the high-voltage vehicle's electrical system into the EM model, a linear approach is taken into account. For this purpose, the corner speed n_{cor} as well as the maximum power $P_{EM,max}$ are linearly scaled on the basis of a nominal voltage U_{NOM} of 360 V. Table 6.3 shows the corresponding values of the previously described parameters.

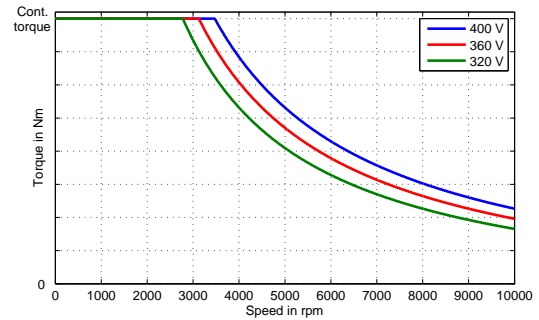
Table 6.3.: List of characteristics of the EM.

maximum speed n_{max}	10 ⁴	rpm
continuous corner speed $n_{cor,cont}$	3120	rpm
nominal voltage U_{NOM}	360	V

Figure 6.9(a) depicts the overall efficiency map of the EM containing the continuous S1 mode as well as the S2 mode in case of an assumed overloading factor c_{ov} of 3. Furthermore, Figure 6.9(b) shows the continuous S1 torque curves over speed of the EM for different voltage levels of the high-voltage vehicle's electrical system.



(a) Efficiency map of the overloaded EM.



(b) Voltage dependencies of the EM.

Figure 6.9.: Overloading effects as well as voltage dependencies of the EM. The left figure depicts the efficiency map of the continuous S1 mode as well as the S2 mode in case of an overload factor c_{ov} of 3. The right figure shows the continuous torque M_{cont} over speed for different voltage levels of the high-voltage vehicle's electrical system.

In a further step, an acceleration scenario of the bus is simulated in order to demonstrate the effects due to different voltage levels of the high-voltage vehicle's electrical system. For simplicity, it is assumed that both electrical traction machines provide a maximum torque M_{max} of 600 Nm and the energy sources fulfill the corresponding power demands. Figure 6.10

shows that the time span for reaching the maximum velocity v_{max} significantly depends on the voltage level of the high-voltage vehicle's electrical system. As these effects may also influence the sizing of EMs on the basis of driving cycles, the methodology of this section uses voltage-dependent EM models.

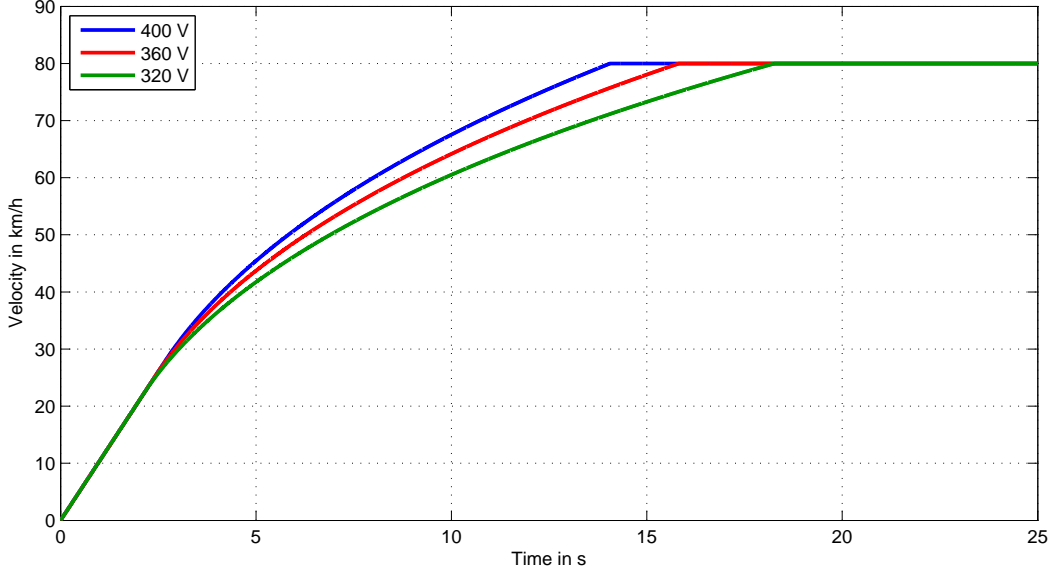


Figure 6.10.: Acceleration scenario of the bus for different voltage levels of the high-voltage vehicle's electrical system. The two electrical traction machines are sized to provide a maximum torque M_{max} of 600 Nm. It can be seen that the time span for reaching the maximum velocity v_{max} significantly depends on the voltage level of the high-voltage vehicle's electrical system.

After describing the scalable EM model used in this section, further characteristics are necessary to determine the requirements for the S1 mode. As this operating mode represents the continuous mode of the EM, the thermal behavior of the EM needs to be considered appropriately. For this purpose, a simplified thermal model is introduced depicted in Figure 6.11. The model consists of two point masses and distinguishes between the windings and the remaining parts of the EM. The inputs of the model are given by means of the power loss $P_{LOSS,EM}$ of corresponding load points and the cooling power P_{COOL} . Furthermore, a thermal resistance R_{TH} is used to consider heat flows between the two point masses. The model outputs are defined by means of the winding temperature ϑ_w and the temperature of remaining parts ϑ_r . The following two equations describe the thermal behavior of the EM:

$$\vartheta_w(t) = \frac{1}{c_{p,w} \cdot m_w} \cdot \int \left(P_{W,EM}(t) - \frac{\vartheta_w(t) - \vartheta_r(t)}{R_{TH}} \right) dt + \vartheta_{w,0}, \quad (6.1)$$

$$\vartheta_r(t) = \frac{1}{c_{p,r} \cdot m_r} \cdot \int \left(P_{R,EM}(t) - \frac{\vartheta_r(t) - \vartheta_w(t)}{R_{TH}} - P_{COOL}(t) \right) dt + \vartheta_{r,0}. \quad (6.2)$$

Table 6.4 lists the values of all thermal parameters of the EM model. As the corner speed n_{cor} of the EM is defined as a constant, the continuous S1 torque M_{cont} scales the continuous power P_{cont} of the EM. By means of the constant power-to-weight ratio PWR, the continuous power P_{cont} can be converted into an equivalent mass containing the masses of the

windings m_w and remaining parts m_r . Furthermore, the power loss P_{LOSS} is divided into two parts to describe the losses caused in the windings and remaining parts. As the EM model uses a total power loss map to determine the power loss P_{LOSS} of corresponding load points, the distribution between the power loss in the windings $P_{W,EM}$ and the remaining parts $P_{R,EM}$ need to be approximated. Since the load points of driving cycles usually cover a broad range of torque and speed requirements, a constant ratio is taken into account for simplicity.

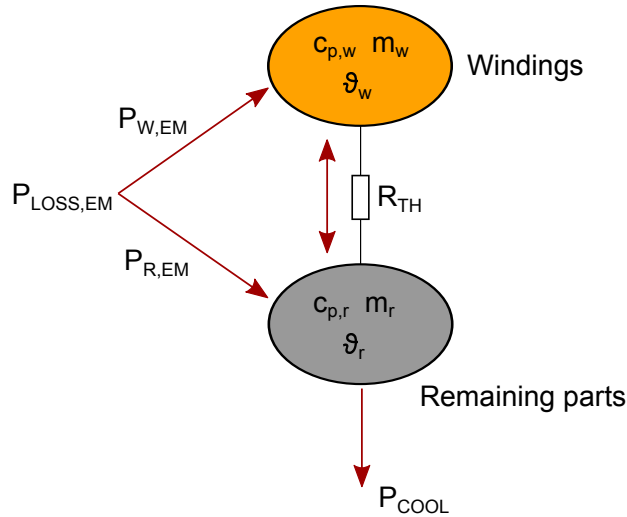


Figure 6.11.: Thermal model of the EM. The model consists of two point masses (m_w , m_r) with corresponding thermal capacities ($c_{p,w}$, $c_{p,r}$) to distinguish between the windings and the remaining parts of the EM. The inputs of the model are given by means of the power loss $P_{LOSS,EM}$ due to the load points as well as the cooling power P_{COOL} . Furthermore, a thermal resistance R_{TH} is used to describe the heat flow between the two point masses. The model outputs are defined by means of the temperatures ϑ_w and ϑ_r .

In order to determine the cooling power P_{COOL} of the EM, the power loss $P_{LOSS,EM}$ along the S1 torque curve are calculated in the first step. Furthermore, it is assumed that the EM can provide a constant continuous cooling power P_{COOL} which does not depend on the speed n of the EM. The value of the continuous cooling power P_{COOL} is approximated by means of the maximum continuous power loss $P_{LOSS,EM,max}$ below the corner speed $n_{cor,cont}$. Figure 6.12 depicts the corresponding approach to determine the continuous cooling power P_{COOL} for a given EM model. After the description of the scalable EM model, the methodology for the optimal sizing of EMs based on the S1 and S2 modes is summarized in the following:

The goal of the methodology is to iteratively determine the continuous S1 torque M_{cont} and the maximum S2 torque M_{max} of the EM for given driving cycles. In addition, the voltage dependencies as well as the thermal limits are integrated into the optimization. The DP algorithm is applied to calculate the optimal operating strategy for an initial maximum S2 torque $M_{max,0}$ of the EM. If no feasible solution is obtained, then the maximum S2 torque M_{max} is increased and vice-versa.

Table 6.4.: Thermal parameters of the EM.

power-to-weight ratio PWR	1.8 [†]	kW/kg
specific heat capacity windings $c_{p,w}$	385	J/(kg · K)
specific heat capacity remaining parts $c_{p,r}$	449	J/(kg · K)
initial temperature ϑ_{init}	40	°C
maximum temperature ϑ_{max}	160	°C
ratio of $m_w/(m_w + m_r)$	0.15	-
ratio of $m_r/(m_w + m_r)$	0.85	-
ratio of $P_{W,EM}/(P_{W,EM} + P_{R,EM})$	0.67	-
ratio of $P_{R,EM}/(P_{W,EM} + P_{R,EM})$	0.33	-
thermal resistance R_{TH}	0.01	K/W

[†] Mean value based on data sheets [13] of the EMs 10.18.13, 10.18.22 and 12.18.13.

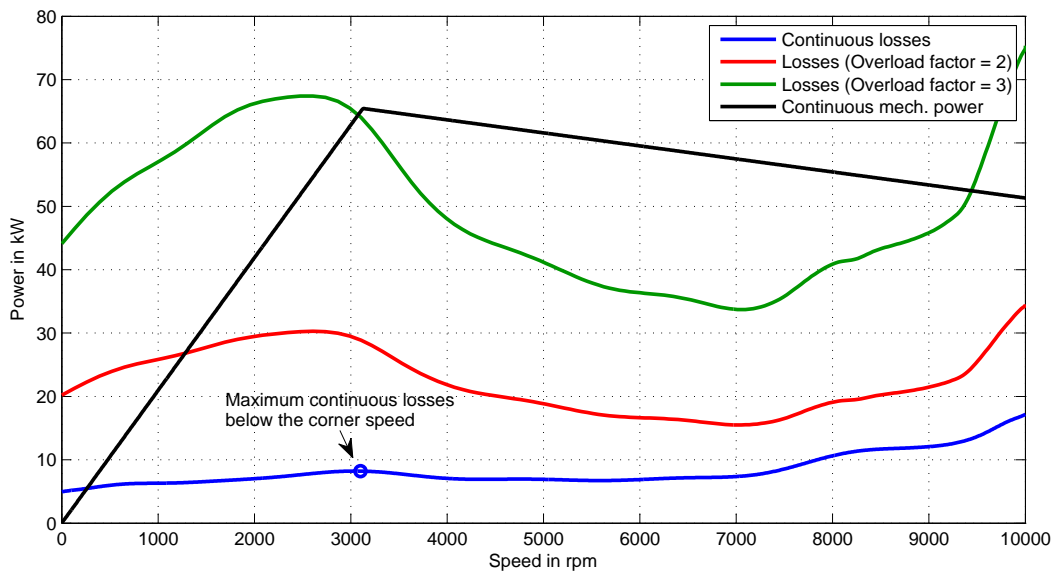


Figure 6.12.: Power loss $P_{LOSS,EM}$ of the EM. The power loss as well as the continuous mechanical power P_{MECH} are depicted over the speed n . In order to determine the continuous cooling power P_{COOL} of the EM the maximum loss $P_{LOSS,EM,max}$ below the corner speed $n_{cor,cont}$ is used. The power loss in case of overloading is determined by a quadratic extrapolation of the continuous power loss map.

To summarize, the following optimization problem is solved for a given maximum S2torque M_{max} :

$$\begin{aligned}
& \min_{u_k \in \mathcal{U}_k} \sum_{k=0}^{N-1} \dot{m}_f(u_k, x_k, w_k, M_{max}) \cdot \Delta t \\
& \text{s.t.} \\
& x_{k+1} = \frac{u_k \cdot \Delta t}{C_{BAT} \cdot 3600} + x_k \\
& 0 \leq x_k \leq 1 \\
& -120 \leq u_k \leq 400 \\
& x_0 = 0.85 \\
& x_f = 0.85 \\
& x_k \in \mathcal{X}_k \\
& u_k \in \mathcal{U}_k
\end{aligned}$$

where the battery current I_{BAT} is used as control variable u_k , the battery's state of charge SOC as state variable x_k and the power demand P_{DEM} as disturbance w_k . In addition, limits of the control and state variables as well as a sampling time Δt of 1 s are considered.

After sizing the EM on the basis of the S2 mode, the requirements for the continuous S1 mode are calculated in the next step. For this purpose, the thermal behavior of the EM needs to be considered in more detail. The proposed approach takes into account the continuous cooling power P_{COOL} of the EM which must be higher than the mean power loss $\bar{P}_{LOSS,EM}$ due to given load points. Furthermore, this part of the methodology considers thermal limits like the maximum winding temperature $\vartheta_{w,max}$. If thermal limits are exceeded, the continuous S1 torque is increased until a sufficient convergence is obtained.

In order to increase the degrees of freedom in terms of the sizing of electric traction motors, a two-speed gear is integrated into the drivetrain. By means of this expansion, the sizing of the EM not only depends on the driving cycle but also on the ratio of the second gear.

6.3.2. Results based on a Battery

The previously described methodology is applied for the optimal sizing of electric traction motors in HEVs.

Firstly, the optimal maximum S2 torque M_{max} is determined for the driving cycles of Appendix D (Braunschweig city driving cycle, Manhattan bus cycle and Orange County bus cycle). The consideration of voltage swings of the battery's terminal voltage U_{TERM} depicts another degree of freedom in the formulation of the optimization problem. Table 6.5 depicts the results, which are based on the reference configuration of the hybrid bus as shown in Section 6.1. It can be seen that the considered voltage swings of the battery's terminal voltage U_{TERM} do not affect the results. In that case, one can conclude that the sizing of the EM in terms of the S2 mode significantly depends on the load points of the driving cycle.

The next part of the methodology considers the optimal sizing of the EMs in terms of the S1 mode. The optimal continuous S1 torque is iteratively increased until no thermal limits of the EM are exceeded. For example, Figure 6.13 shows the temperatures of the windings as well as the remaining parts of the EM for the Braunschweig city driving cycle. As the

Table 6.5.: Comparison of the maximum S2 torque M_{max} for different driving cycles, voltage dependencies and a battery as energy storage. The results show that the voltage swings of the battery's terminal voltage U_{TERM} do not affect the sizing of the EM. Furthermore, the RMS current as well as the mean power loss are depicted.

		neglected voltage dependencies	considered voltage dependencies
Braunschweig city driving cycle		578.7 Nm	578.7 Nm
Manhattan bus cycle		462.9 Nm	462.9 Nm
Orange County bus cycle		386.7 Nm	386.7 Nm

	internal resistance of the battery	RMS current in the battery	mean power loss in the battery
Braunschweig city driving cycle	134.4 m Ω	82.8 A	921 W
Manhattan bus cycle	134.4 m Ω	71.6 A	689 W
Orange County bus cycle	134.4 m Ω	80.9 A	880 W

temperatures are lower than the limit of 160 °C, the size of the EM with corresponding cooling power P_{COOL} is defined accordingly in this example.

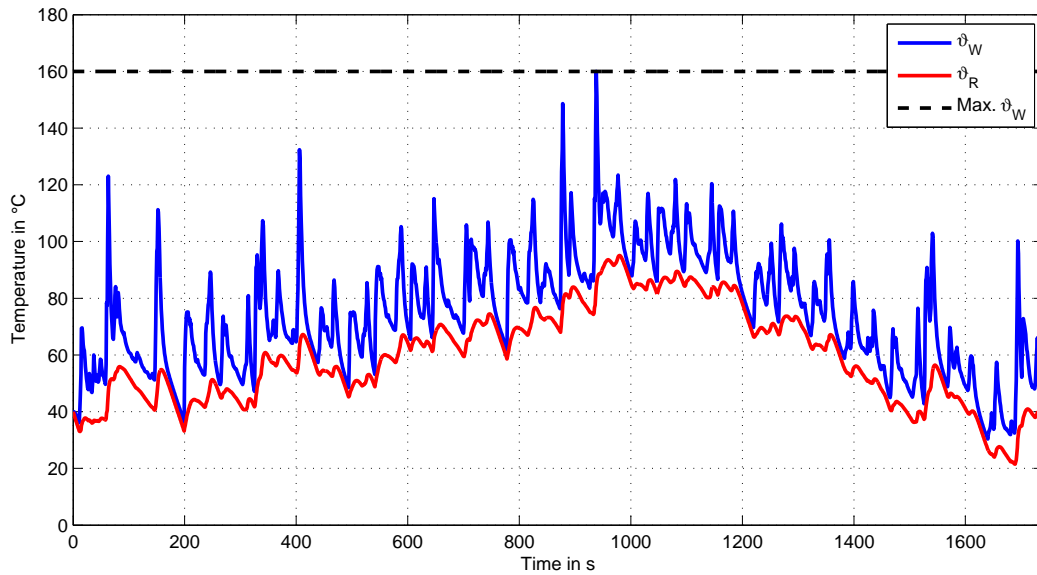


Figure 6.13.: Temperatures of the windings as well as the remaining parts of the EM for the Braunschweig city driving cycle. As the temperatures are lower than the limit of 160 °C, the EM is appropriately sized in terms of the continuous S1 mode.

In the next step, the drivetrain is expanded by means of a two-speed gear box. In order to determine the second gear ratio, the ratio of the first gear derived in Section 5.2 is multiplied by means of a factor. In this section, the range of this factor is limited by 1 and 3, respectively. Due to the additional gear, the operating strategy contains another degree of freedom which can be exploited to reduce the maximum S2 torque M_{max} as well as the continuous S1 torque M_{cont} . Figure 6.14 depicts both torques M_{max} and M_{cont} of the electric traction motors over

the normalized ratio of the second gear. The results show that the integration of a second gear leads to reductions especially for the maximum S2 torque M_{max} . On the basis of different driving cycles, it can be concluded that the ratio of the first to the second gear should be within a range of 1.2 and 1.4.

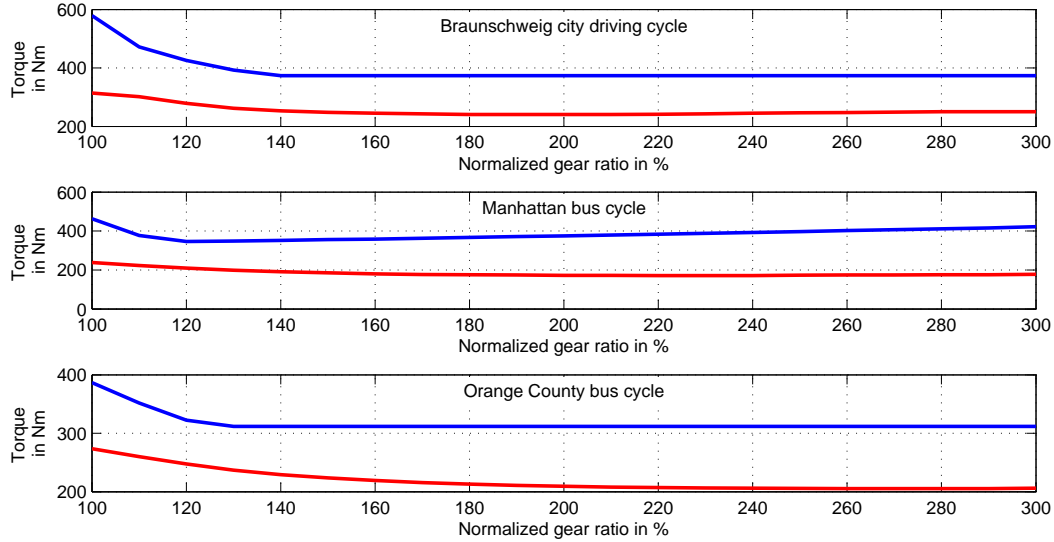


Figure 6.14.: Optimal sizes of the electrical traction machines depending on the normalized ratio of the second gear. The blue lines depict the maximum S2 torque M_{max} and the red lines show the continuous S1 torque M_{cont} .

Furthermore, the DP algorithm provides the corresponding fuel consumption f_c due to different driving cycles and electric traction motors. Figure 6.15 depicts the fuel consumption f_c over the second gear ratio. Beside the reduction of the maximum S2 torque M_{max} and the continuous S1 torque M_{cont} , the integration of a second gear also leads to a lower fuel consumption f_c .

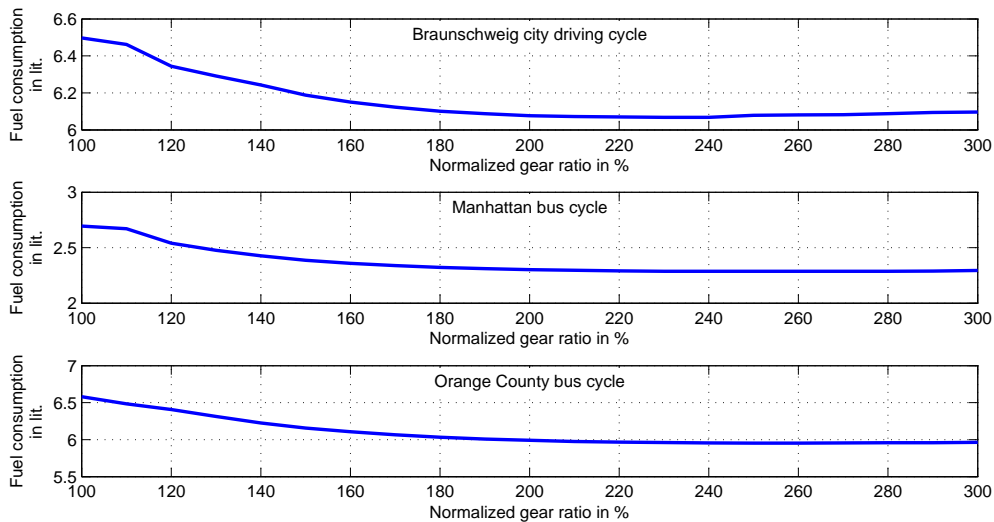


Figure 6.15.: Fuel consumption f_c depending on the second gear. It can be seen that the integration of a second gear leads to a lower fuel consumption f_c .

As the results of Figures 6.14 and 6.15 depict Pareto fronts in terms of optimal EMs and fuel consumption f_c , the optimal ratio of the second gear can be determined. For this purpose, the initial costs $c_{comp,em}$ of the EM, the fuel consumption f_c or a combination of both can be taken into account to calculate the cost-optimal configuration.

In this subsection, the electrical energy storage was defined by means of a battery. Since the sizing of EMs was not affected by the voltage swings of the battery's terminal voltage U_{TERM} , the influence of another type of electrical energy storage is evaluated in the following.

6.3.3. Results based on a Supercap

So far the sizing process of the EM was presented for an almost fixed battery voltage U_{TERM} . In order to demonstrate a scenario containing larger voltage swings, the battery is replaced by means of a supercap. For this purpose, two different supercap types are considered in this work:

Firstly, the influence of a high supercap capacitance C_{SC} is evaluated. As a high supercap capacitance C_{SC} leads to small voltage swings, the maximum torque M_{max} of the EM should not depend on the voltage and furthermore, smaller sizes of the EMs will result.

Secondly, the vehicle configuration contains a small supercap capacitance C_{SC} . For this purpose, the supercap capacitance C_{SC} is optimized for given driving cycles. An optimized supercap should be discharged during a cycle to around 50% of the maximum voltage U_{max} . Hence, 75% of the maximum supercap energy E_{SC} will be used during the cycle and recovered by the generator. As the voltage swings increase in case of a small supercap the sizing of the EM is significantly affected.

The two chosen supercap types described before provide limits in terms of sizing the power source and traction machines. In order to determine the optimal combination, further parameters like component costs and gear box ratio can be taken into account.

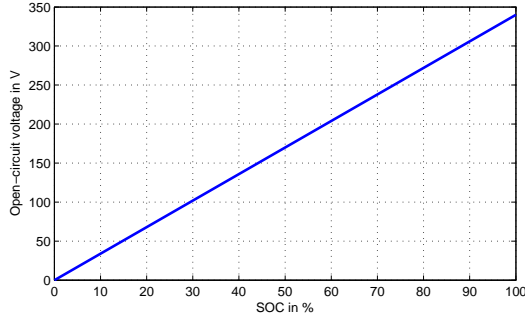
The supercap model is based on the type "EMHSP-0051C0-340R0" [22]. As the maximum voltage U_{max} of the supercap (340 V) and the vehicle's electrical system (360 V) are approximately the same, no DC/DC converter will be used to shift the power supply voltage to the optimum motor inverter voltage. Table 6.6 depicts the parameters of the supercap applied in this subsection.

Table 6.6.: Parameters of the supercap "EMHSP-0051C0-340R0"[22]. This type of supercap has an energy density of 2.13 Wh/kg which is significantly lower than the energy density of batteries. For example, an energy density of 128 Wh/kg can be determined for the fully charged battery pack of Section 5.4.

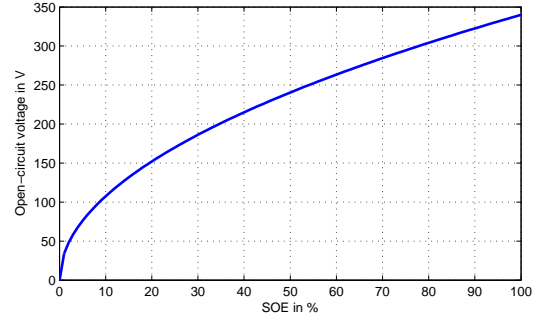
constant parameters	symbol	value	unit
maximum discharge current	I_{DIS}	700 [†]	A
maximum charge current	I_{CH}	700 [†]	A
maximum voltage	U_{max}	340	V
internal resistance	R_{SC}	24.5	mΩ
capacitance	C	51	F
supercap mass	m_{sc}	384	kg

[†] Assumed value.

Furthermore, Figure 6.16(a) depicts the linear relation between the open-circuit voltage U_{OC} and the state of charge SOC. The term state of energy SOE is usually referred to as the state of charge SOC for energy storages like flywheels and supercaps. Figures 6.16(a) and 6.16(b) depict the difference between the open-circuit voltage U_{OC} depending on the SOC as well as the SOE.



(a) Open-circuit voltage U_{OC} of the supercap depending on the state of charge SOC.



(b) Open-circuit voltage U_{OC} of the supercap depending on the state of energy SOE.

Figure 6.16.: Open-circuit voltage U_{OC} of the supercap depending on the SOC and the SOE.

In order to determine the maximum S2 torque M_{max} of the electric traction motors, the same methodology is applied as described in Section 6.3.1. Table 6.7 depicts the corresponding results for different driving cycles and voltage dependencies due to the terminal voltage U_{TERM} of the supercap.

Table 6.7.: Comparison of the maximum torque M_{max} for different driving cycles, voltage dependencies and a supercap as energy storage. The results show that the sizing process does only slightly depend on the terminal voltage swings of the supercap as the state of charge SOC of the supercap varies just as much as up to 11%. Furthermore, the root mean square (RMS) current $I_{RMS,SC}$ as well as the mean power loss $P_{LOSS,SC}$ are depicted.

	neglected voltage [†] dependencies	considered voltage dependencies	state of charge range
Braunschweig city driving cycle	510.9 Nm	510.9 Nm	89 % - 100 %
Manhattan bus cycle	414.9 Nm	414.9 Nm	93 % - 100 %
Orange County bus cycle	386.7 Nm	399.6 Nm	90 % - 100 %
	internal resis- tance of the SC	RMS current in the SC	mean power loss in the SC
Braunschweig city driving cycle	24.5 mΩ	187.2 A	859 W
Manhattan bus cycle	24.5 mΩ	148.4 A	540 W
Orange County bus cycle	24.5 mΩ	182.5 A	816 W

[†] The maximum torque curve of the EM does not depend on the motor inverter voltage.

The results show that the sizing of the EMs slightly depends on the terminal voltage U_{TERM} in case of the Orange County driving cycle. This relatively small difference comes from the maximum speed of the Orange County driving cycle which is higher than the maximum speeds

of the other two driving cycles. In contrast to the results of Table 6.5 lower values of the maximum torque M_{max} are obtained for neglected voltage dependencies. These discrepancies can be justified by means of operating the electrical energy storages at different operating points. As the sizing of the EMs does only slightly depend on the terminal voltage of the supercap, it can be concluded that the capacitance of the supercap ("*EMHSP-0051C0-340R0*") is too high and thus too heavy and costly for the requirements of the driving cycles. Although configurations containing a big supercap capacitance lead to minimum sizes of the EM, the overall vehicle provokes higher initial costs due to the "oversized" supercap. Another drawback is given by the low energy density of supercaps which causes additional vehicle mass as well as higher operating costs. In order to find an improved vehicle configuration, the capacitance of the supercap C_{SC} is optimized in the next step. For this purpose, a scalable supercap model based on the parameters of Table 6.6 is used. Again, the optimization algorithm calculates the maximum torque of the traction machines M_{max} for neglected and considered voltage dependencies. As a further restriction operating points of the inverter leading to a low efficiency η should be avoided. For this purpose, the minimum state of charge SOC of the supercap is defined by 50 % which is equivalent to a state of energy SOE of 25 %. Table 6.8 depicts the minimum capacitance of the supercap C_{min} and the maximum torque M_{max} of the traction machines for different driving cycles.

Table 6.8.: Comparison of the minimum capacitance $C_{SC,min}$ as well as corresponding parameters, RMS current $I_{RMS,SC}$, mean power loss $P_{LOSS,SC}$, maximum torque M_{max} , voltage dependencies and different driving cycles in case of a supercap as energy storage. The results show that the sizing process of the traction machines significantly depends on the terminal voltage swings of the optimized supercaps. Furthermore, the RMS current $I_{RMS,SC}$ as well as the mean power loss $P_{LOSS,SC}$ are depicted. In contrast to the results of Table 6.7 a lower RMS current $I_{RMS,SC}$ and a higher power loss $P_{LOSS,SC}$ are obtained. This behavior is described in the text below.

		neglected voltage dependencies	considered voltage dependencies
Braunschweig city driving cycle		503.9 Nm	892.9 Nm
Manhattan bus cycle		410.2 Nm	668.4 Nm
Orange County bus cycle		382.1 Nm	708.5 Nm
	minimum capacitance	supercap (SC) mass	state of charge range
Braunschweig city driving cycle	12.0 F	90.4 kg	50 % - 100 %
Manhattan bus cycle	9.5 F	71.5 kg	50 % - 100 %
Orange County bus cycle	8.5 F	64.0 kg	50 % - 100 %
	internal resistance of the SC	RMS current in the SC	mean power loss in the SC
Braunschweig city driving cycle	104.1 m Ω	136.3 A	1934 W
Manhattan bus cycle	131.5 m Ω	115.8 A	1763 W
Orange County bus cycle	147.0 m Ω	134.2 A	2647 W

In addition, Table 6.8 evaluates neglected and considered effects due to the terminal voltage

of the supercap. The simulation results show that the maximum torque M_{max} significantly depends on the terminal voltage of the supercap. In contrast to the results of Table 6.7 a lower RMS current $I_{RMS,SC}$ and a higher power loss $P_{LOSS,SC}$ are obtained. This behavior is described in the following:

As the EMs and supercaps are optimized in this section the same reference vehicle configuration of Chapter 5 is used for the remaining components. In order to determine the two component limits minimum capacitance $C_{SC,min}$ and maximum torque M_{max} the DP algorithm is applied for corresponding vehicle configurations. In addition, the DP algorithm provides the optimal operating strategy which significantly depends on the supercap capacitance C_{SC} . The DP algorithm decides to preferably use the engine-generator unit in case of a low capacitance C_{SC} to keep the motor inverter voltage on a higher level as well as to avoid a state of charge SOC below the minimum limit of 50%. Thus, a reduced RMS current $I_{RMS,SC}$ is obtained for a minimum supercap capacitance $C_{SC,min}$ compared to a high supercap capacitance C_{SC} . In addition, the internal supercap resistance R_{SC} increases for a low supercap capacitance C_{SC} which causes a higher power loss $P_{LOSS,SC}$.

As the sizing of EMs is affected due to the voltage swings of the supercap it can be concluded that voltage-dependent effects of the power source need to be considered for the optimal sizing of EMs on the basis of driving cycles.

To summarize, Tables 6.7 and 6.8 provide limits for the sizing of EMs and supercaps. The results show that a high value of the supercap capacitance C_{SC} leads to low values of the maximum torque M_{max} of the EM and vice-versa. As another degree of freedom the gear ratio of the three-speed gear box i_g can be optimized for different driving cycles. This approach allows to handle higher voltage swings of the supercap and consequently leads to lower values of the minimum capacitance of the supercap C_{SC} and to smaller EMs. In order to determine the optimal sizes of supercap and EMs, further parameters can be considered which are for example component costs. In addition, effects like calendric or cyclic aging of supercaps can be included into the optimization.

In this section, two approaches for the optimal sizing of EMs were presented which either consider or neglect the voltage of the vehicle's electrical system. Whereas voltage-dependent effects can be neglected for a battery, these effects significantly influence the optimization in case of supercaps. Beside the sizing of traction machines, the approaches can also be used to determine optimal combinations of EMs and energy storages.

6.4. Cost-optimal Operating Strategies

In the Sections 6.1-6.3, the optimization goal was to minimize the fuel consumption f_c . However, in applications such as public transport or freight traffic, the optimization of costs is more important than only minimizing the fuel consumption f_c .

This section focuses on minimizing the operating costs of HEVs and expands the previously applied fuel-optimal approaches. For this purpose, costs which are influenced through the operating strategy are considered in the optimization problem. In addition to the fuel costs due to the fuel consumption f_c , the operating strategy also provokes component wear. In order to obtain costs for the exchange of components, aging models need to be applied. By means of the aging determined as well as the costs for replacing components, the operating costs c_{op} due to component wear can be finally calculated.

The approaches used in this section consider battery aging and brake pad wear. The effects

of battery aging are divided into cyclic and calendric aging. Parts of the methodologies developed within this section have been published [34, 35]. The following subsections describe the approaches for cost-optimal operating strategies in detail.

6.4.1. Cyclic Battery Aging

In general, the use of the battery leads to a trajectory of the state of charge SOC containing several micro cycles. The number of state of charge swings as well as their amplitudes are one of the key factors which influence the life span of the battery [88, 4]. In order to obtain costs due to cyclic aging, the resulting aging due to the state of charge profile needs to be determined.

Beside the fuel costs due to fuel consumption f_c , the first approach for cost-optimal operating strategies additionally considers costs due to cyclic battery aging. In the following, the methodology proposed as well as simulation results are presented.

Methodology

As shown in related work [26], a usual method to determine cyclic battery aging is given by applying a linear aging model on the basis of a constant energy or charge throughput of the battery. The term "linear aging" means that for example one cycle with a depth of discharge of 100% causes the same aging as 10 cycles with a depth of discharge of 10%. Thus, the charge throughput over the depth of discharge is assumed to be constant and given by means of the number of full discharge cycles. In contrast, the work of [95] uses a more detailed battery model and considers a severity factor map to weight the impacts of different battery temperatures ϑ_{BAT} and state of charge swings. As these factors mainly depend on characteristics like cell chemistry as well as anode and cathode compositions, a suitable map needs to be constructed with the help of data from battery manufacturers or exhaustive measurements. In general, the required data is only available with much effort and thus, another approach should be taken into account. In this section, an approach based on a non-linear charge throughput model is used in order to determine cyclic battery aging.

In the first part of the methodology, the optimization problem is defined by means of a general functional

$$J(SOC_0, I_{BAT}) = \int_{t_0}^{t_f} \left(c_1 \cdot \dot{m}_f(I_{BAT}, SOC, P_{DEM}) + c_2 \cdot \frac{I_{BAT}^2}{10^5} \right) dt, \quad (6.3)$$

where f_c represents the fuel consumption, I_{BAT} the battery current, c_1 the fuel costs per liter and c_2 a weighting factor to penalize high battery currents I_{BAT} . Additionally, a constant factor of 10^{-5} is used to keep both cost terms in similar value ranges. Whereas the fuel consumption f_c can be directly converted into costs by means of fuel costs c_{fuel} , several mathematical formulations can be used in order to describe battery aging and corresponding costs. In Equation 6.3, the square value of the battery current I_{BAT} is included to consider the use of battery energy E_{BAT} . Other mathematical relations are also suitable to penalize high changes of the state of charge SOC. For example, these functions can consider the absolute value of the battery current I_{BAT} or the battery power P_{BAT} .

As the optimization goal is to minimize the performance index J , the division by c_1 does

not influence the result. By introducing the weighting factor $\beta = c_2/c_1$, a more general formulation of Equation 6.3 is obtained:

$$J(SOC_0, I_{BAT}) = \int_{t_0}^{t_f} \left(\dot{m}_f(I_{BAT}, SOC, P_{DEM}) + \beta \cdot \frac{I_{BAT}^2}{10^5} \right) dt. \quad (6.4)$$

Now, β represents the weighting factor to prefer or reduce the use of the battery. For different values of the weighting factor β , optimal state of charge trajectories are calculated and a set of optimal solutions is obtained. In order to find the global optimum of the minimum costs, the rainflow counting algorithm is applied to evaluate the number of cycles with corresponding depths of discharge.

The rainflow counting algorithm originates from mechanical fatigue and stress analysis [65] and has been applied in many scientific areas [71, 103]. In addition, it has been shown that the rainflow counting algorithm is also suitable to determine the battery aging due to cyclic stress [46, 117, 118]. A short introduction to the basics of the algorithm is given in Appendix A.

By means of a battery aging model in combination with the rainflow counting algorithm, the calculated battery cycles are converted into an equivalent cyclic battery aging. Finally, the state of charge trajectory leading to the minimum costs is taken from the set of optimal solutions in order to determine the optimal operating strategy.

Figure 6.17 describes the methodology used in this section for a given weighting factor β . The optimal operating strategy is calculated in the first part. In the next step, the results are evaluated in order to determine the fuel consumption f_c as well as the cyclic battery aging. After a brief introduction to the methodology, the particular steps of Figure 6.17 "Optimization" and "Evaluation" are described in more detail.

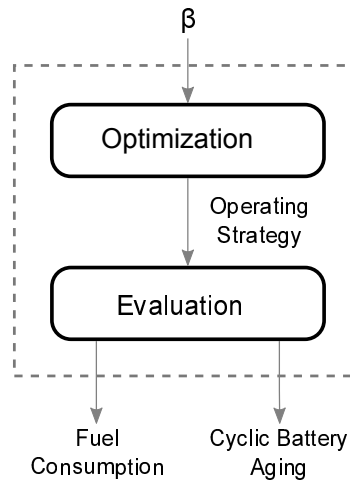


Figure 6.17.: Overview of the methodology. The methodology contains two main parts: The first part calculates the optimal operating strategy for a given value of the weighting factor β . Afterwards, the second part evaluates the fuel consumption f_c as well as the state of charge trajectory in order to determine cyclic battery aging.

The DP algorithm is applied to calculate the optimal operating strategy. In contrast to previous sections, the results cannot be directly used to determine cyclic battery aging. The reason

for this drawback is that the performance index J of Equation 6.4 only considers changes of the state of charge between two time steps.

In order to describe cyclic battery aging, a non-linear model is applied. Figure 6.18(a) depicts the relative capacity over the full discharge cycles [30]. As a capacity loss of 20% defines the battery's end-of-life, the maximum number of full discharge cycles is specified by 1500. In addition, Figure 6.18(b) shows the cyclic aging model which is based on measured data [66]. In contrast to a constant charge throughput model, the approach used in this work leads to a significantly higher cycle life especially for a low depth of discharge.

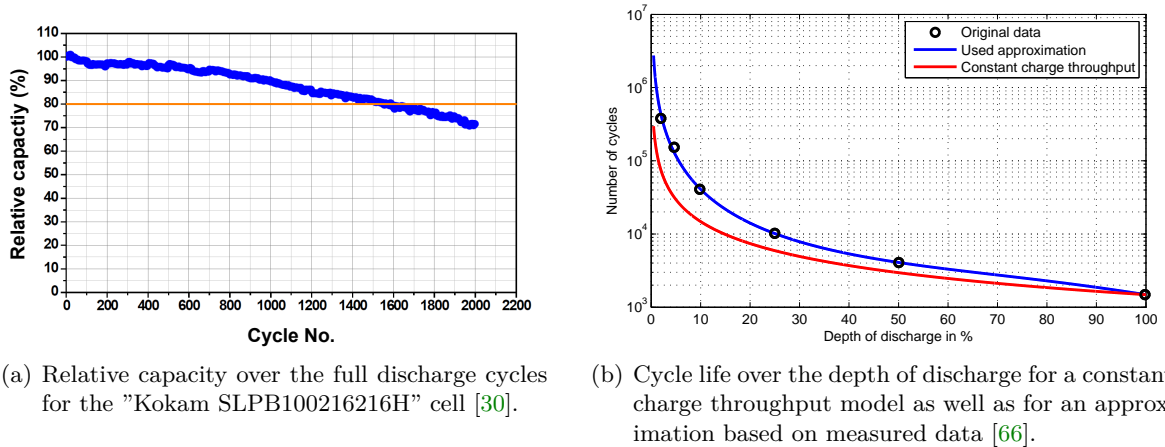


Figure 6.18.: Model used to describe cyclic battery aging. The left figure shows the relative battery capacity depending on the full discharge cycles. As a capacity loss of 20% defines the battery's end-of-life, the maximum number of full discharge cycles is specified by 1500. The right figure depicts the approach of this work in order to describe the cycle life over the depth of discharge. In contrast to a constant charge throughput model, the proposed approach leads to a significantly higher cycle life especially for a low depth of discharge.

As stated above, the defined dynamic program used for the optimization considers micro cycles between two time steps. Thus, the trend of the state of charge trajectory over longer time spans is neglected. Battery cycles containing high amplitudes are implicitly converted into an equivalent number of micro cycles. Although the depth of discharge is probably the same, the resulting battery aging differs due to the non-linearity of the cyclic aging model. As an alternative, a further state variable x can be introduced into the dynamic program. By means of this expansion, the actual height of the micro cycles is stored for positive and negative swings. This variant leads to high calculation times and can also not evaluate state of charge trajectories over longer time spans. Figure 6.19 graphically sketches this problem. Whereas the state of charge swing ΔSOC is determined by means of the expanded dynamic program, a swing containing different signs of the micro cycles such as ΔSOC_{max} cannot be evaluated. Because of this circumstance, the approach of Equation 6.4 is used in combination with a further evaluation. Although the calculation of the global optimum cannot be guaranteed, global optimality is nearly obtained after the evaluation of a plurality of state of charge trajectories.

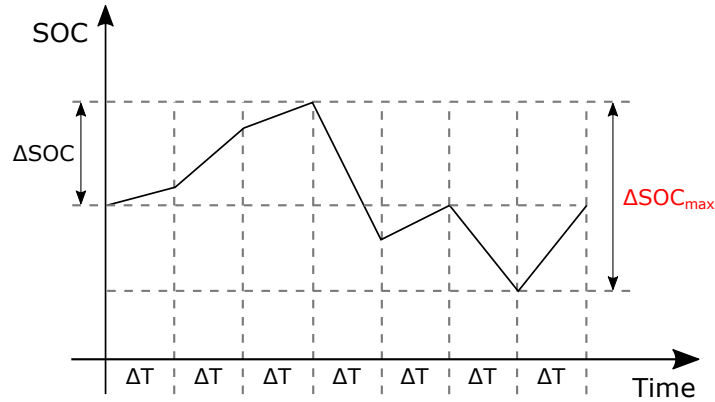


Figure 6.19.: Evaluation of a state of charge trajectory. Whereas cycles like ΔSOC are directly determined by means of an expanded dynamic program, swings such as ΔSOC_{max} can only be evaluated off-line.

To summarize, the following optimization problem is solved for different values of the weighting factor β and battery capacities C_{BAT} :

$$\begin{aligned} & \min_{u_k \in \mathcal{U}_k} \sum_{k=0}^{N-1} \left(\dot{m}_f(u_k, x_k, w_k, C_{BAT}) + \beta \cdot \frac{u_k^2}{10^5} \right) \cdot \Delta t \\ & \text{s.t.} \\ & x_{k+1} = \frac{u_k \cdot \Delta t}{C_{BAT} \cdot 3600} + x_k \\ & 0 \leq x_k \leq 1 \\ & -3 \cdot C_{BAT} \leq u_k \leq 10 \cdot C_{BAT} \\ & x_0 = 0.85 \\ & x_f = 0.85 \\ & x_k \in \mathcal{X}_k \\ & u_k \in \mathcal{U}_k \end{aligned}$$

where the battery current I_{BAT} is used as control variable u_k , the battery's state of charge SOC as state variable x_k and the power demand P_{DEM} as disturbance w_k . In addition, limits of the control and state variables as well as a sampling time Δt of 1 s are considered.

In the evaluation step of the methodology, the fuel consumption f_c and cyclic battery aging are determined for a given weighting factor β . Whereas the fuel consumption f_c can be directly derived from the optimization results, the calculation of the cyclic battery aging needs another approach. As described before, the rainflow counting algorithm is used to obtain the number of micro cycles and swings of the state of charge trajectory. After the evaluation step, the corresponding fuel consumption f_c as well as cyclic battery aging is obtained for a given weighting factor β . The methodology described is repeated for several values of the weighting factor β in order to derive a set of optimal solutions. The globally optimal solution is finally approximated by means of the optimum of locally optimal operating strategies. Further parameters such as fuel costs per liter c_{fuel} or battery costs per kWh c_{bat} need to be defined in order to obtain cost-optimal operating strategies.

Results

Firstly, the aging models of Figure 6.18 are compared by means of simulations. For this purpose, different weighting factors β and driving cycles are used. Table 6.9 shows the corresponding results and depicts the fuel consumption f_c as well as the cyclic battery aging of constant and non-linear charge throughput models. It can be seen that the charge throughput model used in this work leads to significantly lower cyclic aging compared to the constant model. In addition, it can be concluded that the constant charge throughput model causes too pessimistic results in terms of cyclic aging.

Table 6.9.: Comparison of cyclic battery aging due to constant and non-linear charge throughput models for different weighting factors β .

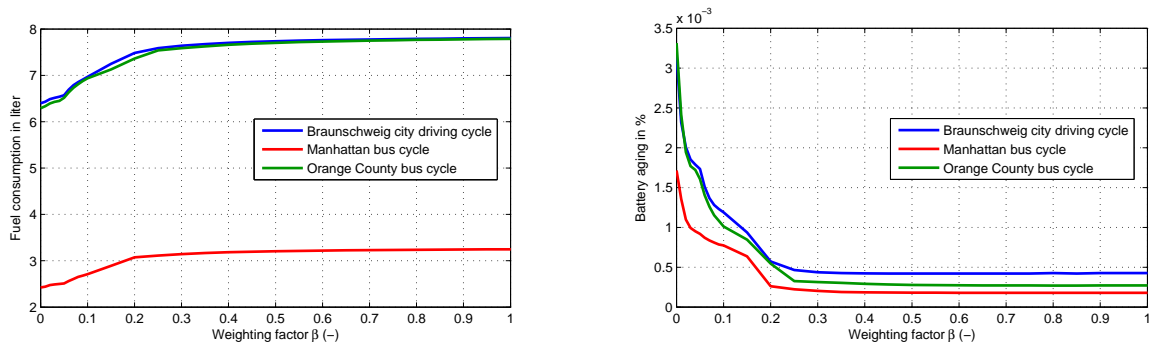
driving cycle	weighting factor β	fuel consumption f_c	cyclic aging (non-linear model)	cyclic aging (constant model)
Braunschweig city driving cycle	0	6.39 lit.	$3.16 \cdot 10^{-5}$	$2.57 \cdot 10^{-4}$
	$1 \cdot 10^{-1}$	6.96 lit.	$1.19 \cdot 10^{-5}$	$1.18 \cdot 10^{-4}$
	$2 \cdot 10^{-1}$	7.48 lit.	$5.71 \cdot 10^{-6}$	$6.87 \cdot 10^{-5}$
	$5 \cdot 10^{-1}$	7.73 lit.	$4.21 \cdot 10^{-6}$	$4.83 \cdot 10^{-5}$
	1	7.81 lit.	$4.27 \cdot 10^{-6}$	$4.79 \cdot 10^{-5}$
Manhattan bus cycle	0	2.42 lit.	$1.72 \cdot 10^{-5}$	$1.38 \cdot 10^{-4}$
	$1 \cdot 10^{-1}$	2.71 lit.	$7.74 \cdot 10^{-6}$	$7.66 \cdot 10^{-5}$
	$2 \cdot 10^{-1}$	3.07 lit.	$2.62 \cdot 10^{-6}$	$3.59 \cdot 10^{-5}$
	$5 \cdot 10^{-1}$	3.21 lit.	$1.81 \cdot 10^{-6}$	$2.23 \cdot 10^{-5}$
	1	3.24 lit.	$1.78 \cdot 10^{-6}$	$2.19 \cdot 10^{-5}$
Orange County bus cycle	0	6.29 lit.	$3.32 \cdot 10^{-5}$	$2.65 \cdot 10^{-4}$
	$1 \cdot 10^{-1}$	6.94 lit.	$1.01 \cdot 10^{-5}$	$1.07 \cdot 10^{-4}$
	$2 \cdot 10^{-1}$	7.36 lit.	$5.45 \cdot 10^{-6}$	$6.68 \cdot 10^{-5}$
	$5 \cdot 10^{-1}$	7.70 lit.	$2.78 \cdot 10^{-6}$	$3.14 \cdot 10^{-5}$
	1	7.78 lit.	$2.71 \cdot 10^{-6}$	$2.70 \cdot 10^{-5}$

In a further step, the influence of the weighting factor β on the cost-optimal operating strategies is evaluated. Figures 6.20(a) and 6.20(b) depict the optimum values of fuel consumption f_c and cyclic battery aging for the Braunschweig city driving cycle. The results show that higher values of the weighting factor β lead to a lower cyclic aging of the battery. Obviously, the fuel consumption f_c increases with the weighting factor β as the EGU is more frequently used to fulfill the power demands P_{DEM} of the driving cycle.

In order to determine the optimal operating costs, the parameters fuel costs per liter c_{fuel} as well as battery costs per kWh c_{bat} need to be defined. By means of these parameters, it is possible to relate the set of optimal operating strategies of Figure 6.20 to equivalent costs. The minimum of these costs provides the optimal operating costs c_{op} .

Based on the reference configuration of Section 6.1, parameter studies were performed. In order to cover a broad parameter range, fuel costs c_{fuel} of 1 €/lit. and 3 €/lit. as well as battery costs c_{bat} of 200 €/kWh and 1000 €/kWh are chosen.

Figure 6.21 depicts the operating costs c_{op} over the weighting factor β for different fuel costs c_{fuel} and battery costs c_{bat} by means of the Braunschweig city driving cycle. As the



(a) Fuel consumption f_c depending on the weighting factor β .

(b) Cyclic battery aging depending on the weighting factor β .

Figure 6.20.: Influence of the weighting factor β . The fuel consumption f_c and cyclic battery aging are compared for different values of the weighting factor β . As a higher value of β leads to a lower use of the battery, the cyclic battery aging decreases. In contrast, the fuel consumption f_c increases for higher values of the weighting factor β in order to fulfill the power demand P_{DEM} of the driving cycle.

minimum operating costs c_{op} are found for low values of the weighting factor β , the scale is limited by 1. The results of the other two driving cycles are presented in Appendix C.

Until now, the battery capacity C_{BAT} was defined by 40 Ah. In the following, the influence of variable battery capacities C_{BAT} on the minimum operating costs c_{op} is evaluated. For this purpose, a set of optimal operating strategies is calculated by means of several values of the weighting factor β and battery capacities C_{BAT} . Afterwards, the minimum operating costs c_{op} are evaluated for given battery capacities C_{BAT} as well as fuel costs c_{fuel} and battery costs c_{bat} .

Figure 6.22 depicts the minimum operating costs c_{op} and fuel costs c_{fuel} over the battery capacity C_{BAT} . Additionally, different values of fuel costs c_{fuel} and battery costs c_{bat} as well as the Braunschweig city driving cycle are used. The costs due to cyclic battery aging are represented by means of the difference between the operating costs c_{op} and fuel costs due to fuel consumption f_c . The results of the evaluated capacity range show two effects:

- Bigger battery capacities C_{BAT} lead to lower fuel consumptions f_c as the recuperation potential can be better exploited.
- Bigger battery capacities C_{BAT} reduce the cyclic aging effects. This circumstance can be justified by means of the applied non-linear battery aging model. As a bigger capacity leads to lower depth of discharges, the cyclic aging is reduced. As only cyclic aging effects are considered, the higher costs for exchanging the battery are not included in this simulation study.

The corresponding results of the other two driving cycles are presented in Appendix C.

In this subsection, the optimal operating strategies leading to minimum operating costs c_{op} were calculated for a hybrid bus. If the life cycle costs c_{life} should be minimized, the scaling of operating costs c_{op} unfortunately provides an estimation. A more accurate approach is given by including the costs for replacing components into the optimization process. In the

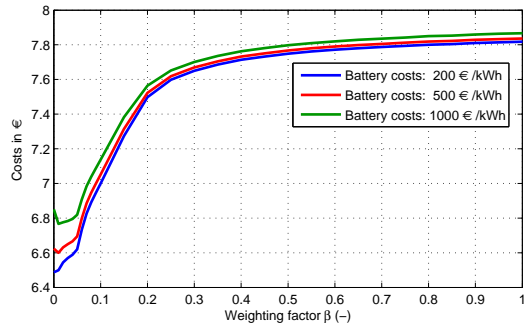
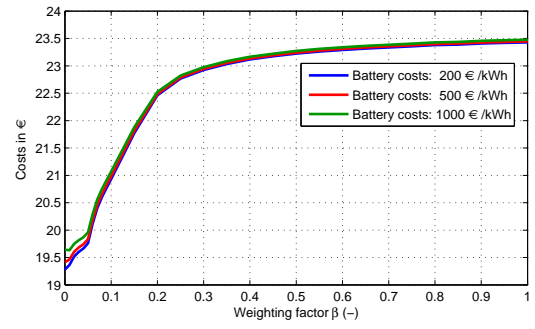
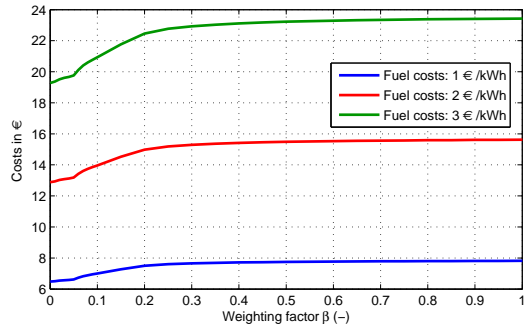
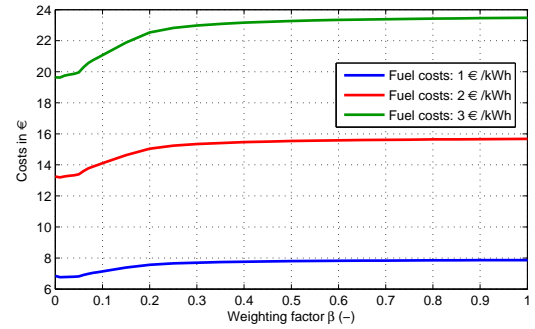
(a) Fuel costs c_{fuel} of 1 €/lit. and variable battery costs c_{bat} .(b) Fuel costs c_{fuel} of 3 €/lit. and variable battery costs c_{bat} .(c) Battery costs c_{bat} of 200 €/kWh and variable fuel costs c_{fuel} .(d) Battery costs c_{bat} of 1000 €/kWh and variable fuel costs c_{fuel} .

Figure 6.21.: Variable fuel costs c_{fuel} and battery costs c_{bat} over the weighting factor β . The optimum for given fuel costs c_{fuel} and battery costs c_{bat} is determined by means of the minimum operating costs c_{op} over the weighting factor β .

following, a methodology to minimize life cycle costs c_{life} including the exchange of batteries is presented.

6.4.2. Calendric Battery Aging

In applications such as freight traffic not only the operating costs c_{op} but also the life cycle costs c_{life} of vehicles are probably of high significance. As the methodology of Section 6.4.1 minimizes the operating costs c_{op} for one driving cycle, another approach needs to be taken into account to optimize life cycle costs c_{life} . For this purpose, calendric battery aging effects are additionally considered in the optimization problem. For a certain vehicle life span, the optimal number of batteries N_{BAT} is calculated on the basis of cyclic and calendric battery aging effects.

Methodology

In order to model calendric aging effects, a linear approach is taken into account. For this purpose, it is assumed that the battery can withstand a defined time span if no cyclic aging occur. In addition, the total number of driving cycles N_{CYC} during the vehicle life span needs

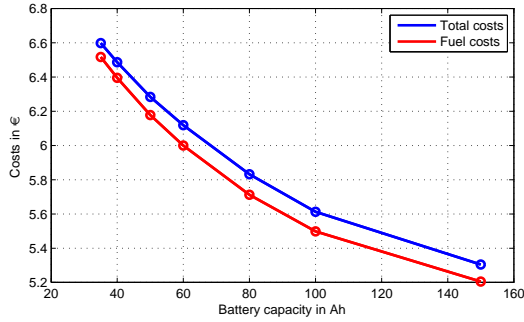
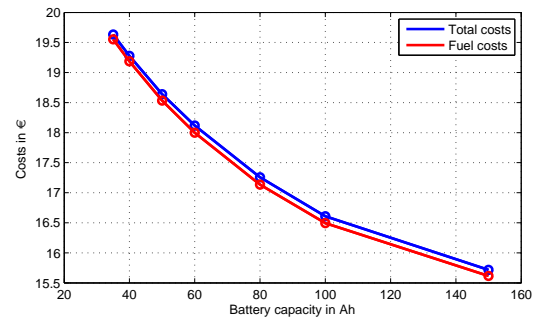
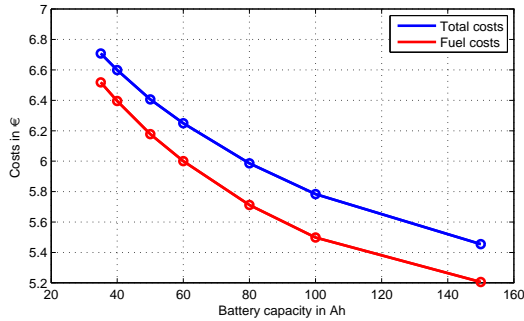
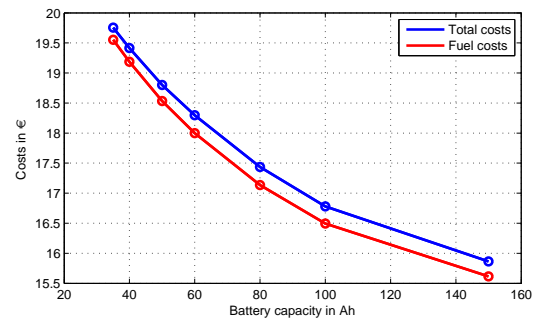
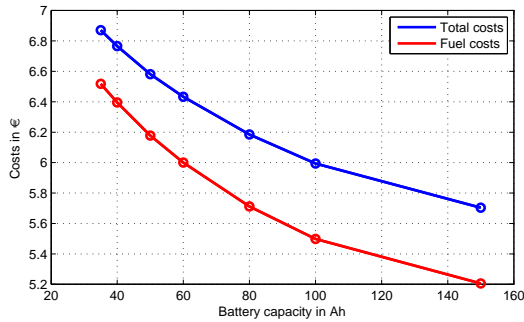
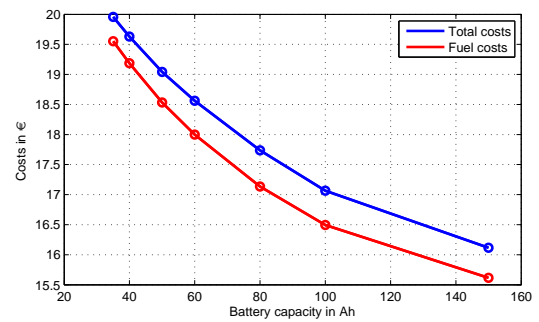
(a) Fuel costs c_{fuel} of 1 €/lit. and battery costs c_{bat} of 200 €/kWh.(b) Fuel costs c_{fuel} of 3 €/lit. and battery costs c_{bat} of 200 €/kWh.(c) Fuel costs c_{fuel} of 1 €/lit. and battery costs c_{bat} of 500 €/kWh.(d) Fuel costs c_{fuel} of 3 €/lit. and battery costs c_{bat} of 500 €/kWh.(e) Fuel costs c_{fuel} of 1 €/lit. and battery costs c_{bat} of 1000 €/kWh.(f) Fuel costs c_{fuel} of 3 €/lit. and battery costs c_{bat} of 1000 €/kWh.

Figure 6.22.: The figures show the minimum operating costs c_{op} as well as the fuel costs due to fuel consumption f_c depending on the battery capacity C_{BAT} . Furthermore, different values of fuel costs c_{fuel} and battery costs c_{bat} as well as the Braunschweig city driving cycle are used. The costs due to cyclic battery aging are represented by means of the difference between operating costs c_{op} and fuel costs due to fuel consumption f_c .

to be known. By means of these two parameters, the calendric battery aging per driving cycle is finally obtained. Further effects such as operating and shelf temperature are neglected for simplicity.

As the modeled calendric battery effects are not influenced by means of the operating strategy, the results of the previous subsection can be used again. To describe the total battery aging, the calculated cyclic aging is expanded with the help of an offset representing the calendric aging. By means of the battery aging per cycle and the number of driving cycles N_{CYC} over the defined vehicle life span, the total battery aging is calculated. The results obtained need to be appropriately rounded as obviously only integer numbers of batteries N_{BAT} are replaced over the life time.

Results

Based on the methodology described above, the calendric battery aging is calculated for a defined vehicle life span of 10 years. In addition, the operating hours h_{op} of the hybrid bus are defined by 2000 and 5000 hours/year, respectively. By means of the duration of the driving profiles used in this work, the total number of driving cycles N_{CYC} over the vehicle life span is calculated. Table 6.10 depicts the calendric battery aging for different driving cycles on the basis of the above mentioned parameters.

Table 6.10.: Number of total driving cycles N_{CYC} and calendric battery aging per cycle.

driving cycle	operating hours (h/year)	life span (years)	# cycles (-)	calendric aging (1/cycle)
Braunschweig city driving cycle	2000	10	41379	$2.4 \cdot 10^{-5}$
	5000	10	103448	$9.7 \cdot 10^{-6}$
Manhattan bus cycle	2000	10	66116	$1.5 \cdot 10^{-5}$
	5000	10	165290	$6.1 \cdot 10^{-6}$
Orange County bus cycle	2000	10	37716	$2.7 \cdot 10^{-5}$
	5000	10	94290	$1.1 \cdot 10^{-5}$

In order to determine the cyclic and calendric aging of batteries, the calculated set of different weighting factors β of the previous Section 6.4.1 is used again. As mentioned before, this approach is valid since the calendric life of the battery cannot be controlled by means of the operating strategy. As the calendric aging represents a constant offset, the optimal operating strategy would be the same compared to the pure cyclic battery aging approach.

Until now, only the operating costs c_{op} for one driving cycle are minimized. However, if the life cycle costs c_{life} should be calculated, then the costs for the replacement of batteries are important. The previously obtained operating costs c_{op} cannot be linearly scaled over a life span as only an integer number of batteries N_{BAT} is used. In order to overcome this drawback, another approach is introduced, which leads to the following definition of life cycle costs

$$c_{life} = N_{CYC} \cdot c_{fuel} \cdot f_c + N_{BAT} \cdot c_{bat} \cdot E_{BAT}, \quad (6.5)$$

where N_{CYC} represents the total number of driving cycles, c_{fuel} the fuel costs per liter, f_c the fuel consumption, N_{BAT} the number of batteries, c_{bat} the battery costs per kWh and E_{BAT} the energy content of the battery.

Table 6.11 depicts the share of calendric and cyclic battery aging leading to the minimum life cycle costs c_{life} for the Braunschweig city driving cycle as well as fuel costs c_{fuel} of 1 €/liter and battery costs c_{bat} of 500 €/kWh. The variable parameters are defined by the battery capacity C_{BAT} and operating hours h_{op} . The results of the other two driving cycles are shown in Appendix C.

Table 6.11.: Share of battery aging effects based on the Braunschweig city driving cycle, fuel costs c_{fuel} of 1 €/liter and battery costs c_{bat} of 500 €/kWh. The variable parameters are defined by the battery capacity C_{BAT} and operating hours h_{op} . By means of the number of driving cycles N_{CYC} , the total battery aging as well as the needed number of batteries N_{BAT} are determined.

battery capacity (Ah)	operating hours (h/year)	cyclic aging (1/cycle)	calendric aging (1/cycle)	battery aging (1/cycle)	total battery aging (-)	number of batteries (-)
40	2000	$2.31 \cdot 10^{-5}$	$2.42 \cdot 10^{-5}$	$4.73 \cdot 10^{-5}$	1.95	2
40	5000	$2.59 \cdot 10^{-5}$	$9.67 \cdot 10^{-6}$	$3.56 \cdot 10^{-5}$	3.68	4
60	2000	$1.84 \cdot 10^{-5}$	$2.42 \cdot 10^{-5}$	$4.26 \cdot 10^{-5}$	1.77	2
60	5000	$1.84 \cdot 10^{-5}$	$9.67 \cdot 10^{-6}$	$2.81 \cdot 10^{-5}$	2.90	3
80	2000	$2.08 \cdot 10^{-5}$	$2.42 \cdot 10^{-5}$	$4.50 \cdot 10^{-5}$	1.86	2
80	5000	$1.47 \cdot 10^{-5}$	$9.67 \cdot 10^{-6}$	$2.44 \cdot 10^{-5}$	2.51	3
100	2000	$1.58 \cdot 10^{-5}$	$2.42 \cdot 10^{-5}$	$4.00 \cdot 10^{-5}$	1.65	2
100	5000	$1.58 \cdot 10^{-5}$	$9.67 \cdot 10^{-6}$	$2.55 \cdot 10^{-5}$	2.64	3

Figure 6.23 depicts the minimum life cycle costs c_{life} depending on the battery capacity C_{BAT} as well as operating hours h_{op} of 2000 h/year and 5000 h/year, respectively. The driving profile is defined by means of the Braunschweig city driving cycle. Fuel costs c_{fuel} of 1 €/liter and 3 €/liter as well as battery costs c_{bat} of 200 €/kWh, 500 €/kWh and 1000 €/kWh are used in order to cover a set of current and future price levels. The evaluated battery capacity range has a defined maximum by means of 150 Ah. As a constant power of the EGU of 160 kW is assumed, the power demand P_{DEM} of the driving cycle provides a minimum limit in terms of the battery capacity C_{BAT} . By means of the calculated results, the optimum battery capacity C_{BAT} leading to minimum life cycle costs c_{life} can be determined for a variable set of prices.

The corresponding results of the other two driving cycles are shown in Appendix C.

In this subsection, cyclic and calendric aging effects of the battery were considered in order to optimize life cycle costs c_{life} of a hybrid bus. Since the operating strategy also influences the use of the mechanical brakes, the brake pad wear depicts another parameter which can be included into the optimization problem. The following subsection describes a possible approach to solve this problem.

6.4.3. Brake Wear

This subsection describes cost-optimal operating strategies with battery aging as well as brake wear considered. For this purpose, the previous approach of Section 6.4.2 is expanded with the help of a mechanical brake model. In case of negative power at the wheels ($P_W < 0$) of the

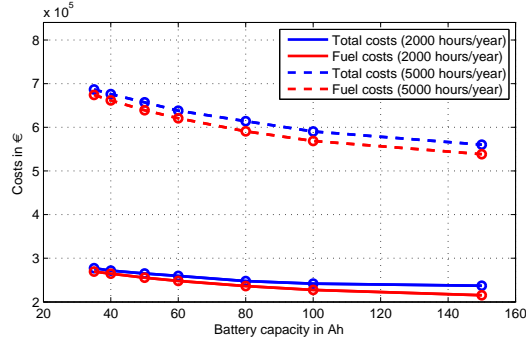
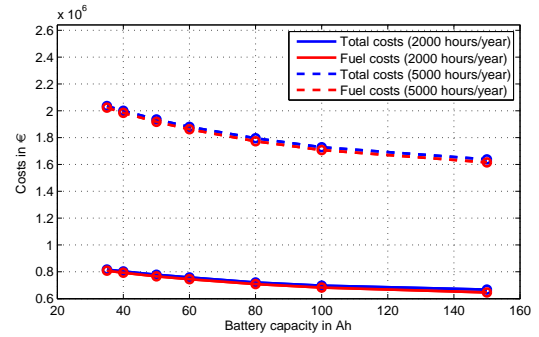
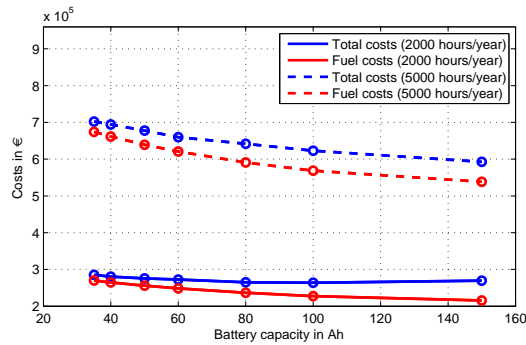
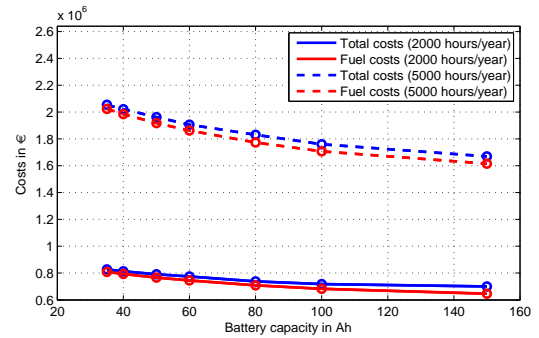
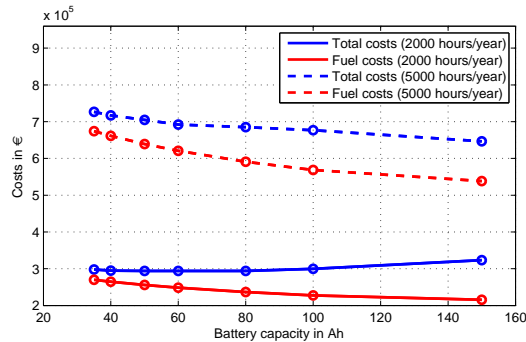
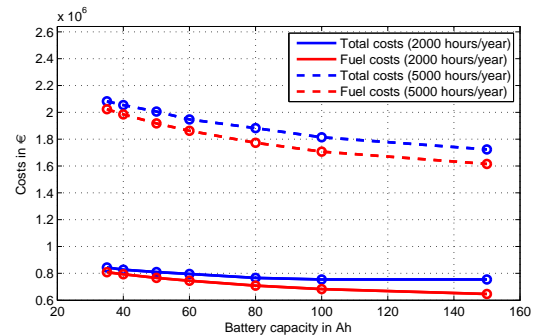
(a) Fuel costs c_{fuel} of 1 €/lit. and battery costs c_{bat} of 200 €/kWh.(b) Fuel costs c_{fuel} of 3 €/lit. and battery costs c_{bat} of 200 €/kWh.(c) Fuel costs c_{fuel} of 1 €/lit. and battery costs c_{bat} of 500 €/kWh.(d) Fuel costs c_{fuel} of 3 €/lit. and battery costs c_{bat} of 500 €/kWh.(e) Fuel costs c_{fuel} of 1 €/lit. and battery costs c_{bat} of 1000 €/kWh.(f) Fuel costs c_{fuel} of 3 €/lit. and battery costs c_{bat} of 1000 €/kWh.

Figure 6.23.: Comparison of life cycle costs c_{life} for the Braunschweig city driving cycle depending on the battery capacity C_{BAT} and operating hours h_{op} . For different values of fuel costs c_{fuel} and battery costs c_{bat} , the optimal battery capacity C_{BAT} leading to the minimum life cycle costs c_{life} can be determined.

driving cycle, the operating strategy either provides this power by means of the mechanical brakes or the use of the electric traction motors in order to recuperate energy. As recuperation and mechanical braking lead to corresponding component wear, the calculated operating strategy should provide power splits leading to minimum life cycle costs c_{life} . In the following, the methodology proposed as well as results based on simulations are presented.

Methodology

In order to determine the costs due to brake wear, a model of the mechanical brake is needed. For this purpose, the brake model based on the work of [108] is used, which is depicted in Figure 6.24. The model shows a linear relation between brake wear and cumulative braking energy for different temperatures. For simplicity, a constant operating temperature is assumed which reduces the number of model parameters. Due to the linearity of the model, the wear is a function of the braking energy. The cumulative work done by the brake is only needed to define the corresponding slope of the function.

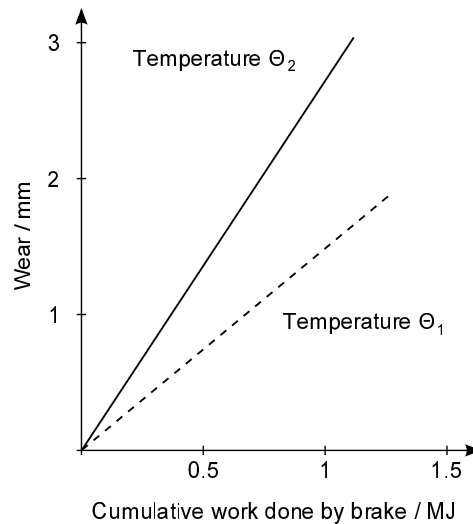


Figure 6.24.: Illustration of the brake model (slightly modified from [108]). The model shows a linear relation between wear and cumulative work for different operating temperatures.

The brake model applied in this work contains one parameter which defines the slope of the linear function. To calculate this parameter, the cumulative braking energy for a normalized brake wear of 100% needs to be known. Table 6.12 depicts the cumulative brake energy demand of all driving cycles used in this work if no recuperation is taken into account. Furthermore, it is assumed that the mechanical brakes can withstand 3 years if no recuperation is taken into account and the bus is operated with annual operating hours h_{op} of 5000 h/year on the basis of a given driving cycle. The costs for replacing the mechanical brakes $c_{comp,brake}$ are estimated by 5000 €. By means of these assumptions, the mechanical brake energies can be directly converted into equivalent braking costs.

In the next step, the life cycle costs c_{life} including the exchange of batteries and brakes are given by

$$c_{life} = N_{CYC} \cdot c_{fuel} \cdot f_c + N_{BAT} \cdot c_{bat} \cdot E_{BAT} + N_{BRAKE} \cdot c_{comp,brake}, \quad (6.6)$$

Table 6.12.: Total brake energy demands of different driving cycles.

driving cycle	total brake energy demand (kWh)
Braunschweig city driving cycle	11.3
Manhattan bus cycle	4.6
Orange County bus cycle	10.9

where N_{CYC} represents the total number of driving cycles, c_{fuel} the fuel costs per liter, N_{BAT} the number of batteries, c_{bat} the battery costs, E_{BAT} the energy content of the battery, N_{BRAKE} the number of brakes and $c_{comp,brake}$ the brake costs.

To find the optimal operating strategy, the set of optimal solutions of Section 6.4.1 is used again. As the weighting factor β was applied to weight the use of the battery, the power split between recuperation and mechanical braking is implicitly influenced. As the recuperation power is limited by means of the electric traction motors as well as the maximum charge power of the battery, a minimum limit of braking costs is given. Furthermore, it can be concluded that a higher value of the weighting factor β leads to a preferable use of the mechanical brakes and vice-versa. By means of this approach, it is possible to obtain the minimum life cycle costs c_{life} for given fuel costs c_{fuel} , battery costs c_{bat} and brake costs $c_{comp,brake}$. In the following, results based on simulations are shown by means of a parameter study.

Results

To demonstrate the methodology described before, a small parameter study was performed. The variable parameters are defined by means of the driving cycle, battery capacity C_{BAT} , operating hours h_{op} , fuel costs c_{fuel} and battery costs c_{bat} . Furthermore, a constant vehicle life span of 10 years and brake costs $c_{comp,brake}$ due to the exchange of brakes of 5000 € are assumed.

Table 6.13 depicts the optimal share of operating costs c_{op} and life cycle costs c_{life} for the Braunschweig city driving cycle. In addition, fuel costs c_{fuel} of 1 €/liter as well as battery costs c_{bat} of 500 €/kWh are used, which represent usual values of today. In contrast, Table 6.14 depicts the results of a future scenario. For this purpose, fuel costs c_{fuel} of 2 €/liter and battery costs c_{bat} of 200 €/kWh are assumed.

Both tables show that the operating costs c_{op} as well as the life cycle costs c_{life} are mainly influenced by means of the fuel costs c_{fuel} and battery costs c_{bat} . The results of the other two driving cycles are presented in Appendix C.

In this section, cost-optimal operating strategies considering battery aging and brake pad wear were presented. The approach can be used to minimize operating costs c_{op} as well as life cycle costs c_{life} of HEVs. The simulation results show that the ratio of braking costs is relatively small compared to the overall life cycle costs c_{life} .

Table 6.13.: Share of operating costs c_{op} and life cycle costs c_{life} for given fuel costs c_{fuel} of 1 €/liter and battery costs c_{bat} of 500 €/kWh. The life span of the bus is defined by 10 years.

operating costs per cycle for the Braunschweig city driving cycle					
battery capacity (Ah)	operating hours (h/year)	fuel costs (€)	battery costs (€)	brake costs (€)	total costs (€)
40	2000	6.43	0.34	0.06	6.83
40	5000	6.41	0.26	0.06	6.73
80	2000	5.71	0.65	0.03	6.39
80	5000	5.74	0.35	0.03	6.12

life cycle costs for the Braunschweig city driving cycle					
battery capacity (Ah)	operating hours (h/year)	fuel costs (k€)	battery costs (k€)	brake costs (k€)	total costs (k€)
40	2000	266.2	14.4	5	285.6
40	5000	663.1	28.8	10	701.9
80	2000	236.4	28.8	5	270.2
80	5000	594.7	43.2	5	642.9

Table 6.14.: Share of operating and life cycle costs for given fuel costs of 2 €/liter and battery costs of 200 €/kWh. The life span of the bus is defined by 10 years.

operating costs per cycle for the Braunschweig city driving cycle					
battery capacity (Ah)	operating hours (h/year)	fuel costs (€)	battery costs (€)	brake costs (€)	total costs (€)
40	2000	12.79	0.16	0.06	13.01
40	5000	12.79	0.12	0.06	12.97
80	2000	11.42	0.26	0.03	11.71
80	5000	11.42	0.18	0.03	11.63

life cycle costs for the Braunschweig city driving cycle					
battery capacity (Ah)	operating hours (h/year)	fuel costs (k€)	battery costs (k€)	brake costs (k€)	total costs (k€)
40	2000	529.3	8.6	5	542.9
40	5000	1323.3	14.4	10	1347.7
80	2000	472.7	11.5	5	489.2
80	5000	1181.8	23.0	5	1209.8

6.5. Operating Strategies Including Thermal Effects

In the approaches of Section 6.4, the thermal effects of components were neglected. However, a possible exceeding of thermal limits may be crucial in terms of component life spans. As the operating strategy mainly influences component temperatures, thermal limits need to be considered in the optimization problem. Since DP is applied for calculating the globally optimal operating strategy, the number of state variables should be low in order to avoid the "curse of dimensionality". In the following, a methodology to obtain optimal operating strategies including thermal limits of the battery is described.

6.5.1. Methodology

It is assumed that the EGU as well as the electric traction motors of the bus are appropriately scaled and do not exceed thermal limits for a given operating strategy. By means of this simplification, the temperature of the battery ϑ_{BAT} remains as critical thermal state and therefore is included into the optimization problem. In addition to the state of charge SOC, the battery temperature ϑ_{BAT} defines the second state variable x of the dynamic program. Furthermore, the cooling power P_{COOL} of the battery provides the second control variable u . The thermal part of the battery is modeled by means of a point mass m_{bat} and a corresponding specific heat capacity $c_{p,bat}$. Thus, the change of the battery temperature ϑ_{BAT} can be described as follows

$$\frac{d\vartheta_{BAT}}{dt} = \frac{1}{c_{p,bat} \cdot m_{bat}} \cdot (P_{LOSS,BAT} - P_{COOL}) \quad (6.7)$$

$$= \frac{1}{c_{p,bat} \cdot m_{bat}} \cdot (I_{BAT}^2 \cdot R_{BAT}(\vartheta_{BAT}) - P_{COOL}), \quad (6.8)$$

where ϑ_{BAT} represents the battery temperature, $P_{LOSS,BAT}$ the electrical losses, P_{COOL} the cooling power, I_{BAT} the current and R_{BAT} the internal battery resistance. Two different relations between R_{BAT} and the battery temperature ϑ_{BAT} are considered, which are shown in Figure 6.25. Whereas the temperature-dependent approach uses a generic, non-linear approach, the other approach assumes a constant battery resistance R_{BAT} based on a reference temperature of 20 °C.

In order to determine the electrical power P_{EL} used to provide the cooling power P_{COOL} , a further relation is introduced by means of the coefficient of performance

$$COP = \frac{P_{COOL}}{P_{EL}}. \quad (6.9)$$

For simplicity, constant coefficient of performance values are assumed in the following simulation studies. The electrical power P_{EL} due to the battery cooling P_{COOL} is added to the power of the auxiliary devices P_{AUX} . The described approach allows to integrate the feedback loop between battery temperature ϑ_{BAT} , cooling power P_{COOL} and electrical power P_{EL} into the optimization problem.

Figure 6.26 shows the thermal model based on the work of [38, 77] which is used to determine the temperature of the battery ϑ_{BAT} . The electrical power loss $P_{LOSS,BAT}$ and the cooling power P_{COOL} represent the control variables u . Furthermore, the model outputs are given by means of the battery temperature ϑ_{BAT} and the electrical power P_{EL} .

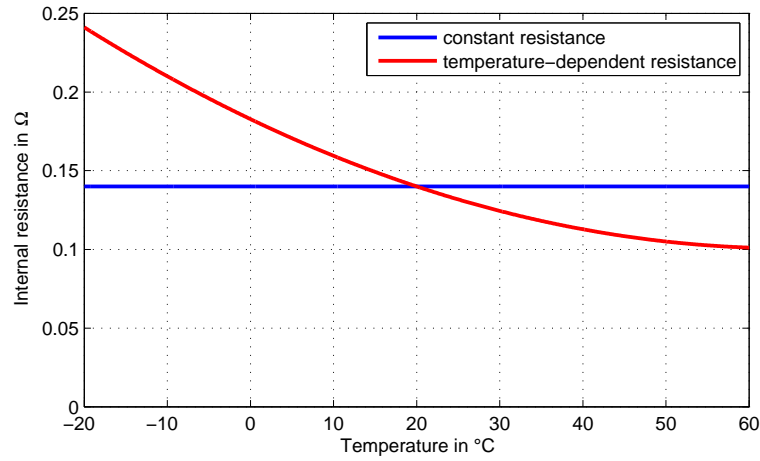


Figure 6.25.: Two models to describe the internal battery resistance R_{BAT} of the battery pack depending on the battery temperature ϑ_{BAT} . Whereas the temperature-dependent function considers the influence of the battery temperature ϑ_{BAT} , the constant approximation neglects this effect.

To summarize, the following optimization problem is solved for different models of the internal resistance R_{BAT} as well as coefficients of performance COP:

$$\begin{aligned}
 & \min_{u_{1,k} \in \mathcal{U}_{1,k}, u_{2,k} \in \mathcal{U}_{2,k}} \sum_{k=0}^{N-1} \dot{m}_f(u_{1,k}, u_{2,k}, x_{1,k}, R_{BAT}(x_{2,k}), w_k, COP) \cdot \Delta t \\
 & \text{s.t.} \\
 & x_{1,k+1} = \frac{u_{1,k} \cdot \Delta t}{C_{BAT} \cdot 3600} + x_{1,k} \\
 & x_{2,k+1} = \frac{1}{c_{p,bat} \cdot m_{bat}} \cdot \left(u_{1,k}^2 \cdot R_{BAT}(x_{2,k}) - u_{2,k} \right) \cdot \Delta t + x_{2,k} \\
 & 0 \leq x_{1,k} \leq 1 \\
 & 20 \leq x_{2,k} \leq 30 \\
 & -120 \leq u_{1,k} \leq 400 \\
 & 0 \leq u_{2,k} \leq 10^4 \\
 & x_{1,0} = 0.85 \\
 & x_{1,f} = 0.85 \\
 & x_{2,0} = 25 \\
 & x_{2,f} = 25 \\
 & x_{1,k} \in \mathcal{X}_{1,k} \\
 & x_{2,k} \in \mathcal{X}_{2,k} \\
 & u_{1,k} \in \mathcal{U}_{1,k} \\
 & u_{2,k} \in \mathcal{U}_{2,k}
 \end{aligned}$$

where the battery current I_{BAT} is used as control variable $u_{1,k}$, the cooling power P_{COOL} as control variable $u_{2,k}$, the battery's state of charge SOC as state variable $x_{1,k}$, the temperature

of the battery ϑ_{BAT} as state variable $x_{2,k}$ and the power demand P_{DEM} as disturbance w_k . In addition, limits of the control and state variables as well as a sampling time Δt of 1 s are considered.

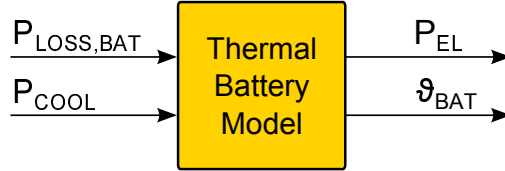


Figure 6.26.: Thermal battery model with corresponding input and output signals. The thermal behavior of the battery is modeled by means of a point mass with corresponding battery mass m_{bat} and specific heat capacity $c_{p,bat}$.

6.5.2. Results

In the following simulations, the reference configuration of the hybrid electric bus containing a battery capacity C_{BAT} of 40 Ah and a maximum power of the EGU $P_{EUG,max}$ of 160 kW is used. Furthermore, the variable battery parameters are defined by means of different temperature ranges, constant or temperature-dependent internal resistances and coefficients of performance COP.

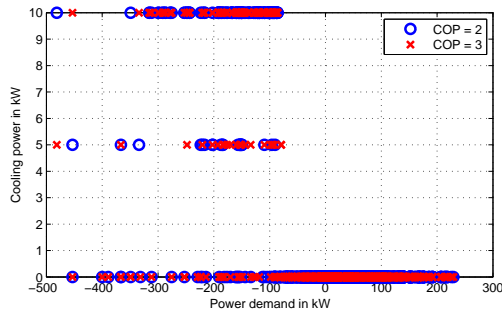
All simulations have in common that the initial battery temperature $\vartheta_{BAT,0}$ and final battery temperature $\vartheta_{BAT,f}$ is determined by 25 °C. The initial parameters of the dynamic program are the same as shown in Section 6.1. In addition, the maximum cooling power $P_{COOL,max}$ is defined by 10 kW discretized in 5 kW steps and the discretization of the battery temperature ϑ_{BAT} is prescribed by 1 °C.

Table 6.15 presents the results of the parameter studies performed and depicts the fuel consumption f_c depending on different driving cycles, temperature-dependences of the internal resistance R_{BAT} and coefficients of performance COP. The results show that the defined values of the coefficient of performance COP do not influence the fuel consumption f_c . This behavior can be justified by the fact that the battery cooling is only activated if high recuperation power is available. The left column of Figure 6.27 shows this relation for different driving cycles. Furthermore, the fuel consumption f_c tends to be higher for a constant internal resistance R_{BAT} of the battery. In case of a temperature-dependent resistance model, the optimal operating strategy tries to keep the battery temperature ϑ_{BAT} on a higher level within the allowed temperature range. Thus, the internal resistance R_{BAT} as well as the power loss $P_{LOSS,BAT}$ decrease compared to the constant approach and an improved efficiency η in terms of charging and discharging is achieved. This circumstance leads to different fuel consumptions f_c between constant and temperature-dependent resistance models but also to an increased battery aging due to higher temperature levels. The battery temperatures ϑ_{BAT} over time are compared for both resistance models in the right column of Figure 6.27.

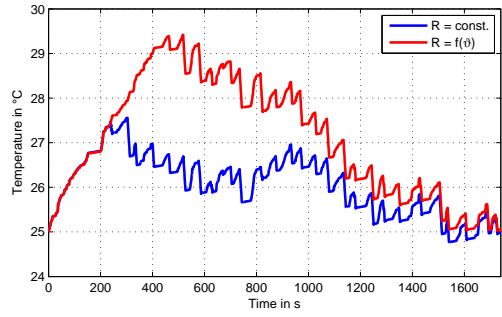
Table 6.15.: Results of parameter studies. The variable parameters are defined by means of the driving cycle, constant or temperature-dependent resistance models and the coefficient of performance COP. The fuel consumption f_c is used to compare the different parameter configurations. In addition, the allowed temperature range of the battery is defined by 20 °C - 30 °C.

parameter	internal resistance function	coefficient of performance COP	fuel consumption f_c
Braunschweig	const.	2	6.390 lit.
bus	const.	3	6.390 lit.
cycle	$f(\vartheta_{Bat})$	2	6.377 lit.
	$f(\vartheta_{Bat})$	3	6.377 lit.
Manhattan	const.	2	2.419 lit.
bus	const.	3	2.419 lit.
cycle	$f(\vartheta_{Bat})$	2	2.415 lit.
	$f(\vartheta_{Bat})$	3	2.415 lit.
Orange County	const.	2	6.285 lit.
bus	const.	3	6.285 lit.
cycle	$f(\vartheta_{Bat})$	2	6.263 lit.
	$f(\vartheta_{Bat})$	3	6.263 lit.

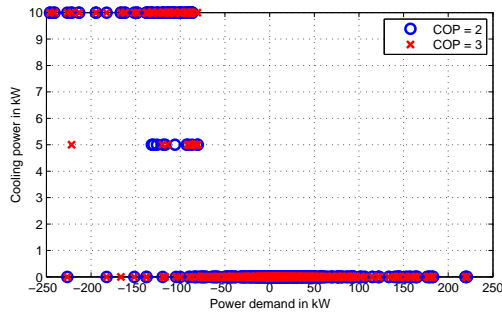
This section presented a methodology for calculating optimal operating strategies with thermal limits considered. For this purpose, the battery temperature ϑ_{BAT} was included into the optimization problem. By means of a parameter study, the influence of different driving cycles, battery resistance models and coefficients of performance COP were evaluated. Although the differences are relatively small in case of the hybrid electric bus used in this work, the obtained results can be important for operating strategies of pure electric vehicle concepts. In that case, the energy consumption e_c due to the cooling or heating of components can significantly influence the vehicle range.



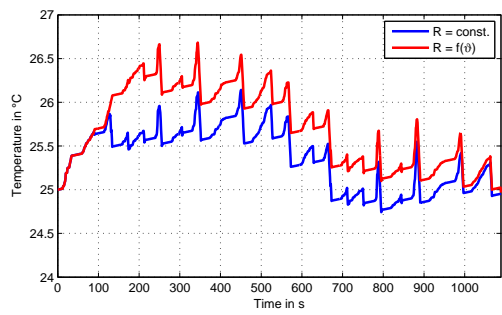
(a) Cooling power P_{COOL} over power demand P_{DEM} for different coefficients of performance COPs and the Braunschweig city driving cycle.



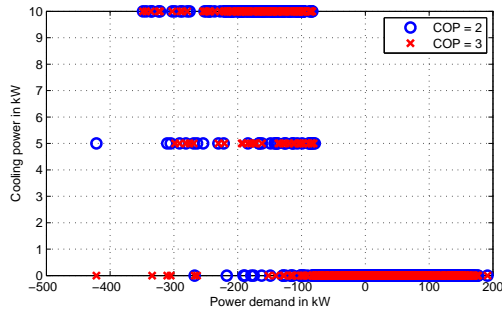
(b) Battery temperature ϑ_{BAT} over time for different internal resistance models and the Braunschweig city driving cycle.



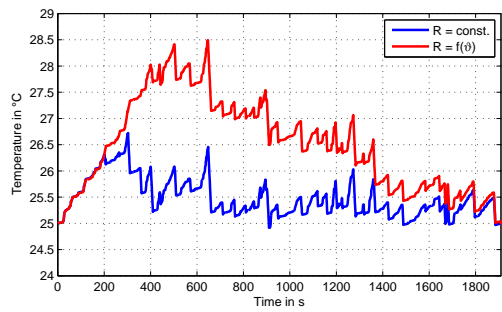
(c) Cooling power P_{COOL} over power demand P_{DEM} for different coefficients of performance COPs and the Manhattan bus cycle.



(d) Battery temperature ϑ_{BAT} over time for different internal resistance models and the Manhattan bus cycle.



(e) Cooling power P_{COOL} over power demand P_{DEM} for different coefficients of performance COPs and the Orange County bus cycle.



(f) Battery temperature ϑ_{BAT} over time for different internal resistance models and the Orange County bus cycle.

Figure 6.27.: The left column evaluates the cooling power P_{COOL} depending on the power demand P_{DEM} as well as different coefficients of performance COP and driving cycles. The relations show that the battery cooling is only activated if high recuperation power is available. The right column shows the battery temperature ϑ_{BAT} over time for constant and temperature-dependent resistance models and different driving cycles. In case of the latter model, the battery temperature ϑ_{BAT} tends to higher values. As the battery resistance R_{BAT} as well as the power loss $P_{LOSS,BAT}$ decrease for higher battery temperatures ϑ_{BAT} , an improved efficiency η in terms of charging and discharging is achieved but battery aging also increases.

6.6. Operating Strategies for the Engine-Generator Unit

In the previous sections, the start and stop operations of the engine are not considered in the optimization problem. Thus, the calculated operating strategies may contain frequent engine starts, which leads to negative effects in terms of component life spans as well as driver comfort. In order to reduce the number of engine starts N_{START} , different approaches can be taken into account. The work of [1], for example, presents an energy-based approach to penalize engine starts. The underlying idea of this method is based on the assumption that the electrical energy used to start the engine must be compensated later by means of an additional fuel consumption f_c . This relation is valid for mild and full hybrid vehicles since the battery cannot be externally charged. The energy-based approach uses the DP algorithm to calculate the global optimum. In addition to the state of charge SOC, the state space \mathcal{X} is expanded by means of a binary variable to define the states "engine on" and "engine off". The transition between these engine states is parted into two sections: Firstly, only the EM provides a constant torque to start the engine. Secondly, the engine delivers a constant torque and the EM is used to compensate the difference between the torque demand and engine torque. In order to determine the additional fuel consumption due to the start of the engine, further characteristics such as engine inertia, brake torque of the engine as well as the maximum torque of the EM are considered.

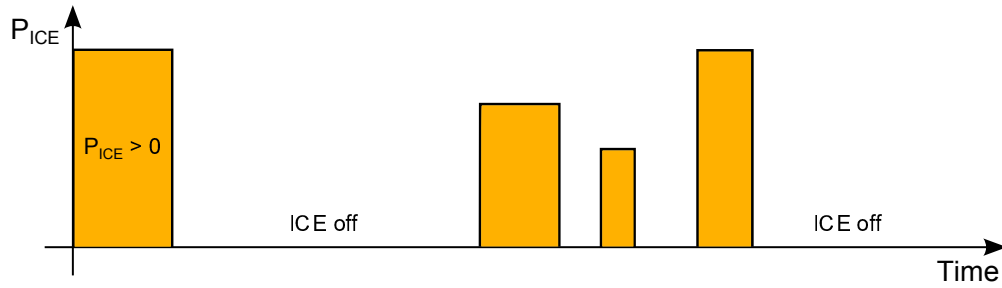
As an alternative to the previously described energy-based approach, this section presents a time-based approach in order to reduce the number of engine starts N_{START} . The main difference of both methods lies in the number of parameters. Whereas the former needs additional component parameters of engine and EM, the latter only uses one optimization parameter which is denoted as minimum idle time $t_{idle,min}$. In the following, the time-based approach is described in detail.

6.6.1. Methodology

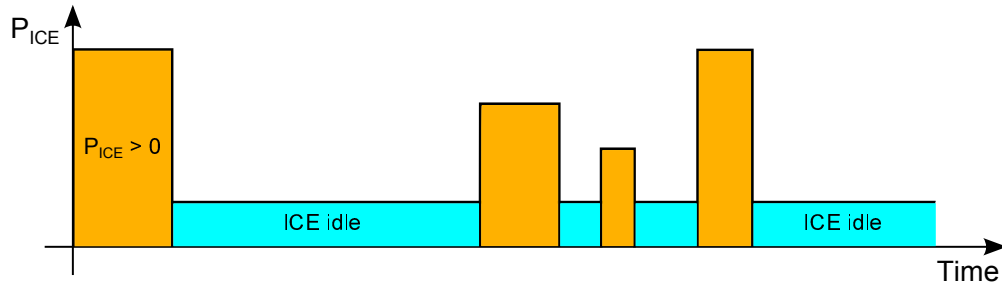
Before focusing on the time-based approach, two limits in terms of an operating strategy for the engine can be determined:

- 1.) The engine starts are not considered:
The engine is deactivated if its power demand is smaller than zero. Obviously, the fuel consumption f_c of the deactivated engine is zero. This approach leads to a maximum number of engine starts N_{START} in combination with a minimum fuel consumption f_c .
- 2.) The engine always remains in the idle mode:
The engine is idling if its power demand is smaller than zero. Thus, the minimum number of engine starts N_{START} as well as the maximum fuel consumption f_c is obtained.

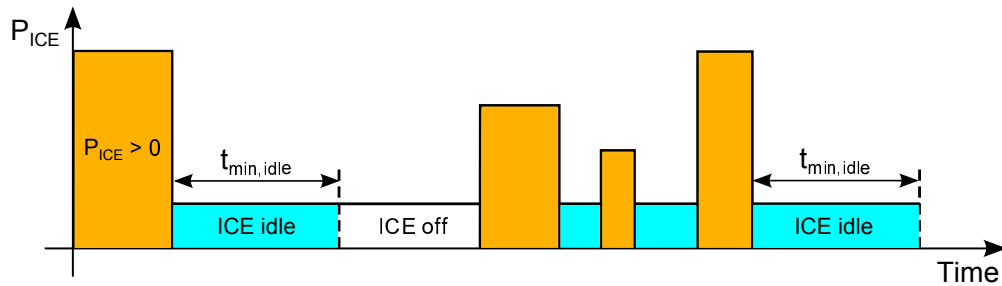
The proposed time-based approach provides solutions which lie between these two extremal limits. The minimum idle time $t_{idle,min}$ depicts the optimization parameter and weights the number of engine starts N_{START} . If the time span between two requested engine power demands is lower than a given minimum idle time $t_{idle,min}$, then the engine remains in the idle mode. The illustrations of Figures 6.28(a) and 6.28(b) graphically describe the extremal cases for given power demands of the engine. In contrast, Figure 6.28(c) depicts the proposed time-based method using a defined minimum idle time $t_{idle,min}$.



(a) Approach with a deactivated engine. If the required engine power P_{ICE} is lower than zero, then the engine is deactivated.



(b) Approach with an idling engine. If the required engine power P_{ICE} is lower than zero, then the engine idles.



(c) Approach with minimum idle time $t_{idle,min}$. If the required engine power P_{ICE} is lower than zero, then the engine either idles or is deactivated depending on the minimum idle time $t_{idle,min}$.

Figure 6.28.: Approaches to consider start-stop operations of the engine.

The optimal operating strategy with a considered minimum idle time $t_{idle,min}$ is calculated by means of the DP algorithm. In the previous Sections 6.1 - 6.4, the state of charge SOC represents the only state variable x . In order to integrate the state of the engine as well as the minimum idle time $t_{idle,min}$, the state space \mathcal{X} needs to be expanded. For this purpose, another state variable called x_{ice} is introduced. The length of x_{ice} is variable and depends on the defined minimum idle time $t_{idle,min}$. If the idle time t_{idle} is neglected, then only a binary variable ("engine on" and "engine off") remains. As the discretization of the velocity profile is specified by 1 s, the same interval is used for the state variable x_{ice} .

Table 6.16 summarizes the expansions of the dynamic program and describes the transitions between the states of the state variable x_{ice} for a minimum idle time $t_{idle,min} > 2$. The table is also valid for lower idle times t_{idle} , but the numbers of states and transitions need to be decreased accordingly.

Table 6.16.: Transitions between the states of the state variable x_{ice} . The table describes the costs as well as the next state $x_{ice,k+1}$ for a given state $x_{ice,k}$ and required engine power P_{ICE} . The table is valid for minimum idle times $t_{idle,min} > 2$. If lower times are required, then the number of states and corresponding transitions can be reduced.

$x_{ice,k}$	condition	$x_{ice,k+1}$	costs
$t_{idle,0}$	$P_{ICE} > 0$	$t_{idle,1}$	$\dot{m}_f(P_{ICE})$
$t_{idle,0}$	$P_{ICE} \leq 0$	$t_{idle,0}$	0
$t_{idle,1}$	$P_{ICE} > 0$	$t_{idle,1}$	$\dot{m}_f(P_{ICE})$
$t_{idle,1}$	$P_{ICE} \leq 0$	$t_{idle,2}$	$\dot{m}_f(idle)$
$t_{idle,2}$	$P_{ICE} > 0$	$t_{idle,1}$	$\dot{m}_f(P_{ICE})$
$t_{idle,2}$	$P_{ICE} \leq 0$	$t_{idle,3}$	$\dot{m}_f(idle)$
...
$t_{idle,N}$	$P_{ICE} > 0$	$t_{idle,1}$	$\dot{m}_f(P_{ICE})$
$t_{idle,N}$	$P_{ICE} \leq 0$	$t_{idle,0}$	0

To summarize, the following optimization problem is solved for variable idle times t_{idle} :

$$\begin{aligned}
& \min_{u_k \in \mathcal{U}_k} \sum_{k=0}^{N-1} \dot{m}_f(u_k, x_k, x_{ice,k}, w_k) \cdot \Delta t \\
& \text{s.t.} \\
& x_{k+1} = \frac{u_k \cdot \Delta t}{C_{BAT} \cdot 3600} + x_k \\
& x_{ice,k+1} = f(x_{ice,k}, P_{ICE}) \\
& 0 \leq x_k \leq 1 \\
& 0 \leq x_{ice} \leq t_{idle} \\
& -120 \leq u_k \leq 400 \\
& x_0 = 0.85 \\
& x_f = 0.85 \\
& x_{ice,0} = 0 \\
& x_{ice,f} = 0 \\
& x_k \in \mathcal{X}_k \\
& x_{ice,k} \in \mathcal{X}_{ice,k} \\
& u_k \in \mathcal{U}_k
\end{aligned}$$

where the battery current I_{BAT} is used as control variable u_k , the battery's state of charge SOC as state variable x_k , the "state of the engine" as state variable $x_{ice,k}$ and the power demand P_{DEM} as disturbance w_k . In addition, limits of the control and state variables as well as a sampling time Δt of 1 s are considered.

6.6.2. Results

In the following, the presented time-based approach is demonstrated by means of simulations. The simulation model contains the reference configuration as shown in Section 6.1. Since the model uses a series hybrid topology, the start-stop operations of the EGU are included into the optimization problem. In order to calculate the global optimum, the driving cycles must be known in advance. For this purpose, the velocity profiles of Appendix D are used.

Figure 6.29 depicts the number of engine starts N_{START} depending on the minimum idle time $t_{idle,min}$ for three driving cycles. The results show that a lower minimum idling time $t_{idle,min}$ leads to a higher number of engine starts N_{START} . As the EGU is started at least once per driving cycle, a lower threshold is given for long minimum idle times $t_{idle,min}$.

Figure 6.30 shows the fuel consumption f_c depending on the minimum idle time $t_{idle,min}$ for three driving cycles. It can be seen that the fuel consumption f_c increases with longer minimum idle times $t_{idle,min}$ and vice versa.

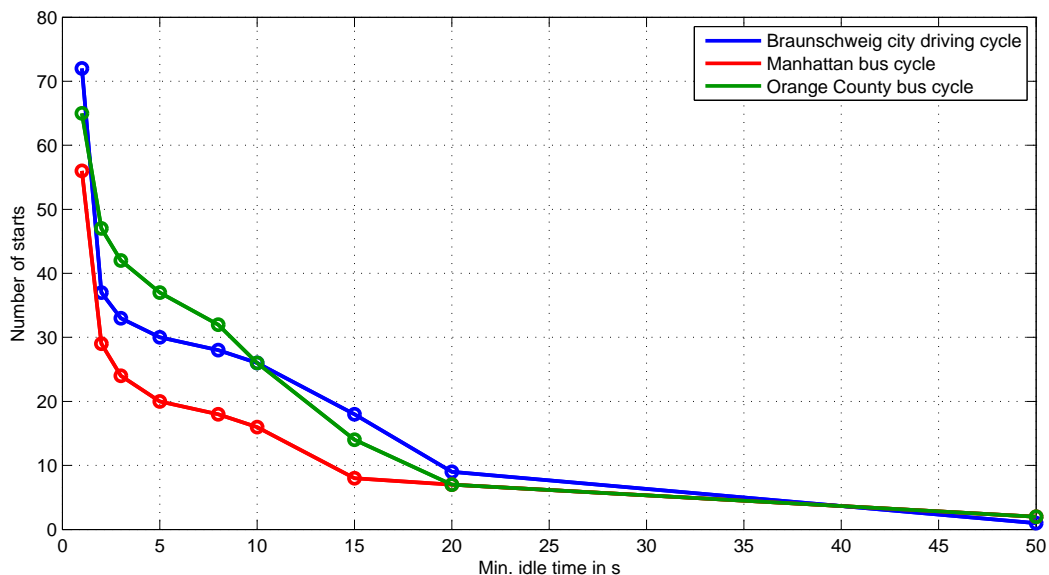


Figure 6.29.: Number of engine starts N_{START} depending on the minimum idling time $t_{idle,min}$. A lower minimum idle time $t_{idle,min}$ leads to a higher number of engine starts N_{START} and vice versa.

On the basis of simulation results, the influence of several minimum idle times $t_{idle,min}$ is evaluated. As minimizing the number of engine starts N_{START} and minimizing the fuel consumption f_c depict contrary objectives, the optimal value for the minimum idle time $t_{idle,min}$ mainly depends on the application. If the focus is put on an improved driver comfort or longer component life spans, then higher values for the minimum idle time $t_{idle,min}$ need to be taken into account.

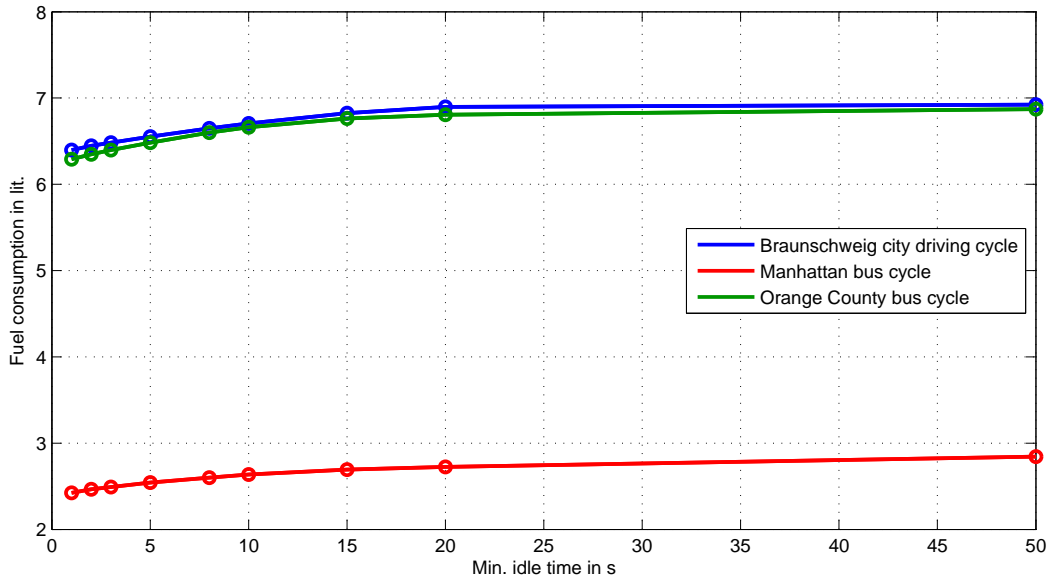


Figure 6.30.: Fuel consumption f_c depending on the minimum idling time $t_{idle,min}$. A longer minimum idle time $t_{idle,min}$ leads to an increased fuel consumption f_c .

6.7. Summary

In this chapter, novel methodologies in terms of optimal component sizing as well as operating strategies were presented for applications in the field of HEVs. These methodologies were described on the basis of stand-alone approaches which can also be combined in order to obtain further optimization goals. A model of a series hybrid bus was used for the demonstration but the generality of the proposed approaches also allows to consider other vehicle types and topologies. In order to calculate globally optimal results, the mathematical method of IDP was applied.

In the first section, initial parameters of the dynamic program such as discretizations of state variables Δx and control variables Δu were defined. For this purpose, a reference configuration of the bus including a battery capacity C_{BAT} of 40 Ah and a maximum EGU power $P_{EGU,max}$ of 160 kW was used. In order to determine initial values of the state of charge SOC_0 , the driving cycles were periodically continued until a convergence of the state of charge trajectory was obtained. As the hybrid bus cannot be charged from the grid, the initial state of charge SOC_0 and the final state of charge SOC_f need to be equal and were defined by 85%. In terms of a meaningful trade-off between accuracy and calculation time, the IDP algorithm was applied containing an initial state of charge discretization ΔSOC of 10^{-3} and a battery current discretization ΔI of 0.5 A. Furthermore, the number of iterations and the grid reduction factor were defined by five and 0.5, respectively. All the parameters determined within the first section were used in the following simulation studies.

The second section described the optimal sizing of the two energy sources battery and EGU. By means of an iterative approach, the minimum power of the EGU $P_{EGU,min}$ was determined for given battery capacities C_{BAT} leading to a set of optimal combinations of traction energy sources. Furthermore, the minimum fuel consumption f_c was calculated for this set of optimal energy sources. Compared to a very low battery capacity C_{BAT} , the results show a reduction of fuel consumption f_c of approximately 30% for a high battery capacity C_{BAT} .

On the basis of the optimal set of traction energy sources combined with additional parameters like initial costs ($c_{comp,egu}$, $c_{comp,bat}$) or fuel consumption f_c , the optimal sizes of traction energy sources can be finally determined.

The third section presented an approach for the optimal scaling of EMs for HEVs. For the demonstration, the optimal continuous S1 torque M_{cont} as well as the optimal maximum S2 torque M_{max} of the electric traction motors were optimized for given driving cycles. The methodology considers the overloading of the EM as well as voltage-dependencies due to voltage swings of the vehicle's electrical system. The results show that the voltage swings of the vehicle's electrical system do not affect the optimization if a battery is used as energy storage. In addition, a second gear was included in the drivetrain leading to a further degree of freedom. By means of this expansion, the optimal continuous torque M_{cont} can be reduced by up to 25% on the basis of the chosen driving cycles. In a further step, the battery was replaced by a supercap. The simulation results depict that significantly higher values of the maximum torque M_{max} are required due to the voltage swings of the supercap.

In the fourth section, cost-optimal operating strategies for HEVs were calculated. For this purpose, not only the fuel consumption f_c but also battery aging effects as well as brake pad wear were included in the optimization problem. Firstly, the operating costs c_{op} are described by means of costs due to fuel consumption f_c as well as costs due to cyclic battery aging. In contrast to linear aging models, the use of a non-linear aging model based on data sheets and related work leads to significantly lower cyclic aging. The methodology allows to determine the optimal operating strategy leading to minimum operating costs c_{op} . In a further step, calendric aging effects were included in order to estimate the life cycle costs c_{life} of HEVs. The results show that finding the optimal battery capacity C_{BAT} is mainly influenced by the operating hours h_{op} of the bus. Furthermore, the braking costs due to brake pad wear were included into the optimization problem. Based on the mechanical brake model used, it turned out that costs for the exchange of mechanical brakes are relatively small compared to the total life cycle costs c_{life} .

In the fifth section, an approach for optimal operating strategies containing thermal effects was described. In order to demonstrate the approach, not only the fuel consumption f_c but also the thermal behavior of the battery was considered in the optimization process. The minimum fuel consumption f_c was calculated for different coefficients of performance COP and models of the battery's internal resistance R_{BAT} . Although the differences between the results are very small in case of the hybrid bus, the proposed methodology may be important for pure electric vehicle concepts.

The sixth section presented a methodology which controls the number of start-stop operations N_{START} of the engine by means of a time-based approach. For this purpose, the dynamic program was expanded by means of a further state variable x_{ice} in order to consider the idling time t_{idle} of the engine. The methodology allows to determine the optimal value of the minimum idling time $t_{idle,min}$ leading to a compromise of the contrary items fuel consumption f_c and driver comfort.

7. Summary and Conclusion

The main goal of this thesis has been the development of novel methodologies in order to optimize the component sizing as well as the operating strategies of hybrid electric vehicles (HEVs).

Starting from the basics of this vehicle type in Chapter 2, the state-of-the-art of operating strategies for HEVs was described in Chapter 3. It turned out that only the mathematical method of dynamic programming (DP) fulfills the requirements of the optimization problems defined within this thesis. Therefore, the following Chapter 4 provided a more detailed introduction to DP and outlined the different variants as well as their pros and cons. In addition, the modifications of the DP algorithm used in this work were described. The devised approaches of this thesis were demonstrated by means of a series hybrid bus model. In Chapter 5, the component models of the bus were presented with respect to their characteristics and parameters.

Chapter 6 represents the central part of this thesis and describes the methodologies developed. After the definition of a reference simulation model and determining the specific parameters of the dynamic program in Section 6.1, the Sections 6.2 and 6.3 deal with the optimal sizing of components. The remaining Sections 6.4 - 6.6 provide novel approaches in terms of optimal operating strategies of HEVs. In Section 6.2, a methodology for calculating optimal sizes of both energy sources, engine-generator unit (EGU) and battery, was described. For this purpose, the scaling of the energy sources was performed based on linear approaches. As the results depict Pareto fronts, further parameters are needed to find the optimal configuration of energy sources. These parameters include, for example, the initial component costs or the fuel costs. Another methodology described in Section 6.3 deals with the optimal sizing of electric motors (EMs). The demonstration was carried out by means of the electric traction motors of the hybrid bus. The methodology allows to calculate the optimal EM for a given driving cycle profile in terms of the S1 and S2 operating modes. The optimization considers overloading of the EM as well as voltage dependencies due to the voltage swings of the vehicle's electrical system. By means of simulation results, it can be concluded that the sizing of EMs depends on the chosen type of electrical energy storage. Whereas voltage swings of the vehicle's electrical system can be neglected for batteries, these effects need to be considered in case of supercaps. Section 6.4 describes methodologies to calculate cost-optimal operating strategies in order to minimize operating as well as life cycle costs. Beside the fuel costs, the first part considers costs due to cyclic battery aging. In contrast to constant charge throughput models, a non-linear charge throughput model on the basis of measurement data was applied leading to significantly lower aging. By means of a combination of DP and the rainflow counting algorithm, the ratio of fuel costs and costs due to cyclic battery aging was calculated. In a further step of the first part, calendric aging effects were included for determining life cycle costs of HEVs. The second part considers costs due to brake pad wear in the optimization process on the basis of a linear brake wear model. The methodology developed allows to determine the cost-optimal operating strategies for variable parameters such as fuel and battery prices and battery capacities. Based on simulations containing current as well as future price levels, it can be concluded that the operating as well as the life

cycle costs are mainly influenced by the fuel costs. In Section 6.5, an approach for optimal operating strategies including battery temperatures was described. For this purpose, not only the fuel consumption but also the thermal behavior of the battery was integrated into the optimization problem. The results based on the bus model show that the additional power demand through the cooling of the battery is relatively small. However, the approach can be used for optimizing the operating strategies of pure electric vehicles. In that case, the energy consumption of auxiliaries is probably significant in terms of the vehicle range. Section 6.6 provides a methodology which allows to control the number of start-stop operations of the internal combustion engine (ICE). In contrast to related work, a time-based approach was taken into account which considers a minimum idling time of the engine. On the basis of this approach, several operating strategies depending on minimum idling times are calculated. The selection of the optimal operating strategy is mainly influenced by the desired application. In terms of a lower fuel consumption, low values of the minimum idling time should be chosen. In contrast, higher values of this parameter lead to improved driver comfort and NVH behavior.

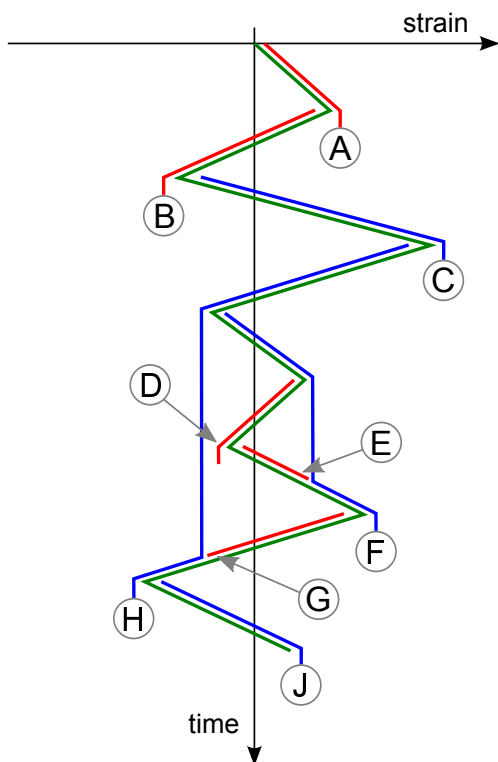
Outlook

In this thesis, novel approaches in terms of optimal energy management for HEVs were demonstrated with the help of a series hybrid bus model. As the methodologies developed do not depend on the hybrid topology, other types of HEVs can be used in future work. In terms of cost-optimal strategies, further components which are controlled by means of the operating strategy can be taken into account. As an example, costs due to the wear of components like clutches, ICE or EM would lead to better estimations of operating and life cycle costs.

Other improvements can be provided with respect to the use of more advanced component models, but limits due to the optimization framework need to be taken into account. Although DP can handle high model complexities, the number of state variables is restricted in practice due to the "curse of dimensionality". Further work may consider the scaling of components like EGU, battery or EM in more detail. For this purpose, the approaches of this thesis need to be replaced by more detailed functions. As stated above, the methodologies of this work use DP for calculating the globally optimal solution. Instead of DP, faster algorithms such as quadratic programming or Pontryagin's maximum principle can be applied but in that case, component models as well as the optimization problems need to be simplified. This thesis has focused on optimal operating strategies which on the one hand provide benchmarks but on the other hand can only be applied off-line. Since the development of causal operating strategies was not the goal of this thesis, future work may concentrate on this task. For this purpose, the globally optimal results can be used in order to derive and improve rules for causal operating strategies. As simulation studies were performed within this work, the validation of the proposed methodologies by means of measurement data can be taken into account in the future.

A. Rainflow Counting Algorithm

The rainflow counting algorithm is a well-known method in the field of mechanical stress analysis. It belongs to the class of cycle-counting algorithms and was originally introduced by [65]. The principle of the algorithm is that a strain profile can be converted into cycles with corresponding amplitudes.



Example of a load profile (green line) for the demonstration of the rainflow counting algorithm. The profile is converted into nine half cycles with corresponding amplitudes A-J.

The left figure depicts the principle of the rainflow counting algorithm and shows a given load profile containing the strain over time. The algorithm only uses the extremal values and omits all remaining points. In the next step, water droplets are generated at each extremum. Like the behavior of a pagoda roof during rain, these droplets flow to the next extremum and fall down. Afterwards, the following two scenarios occur:

- If two droplets merge, then only the droplet with the bigger amplitude remains. The other droplet is removed and the corresponding amplitude is stored (red lines),
- If the droplet falls on the ground, the corresponding amplitude is stored (blue lines).

In the evaluation step, the calculated amplitudes of the water droplets can be divided into half and full cycles. By means of stress or fatigue models, these cycles can be finally converted into an equivalent damage.

B. Mathematical Derivations

B.1. Hamilton-Jacobi-Bellman Equation

In the following, a brief derivation of the Hamilton-Jacobi-Bellman Equation (HJBE) is provided as shown in [49].

The performance index

$$J(x_0, u) = \int_{t_0}^{t_f} L(\tau, x, u) d\tau + L_f(t_f, x(t_f)) \quad (\text{B.1})$$

is to be minimized by means of an optimal control variable u^* .

In a further step, the performance index $J(\cdot)$ of Equation B.1 is expanded in order to describe the optimal cost-to-go $\mathcal{J}(\cdot)$:

$$\mathcal{J}(t, x_t) = \min_{u([t, t_f]) \in \mathcal{U}} \left\{ \int_t^{t_f} L(\tau, x, u) d\tau + L_f(t_f, x(t_f)) \right\}. \quad (\text{B.2})$$

By subdividing the interval, we obtain

$$\mathcal{J}(t, x_t) = \min_{u([t, t_f]) \in \mathcal{U}} \left\{ \int_t^{t+\Delta t} L(\tau, x, u) d\tau + \int_{t+\Delta t}^{t_f} L(\tau, x, u) d\tau + L_f(t_f, x(t_f)) \right\}. \quad (\text{B.3})$$

The principle of optimality requires that

$$\mathcal{J}(t, x_t) = \min_{u([t, t+\Delta t]) \in \mathcal{U}} \left\{ \int_t^{t+\Delta t} L(\tau, x, u) d\tau + \mathcal{J}(t + \Delta t, x_t + \Delta x_t) \right\}. \quad (\text{B.4})$$

Rewriting Equation B.4 leads to

$$0 = \min_{u([t, t+\Delta t]) \in \mathcal{U}} \left\{ \int_t^{t+\Delta t} L(\tau, x, u) d\tau + \mathcal{J}(t + \Delta t, x_t + \Delta x_t) - \mathcal{J}(t, x_t) \right\}. \quad (\text{B.5})$$

Taking the limit as $\Delta t \rightarrow 0$ gives

$$0 = \lim_{\Delta t \rightarrow 0} \frac{1}{\Delta t} \min_{u([t, t+\Delta t]) \in \mathcal{U}} \left\{ \int_t^{t+\Delta t} L(\tau, x, u) d\tau + \mathcal{J}(t + \Delta t, x_t + \Delta x_t) - \mathcal{J}(t, x_t) \right\}. \quad (\text{B.6})$$

Two different notations are considered in terms of the state variable:

- x can be seen as a state function over the integration interval,
- x_t represents a vector of states.

In the following equations, the difference between these notations vanishes and consequently, the notation x is used to describe the state variable.

$$0 = \min_{u \in \mathcal{U}} \left\{ L(t, x, u) + \frac{d}{dt} \mathcal{J}(t, x) \right\}. \quad (\text{B.7})$$

$$0 = \min_{u \in \mathcal{U}} \left\{ L(t, x, u) + \frac{\partial}{\partial t} \mathcal{J}(t, x) + \frac{\partial}{\partial x} \mathcal{J}(t, x) \cdot \dot{x} \right\}. \quad (\text{B.8})$$

Finally, the HJBE is obtained by means of

$$0 = \frac{\partial}{\partial t} \mathcal{J}(t, x) + \min_{u \in \mathcal{U}} \left\{ L(t, x, u) + \frac{\partial}{\partial x} \mathcal{J}(t, x) \cdot f(t, x, u) \right\}. \quad (\text{B.9})$$

B.2. Pontryagin's Maximum Principle

This section provides a brief introduction to Pontryagin's maximum principle (PMP) based on [49].

Firstly, the performance index $J(\cdot)$ is expanded by means of the system dynamics $f(\cdot)$ leading to the augmented functional

$$J(x_0, u) = \int_{t_0}^{t_f} \left(L(t, x, u) + \lambda^T \cdot (f(t, x, u) - \dot{x}) \right) dt. \quad (\text{B.10})$$

The Hamiltonian function defined in Equation 3.17 is used to obtain

$$J(x_0, u) = \int_{t_0}^{t_f} \left(H(t, x, u, \lambda) - \lambda^T \dot{x} \right) dt. \quad (\text{B.11})$$

In the next step, the variation of the performance index δJ can be described by means of

$$\delta J = \int_{t_0}^{t_f} \left\{ \left[\frac{\partial H}{\partial x} + \dot{\lambda} \right]^T \cdot \delta x + \left[\frac{\partial H}{\partial u} \right]^T \cdot \delta u + \left[\frac{\partial H}{\partial \lambda} - \dot{x} \right]^T \cdot \delta \lambda \right\} dt. \quad (\text{B.12})$$

By means of Equation B.12 necessary conditions in terms of the state x and co-state λ can be derived:

$$\dot{\lambda}^*(t) = -\frac{\partial H}{\partial x}(t, x^*(t), u^*(t), \lambda^*(t)) \quad (\text{B.13})$$

$$x^*(t) = \frac{\partial H}{\partial \lambda}(t, x^*(t), u^*(t), \lambda^*(t)) \quad (\text{B.14})$$

In order to determine the optimal control variable u^* , a further condition needs to be taken into account. The variational approach uses the condition

$$\frac{\partial H}{\partial u}(t, x^*(t), u^*(t), \lambda^*(t)) = 0, \quad (\text{B.15})$$

which can only be applied for unconstrained control variables.

In contrast, the PMP uses another approach which allows to consider constrained control variables. Thereby, the condition

$$H(t, x^*(t), u^*(t), \lambda^*(t)) \leq H(t, x^*(t), u, \lambda^*(t)) \quad (\text{B.16})$$

must hold.

B.3. Relation between Dynamic Programming and the Hamilton-Jacobi-Bellman Equation

This section describes the relation between DP and the HJBE and is based on [8].

Since DP is a numerical method, the time horizon $[0, T]$ is divided into N pieces which leads to a discretization interval of

$$\Delta = \frac{T}{N} \quad (\text{B.17})$$

Furthermore, the optimal cost-to-go function of the continuous-time problem $\mathcal{J}(t, x)$ is approximated by $\tilde{\mathcal{J}}(t, x)$.

Now, the DP equations are represented by

$$\tilde{\mathcal{J}}(N \cdot \Delta, x) = L_N(N \cdot \Delta, x), \quad (\text{B.18})$$

and

$$\tilde{\mathcal{J}}(k \cdot \Delta, x) = \min_{u \in \mathcal{U}} \left[L(x, u) \cdot \Delta + \tilde{\mathcal{J}}((k+1) \cdot \Delta, x + f(x, u) \cdot \Delta) \right], \quad k = 0, \dots, N-1. \quad (\text{B.19})$$

Assuming that $\tilde{\mathcal{J}}(t, x)$ has the required differentiability properties, a Taylor series can be defined around $(k \cdot \Delta, x)$. A first order approximation leads to

$$\begin{aligned} \tilde{\mathcal{J}}((k+1) \cdot \Delta, x + f(x, u) \cdot \Delta) &= \tilde{\mathcal{J}}(k \cdot \Delta, x) + \\ &\frac{\partial}{\partial t} \tilde{\mathcal{J}}(k \cdot \Delta, x) \cdot \Delta + \left[\frac{\partial}{\partial x} \tilde{\mathcal{J}}(k \cdot \Delta, x) \right]^T \cdot f(x, u) \cdot \Delta. \end{aligned} \quad (\text{B.20})$$

With the help of Equation B.20, the DP Equation B.19 can be rewritten in

$$\begin{aligned} \tilde{\mathcal{J}}(k \cdot \Delta, x) &= \min_{u \in \mathcal{U}} \left[L(x, u) \cdot \Delta + \tilde{\mathcal{J}}(k \cdot \Delta, x) + \right. \\ &\left. \frac{\partial}{\partial t} \tilde{\mathcal{J}}(k \cdot \Delta, x) \cdot \Delta + \left[\frac{\partial}{\partial x} \tilde{\mathcal{J}}(k \cdot \Delta, x) \right]^T \cdot f(x, u) \cdot \Delta \right]. \end{aligned} \quad (\text{B.21})$$

Cancelling $\tilde{\mathcal{J}}(k \cdot \Delta, x)$ from both sides of Equation B.21 and dividing by Δ , yields to

$$0 = \min_{u \in \mathcal{U}} \left[L(x, u) + \frac{\partial}{\partial t} \mathcal{J}(k \cdot \Delta, x) + \left[\frac{\partial}{\partial x} \mathcal{J}(k \cdot \Delta, x) \right]^T \cdot f(x, u) \right]. \quad (\text{B.22})$$

For the transition between discrete-time and continuous-time cost-to-go functions, it is assumed that

$$\lim_{k \rightarrow \infty, \Delta \rightarrow 0, k\Delta = t} \tilde{\mathcal{J}}(k \cdot \Delta, x) = \mathcal{J}(t, x), \quad \text{for all } t, x. \quad (\text{B.23})$$

By means of Equation B.23, the continuous version of Equation B.22

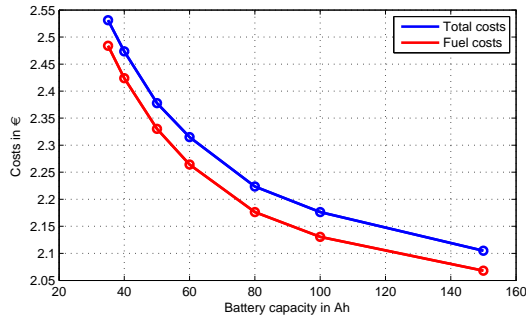
$$0 = \min_{u \in \mathcal{U}} \left[L(x, u) + \frac{\partial}{\partial t} \mathcal{J}(t, x) + \left[\frac{\partial}{\partial x} \mathcal{J}(t, x) \right]^T \cdot f(x, u) \right] \quad (\text{B.24})$$

is obtained with the boundary condition

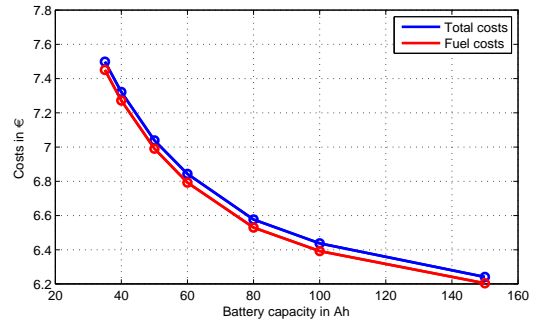
$$\mathcal{J}(T, x(T)) = L_N(N \cdot \Delta, x(N \cdot \Delta)). \quad (\text{B.25})$$

The comparison of Equations 3.16 and B.24 shows that both derivations lead to the same result. Thus, it can be concluded that DP represents a suitable method for solving the HJBE.

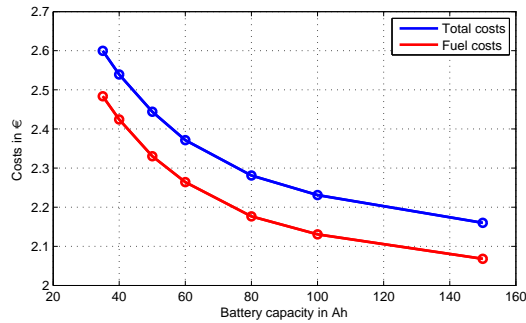
C. Simulation Results



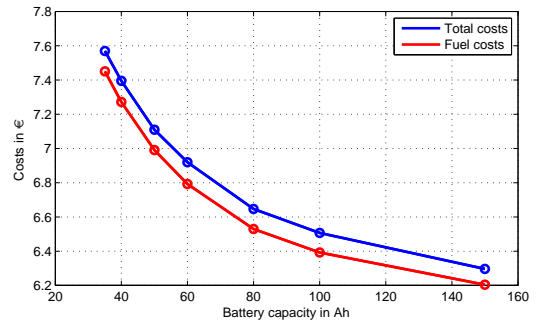
(a) Fuel costs c_{fuel} of 1 €/lit. and battery costs c_{bat} of 200 €/kWh.



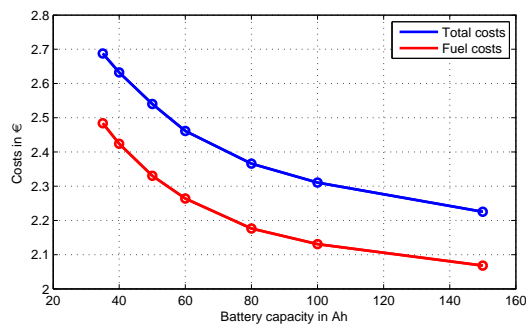
(b) Fuel costs c_{fuel} of 3 €/lit. and battery costs c_{bat} of 200 €/kWh.



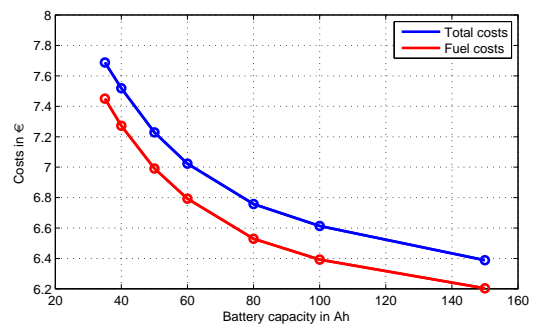
(c) Fuel costs c_{fuel} of 1 €/lit. and battery costs c_{bat} of 500 €/kWh.



(d) Fuel costs c_{fuel} of 3 €/lit. and battery costs c_{bat} of 500 €/kWh.

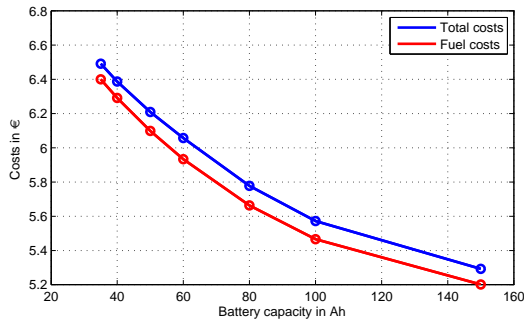


(e) Fuel costs c_{fuel} of 1 €/lit. and battery costs c_{bat} of 1000 €/kWh.

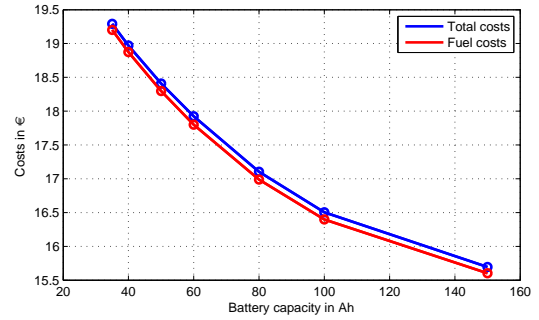


(f) Fuel costs c_{fuel} of 3 €/lit. and battery costs c_{bat} of 1000 €/kWh.

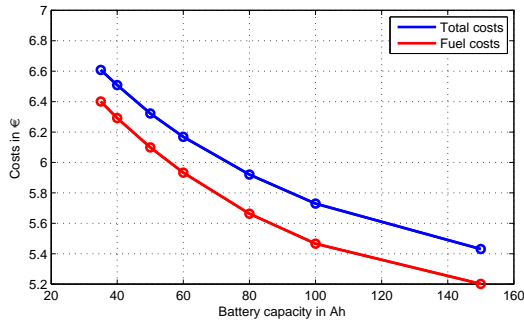
Figure C.1.: Minimum costs depending on the battery capacity C_{BAT} for different fuel costs c_{fuel} and battery costs c_{bat} for the Manhattan bus cycle.



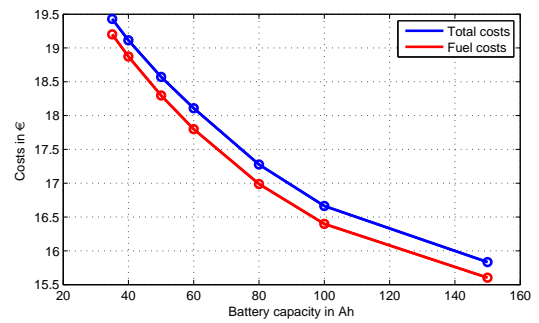
(a) Fuel costs c_{fuel} of 1 €/lit. and battery costs c_{bat} of 200 €/kWh.



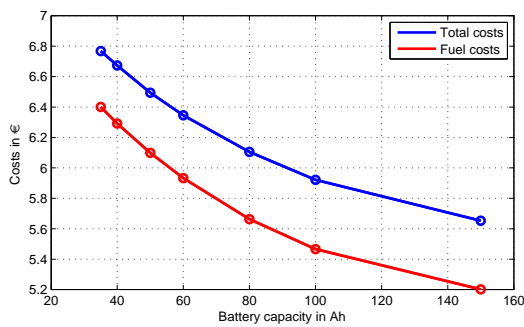
(b) Fuel costs c_{fuel} of 3 €/lit. and battery costs c_{bat} of 200 €/kWh.



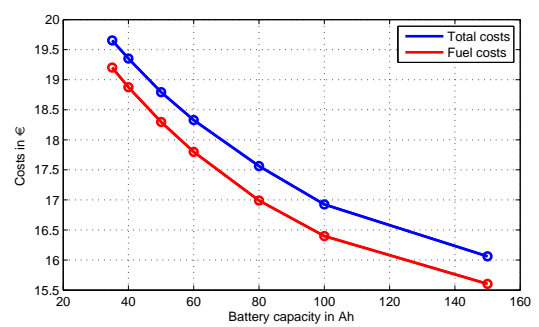
(c) Fuel costs c_{fuel} of 1 €/lit. and battery costs c_{bat} of 500 €/kWh.



(d) Fuel costs c_{fuel} of 3 €/lit. and battery costs c_{bat} of 500 €/kWh.

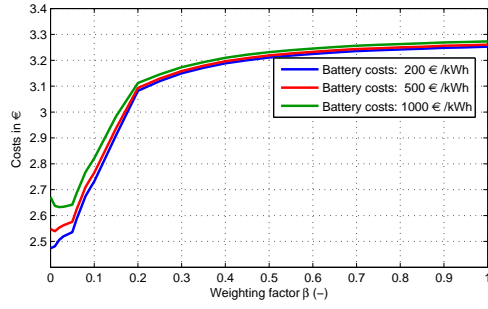
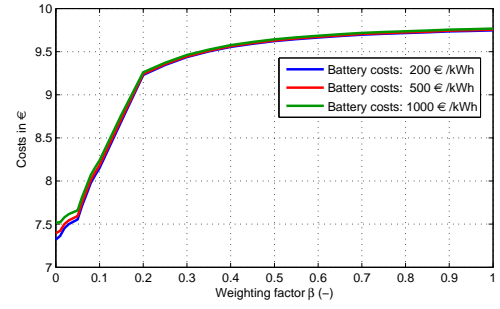
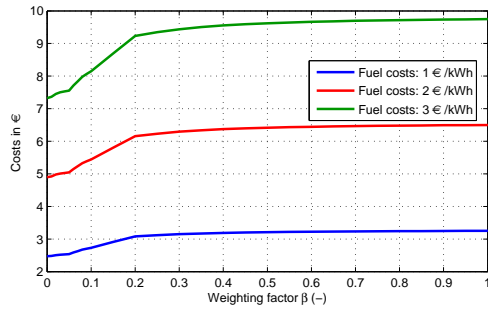
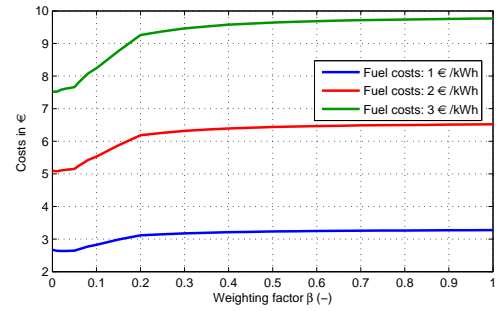


(e) Fuel costs c_{fuel} of 1 €/lit. and battery costs c_{bat} of 1000 €/kWh.

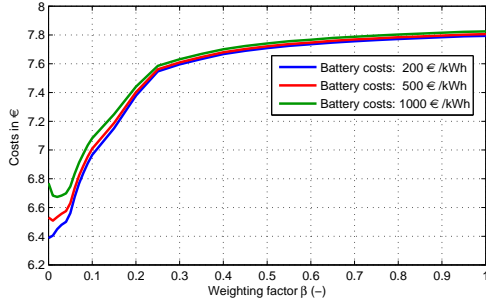
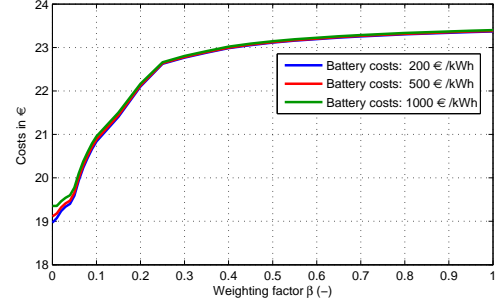
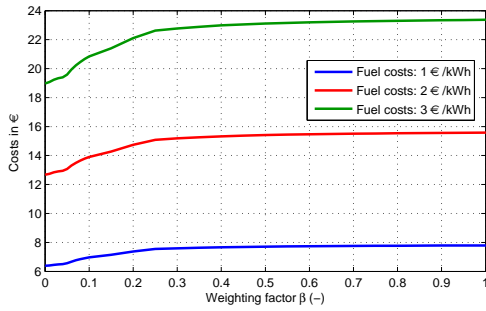
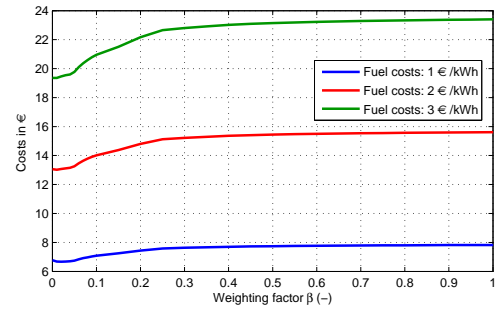


(f) Fuel costs c_{fuel} of 3 €/lit. and battery costs c_{bat} of 1000 €/kWh.

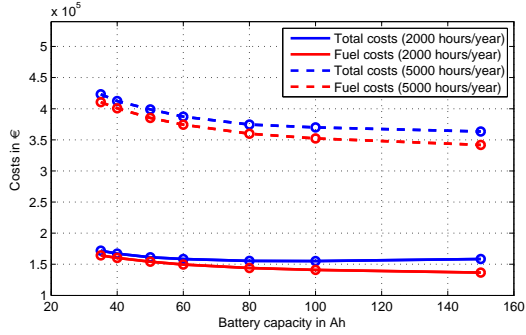
Figure C.2.: Minimum costs depending on the battery capacity C_{BAT} for different fuel costs c_{fuel} and battery costs c_{bat} for the Orange County bus cycle.

(a) Fuel costs c_{fuel} of 1 €/lit. and variable battery costs c_{bat} .(b) Fuel costs c_{fuel} of 3 €/lit. and variable battery costs c_{bat} .(c) Battery costs c_{bat} of 200 €/kWh and variable fuel costs c_{fuel} .(d) Battery costs c_{bat} of 1000 €/kWh and variable fuel costs c_{fuel} .Figure C.3.: Variable fuel costs c_{fuel} and battery costs c_{bat} over β for the Manhattan bus cycle.Table C.1.: Share of battery aging effects based on the Manhattan bus cycle, fuel costs c_{fuel} of 1 €/liter and battery costs c_{bat} of 500 €/kWh. The variable parameters are defined by the battery capacity C_{BAT} and operating hours h_{op} .

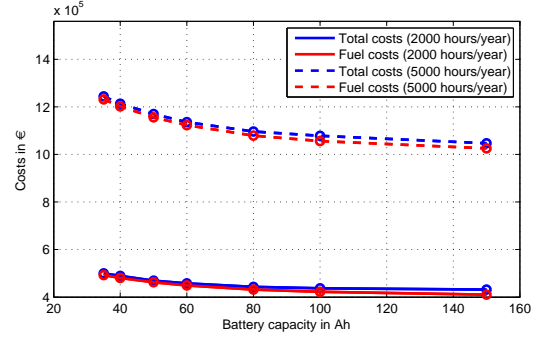
battery capacity (Ah)	operating hours (h/year)	cyclic aging (1/cycle)	calendric aging (1/cycle)	battery aging (1/cycle)	total battery aging (-)	number of batteries (-)
40	2000	$1.36 \cdot 10^{-5}$	$1.51 \cdot 10^{-5}$	$2.87 \cdot 10^{-5}$	1.90	2
40	5000	$1.72 \cdot 10^{-5}$	$6.05 \cdot 10^{-6}$	$2.33 \cdot 10^{-5}$	3.84	4
60	2000	$1.18 \cdot 10^{-5}$	$1.51 \cdot 10^{-5}$	$2.69 \cdot 10^{-5}$	1.78	2
60	5000	$1.18 \cdot 10^{-5}$	$6.05 \cdot 10^{-6}$	$1.79 \cdot 10^{-5}$	2.95	3
80	2000	$8.17 \cdot 10^{-6}$	$1.51 \cdot 10^{-5}$	$2.33 \cdot 10^{-5}$	1.54	2
80	5000	$5.89 \cdot 10^{-6}$	$6.05 \cdot 10^{-6}$	$1.19 \cdot 10^{-5}$	1.97	2
100	2000	$6.36 \cdot 10^{-6}$	$1.51 \cdot 10^{-5}$	$2.15 \cdot 10^{-5}$	1.42	2
100	5000	$4.65 \cdot 10^{-6}$	$6.05 \cdot 10^{-6}$	$1.07 \cdot 10^{-5}$	1.77	2

(a) Fuel costs c_{fuel} of 1 €/lit. and variable battery costs c_{bat} .(b) Fuel costs c_{fuel} of 3 €/lit. and variable battery costs c_{bat} .(c) Battery costs c_{bat} of 200 €/kWh and variable fuel costs c_{fuel} .(d) Battery costs c_{bat} of 1000 €/kWh and variable fuel costs c_{fuel} .Figure C.4.: Variable fuel costs c_{fuel} and battery costs c_{bat} over β for the Orange County bus cycle.Table C.2.: Share of battery aging effects based on the Orange County bus cycle, fuel costs c_{fuel} of 1 €/liter and battery costs c_{bat} of 500 €/kWh. The variable parameters are defined by the battery capacity C_{BAT} and operating hours h_{op} .

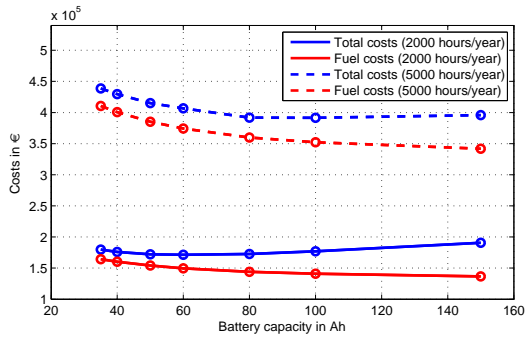
battery capacity (Ah)	operating hours (h/year)	cyclic aging (1/cycle)	calendric aging (1/cycle)	battery aging (1/cycle)	total battery aging (-)	number of batteries (-)
40	2000	$2.41 \cdot 10^{-5}$	$2.65 \cdot 10^{-5}$	$5.06 \cdot 10^{-5}$	1.91	2
40	5000	$2.72 \cdot 10^{-5}$	$1.06 \cdot 10^{-5}$	$3.78 \cdot 10^{-5}$	3.56	4
60	2000	$1.81 \cdot 10^{-5}$	$2.65 \cdot 10^{-5}$	$4.46 \cdot 10^{-5}$	1.68	2
60	5000	$1.81 \cdot 10^{-5}$	$1.06 \cdot 10^{-5}$	$2.87 \cdot 10^{-5}$	2.70	3
80	2000	$1.99 \cdot 10^{-5}$	$2.65 \cdot 10^{-5}$	$4.64 \cdot 10^{-5}$	1.75	2
80	5000	$1.99 \cdot 10^{-5}$	$1.06 \cdot 10^{-5}$	$3.05 \cdot 10^{-5}$	2.88	3
100	2000	$1.47 \cdot 10^{-5}$	$2.65 \cdot 10^{-5}$	$4.12 \cdot 10^{-5}$	1.55	2
100	5000	$1.05 \cdot 10^{-5}$	$1.06 \cdot 10^{-5}$	$2.11 \cdot 10^{-5}$	1.99	2



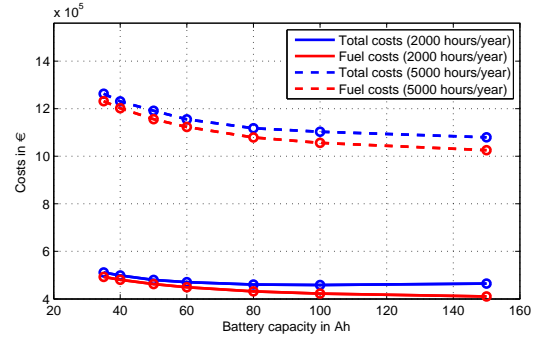
(a) Fuel costs c_{fuel} of 1 €/lit. and battery costs c_{bat} of 200 €/kWh.



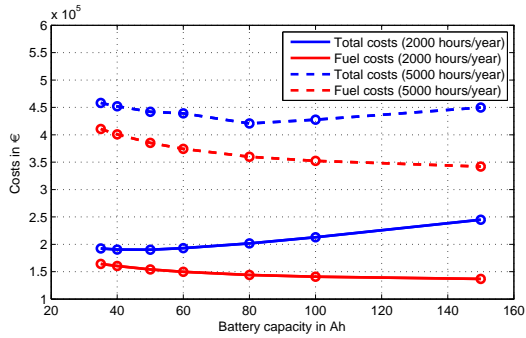
(b) Fuel costs c_{fuel} of 3 €/lit. and battery costs c_{bat} of 200 €/kWh.



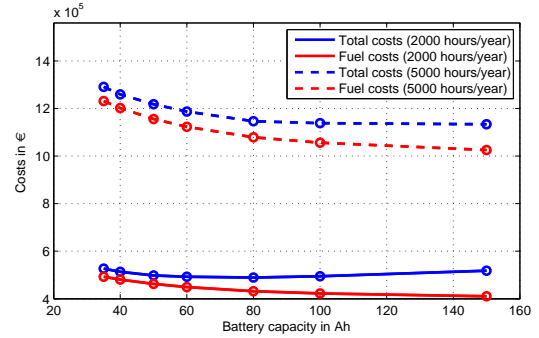
(c) Fuel costs c_{fuel} of 1 €/lit. and battery costs c_{bat} of 500 €/kWh.



(d) Fuel costs c_{fuel} of 3 €/lit. and battery costs c_{bat} of 500 €/kWh.

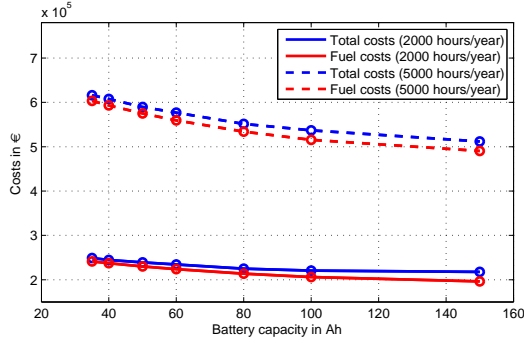


(e) Fuel costs c_{fuel} of 1 €/lit. and battery costs c_{bat} of 1000 €/kWh.

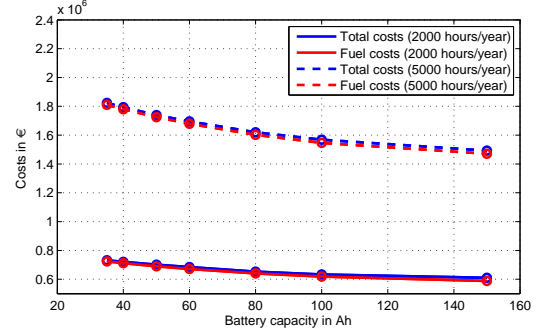


(f) Fuel costs c_{fuel} of 3 €/lit. and battery costs c_{bat} of 1000 €/kWh.

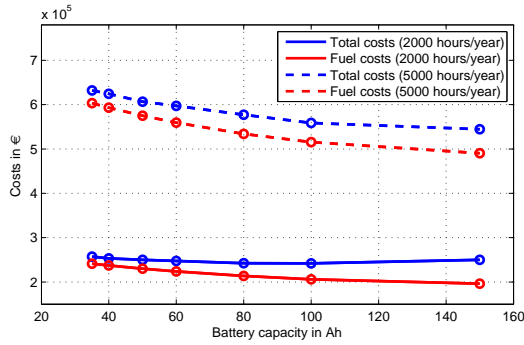
Figure C.5.: Comparison of life cycle costs c_{life} depending on battery capacity C_{BAT} and operating hours h_{op} for the Manhattan bus cycle. The optimal battery capacity C_{BAT} leading to the minimum life cycle costs c_{life} can be determined for different values of fuel costs c_{fuel} and battery costs c_{bat} .



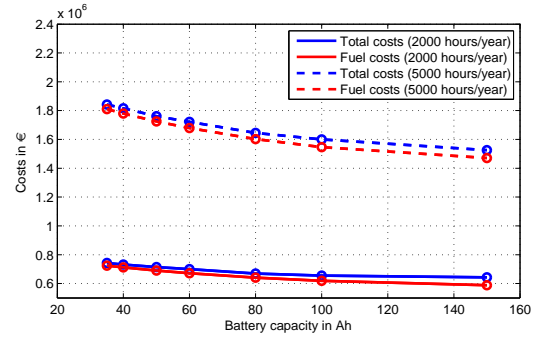
(a) Fuel costs c_{fuel} of 1 €/lit. and battery costs c_{bat} of 200 €/kWh.



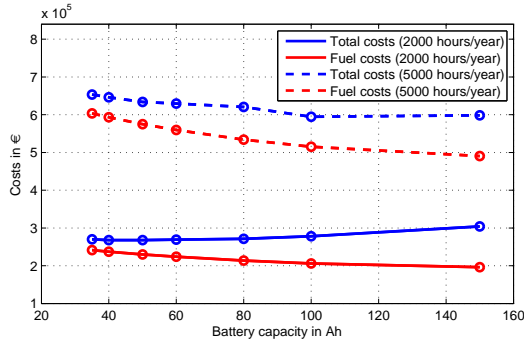
(b) Fuel costs c_{fuel} of 3 €/lit. and battery costs c_{bat} of 200 €/kWh.



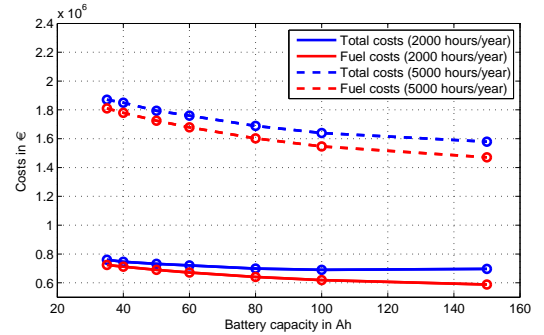
(c) Fuel costs c_{fuel} of 1 €/lit. and battery costs c_{bat} of 500 €/kWh.



(d) Fuel costs c_{fuel} of 3 €/lit. and battery costs c_{bat} of 500 €/kWh.



(e) Fuel costs c_{fuel} of 1 €/lit. and battery costs c_{bat} of 1000 €/kWh.



(f) Fuel costs c_{fuel} of 3 €/lit. and battery costs c_{bat} of 1000 €/kWh.

Figure C.6.: Comparison of life cycle costs c_{life} depending on battery capacity C_{BAT} and operating hours h_{op} for the Orange County bus cycle. The optimal battery capacity C_{BAT} leading to the minimum life cycle costs c_{life} can be determined for different values of fuel costs c_{fuel} and battery costs c_{bat} .

Table C.3.: Share of operating costs c_{op} and life cycle costs c_{life} for given fuel costs c_{fuel} of 1 €/liter and battery costs c_{bat} of 500 €/kWh. The life cycle of the bus is defined by 10 years.

operating costs per cycle for the Manhattan bus cycle					
battery capacity (Ah)	operating hours (h/year)	fuel costs (€)	battery costs (€)	brake costs (€)	total costs (€)
40	2000	2.44	0.21	0.02	2.67
40	5000	2.42	0.17	0.02	2.61
80	2000	2.18	0.34	0.01	2.53
80	5000	2.19	0.17	0.01	2.37

life cycle costs for the Manhattan bus cycle					
battery capacity (Ah)	operating hours (h/year)	fuel costs (k€)	battery costs (k€)	brake costs (k€)	total costs (k€)
40	2000	161.4	14.4	5	180.8
40	5000	400.7	28.8	5	434.5
80	2000	143.9	28.8	5	177.7
80	5000	363.0	28.8	5	396.8

Table C.4.: Share of operating costs c_{op} and life cycle costs c_{life} for given fuel costs c_{fuel} of 2 €/liter and battery costs c_{bat} of 200 €/kWh. The life cycle of the bus is defined by 10 years.

operating costs per cycle for the Manhattan bus cycle					
battery capacity (Ah)	operating hours (h/year)	fuel costs (€)	battery costs (€)	brake costs (€)	total costs (€)
40	2000	4.88	0.08	0.02	4.98
40	5000	4.85	0.07	0.02	4.94
80	2000	4.35	0.13	0.01	4.49
80	5000	4.35	0.08	0.01	4.44

life cycle costs for the Manhattan bus cycle					
battery capacity (Ah)	operating hours (h/year)	fuel costs (k€)	battery costs (k€)	brake costs (k€)	total costs (k€)
40	2000	322.9	5.8	5	333.7
40	5000	801.3	11.5	5	817.8
80	2000	287.8	11.5	5	304.3
80	5000	719.5	17.3	5	741.8

Table C.5.: Share of operating costs c_{op} and life cycle costs c_{life} for given fuel costs c_{fuel} of 1 €/liter and battery costs c_{bat} of 500 €/kWh. The life cycle of the bus is defined by 10 years.

operating costs per cycle for the Orange County bus cycle					
battery capacity (Ah)	operating hours (h/year)	fuel costs (€)	battery costs (€)	brake costs (€)	total costs (€)
40	2000	6.34	0.36	0.06	6.76
40	5000	6.31	0.27	0.06	6.64
80	2000	5.66	0.67	0.03	6.36
80	5000	5.66	0.44	0.03	6.13

life cycle costs for the Orange County bus cycle					
battery capacity (Ah)	operating hours (h/year)	fuel costs (k€)	battery costs (k€)	brake costs (k€)	total costs (k€)
40	2000	238.9	14.4	5	258.3
40	5000	594.5	28.8	10	633.3
80	2000	213.6	28.8	5	247.4
80	5000	534.0	43.2	5	582.2

Table C.6.: Share of operating costs c_{op} and life cycle costs c_{life} for given fuel costs c_{fuel} of 2 €/liter and battery costs c_{bat} of 200 €/kWh. The life cycle of the bus is defined by 10 years.

operating costs per cycle for the Orange County bus cycle					
battery capacity (Ah)	operating hours (h/year)	fuel costs (€)	battery costs (€)	brake costs (€)	total costs (€)
40	2000	12.58	0.17	0.06	12.81
40	5000	12.61	0.11	0.06	12.78
80	2000	11.33	0.27	0.03	11.63
80	5000	11.33	0.18	0.03	11.54

life cycle costs for the Orange County bus cycle					
battery capacity (Ah)	operating hours (h/year)	fuel costs (k€)	battery costs (k€)	brake costs (k€)	total costs (k€)
40	2000	474.6	8.6	5	488.2
40	5000	1189.0	11.5	10	1210.5
80	2000	427.2	11.5	5	443.7
80	5000	1067.9	17.3	5	1090.2

D. Driving Cycles

In Chapter 6 different approaches for optimal energy management were demonstrated with the help of driving cycles, which are the "Braunschweig city driving cycle", the "Manhattan bus cycle" and the "Orange County bus cycle". The corresponding velocity profiles are shown in the following Figures D.1 - D.3.

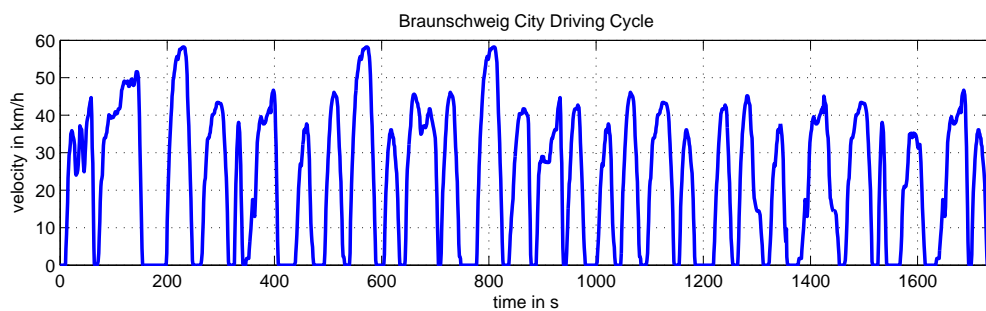


Figure D.1.: Velocity profile of the "Braunschweig city driving cycle".

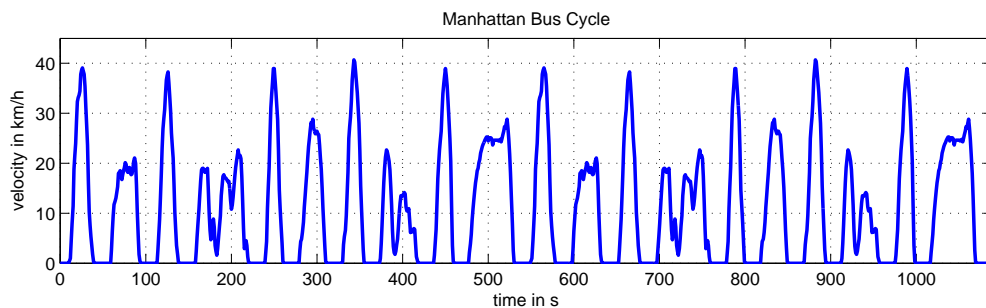


Figure D.2.: Velocity profile of the "Manhattan bus cycle".

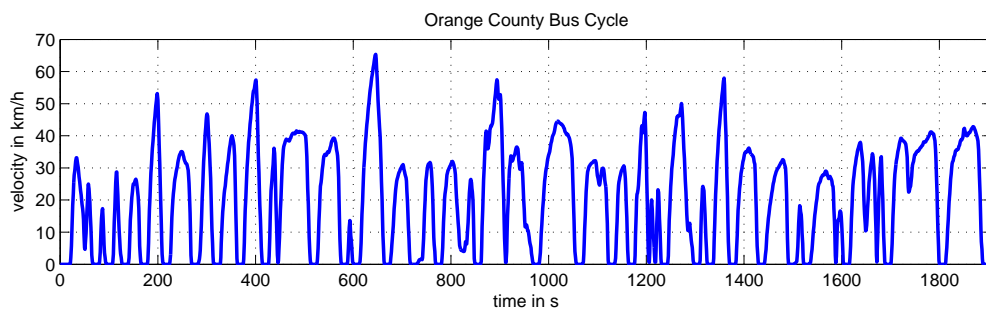


Figure D.3.: Velocity profile of the "Orange County bus cycle".

E. List of Abbreviations

APU	Auxiliary power unit
AUX	Auxiliary devices
CDCS	Charge-depleting / charge-sustaining
COP	Coefficient of performance
CV	Conventional vehicle
CVT	Continuously variable transmission
DDP	Deterministic dynamic programming
DP	Dynamic programming
ECMS	Equivalent consumption minimization strategy
EGU	Engine-generator unit
EM	Electric motor
EV	Electric vehicle
HEV	Hybrid electric vehicle
HJBE	Hamilton-Jacobi-Bellman equation
HV	Hybrid vehicle
ICE	Internal combustion engine
LP	Linear programming
MPC	Model predictive control
NVH	Noise, Vibration, Harshness
PE	Power electronics
PGS	Planetary gear set
PMP	Pontryagin's maximum principle
PWR	Power-to-weight ratio
QP	Quadratic programming
REX	Range extender
RMS	Root mean square
SDP	Stochastic dynamic programming
SOC	State of charge
SOE	State of energy
ZE	Zero-emission

F. List of Symbols

Greek Symbols

Symbol	Unit	Description
α	rad	Road angle
β	.	Weighting factor
γ	-	Discount factor
δ	.	Variation
η	-	Efficiency
λ	.	Co-state
ρ	kg/m ³	Air density
π	.	Control policy
ϑ	°C	Temperature
ϑ_{BAT}	°C	Battery temperature
ϑ_w	°C	Temperature of the windings
ϑ_r	°C	Temperature of the remaining parts
Δ	.	Difference

Sub- / Superscripts

Subscripts		Superscripts	
0	initial	*	optimum
cont	continuous	^	estimation
f	final	.	time derivative
gen	generator	T	transpose
max	maximum	—	mean
min	minimum		
mot	motor		
ref	reference		
tol	tolerance		

Latin Symbols

Symbol	Unit	Description
A	m^2	Frontal area
C	F	Capacitance
C_{BAT}	Ah	Battery capacity
C_{CH}	1/h	C-Rate (charging)
C_{DIS}	1/h	C-Rate (discharging)
C_{SC}	F	Supercap capacitance
C_{STO}	kWh	Storage capacity
$E\{\cdot\}$.	Expected value
E_{BAT}	kWh	Energy content of the battery
E_{FUEL}	kWh	Energy content of the fuel tank
E_{PROP}	kWh	Energy for propulsion
E_{SC}	kWh	Energy content of the supercap
E_{SUM}	kWh	Energy at the summing point
F_A	N	Aerodynamic friction
F_G	N	Force due to gradients
F_R	N	Rolling friction
F_T	N	Traction force
$H(\cdot)$.	Hamiltonian function
H_{LV}	kWh/kg	Lower heating value
I_{BAT}	A	Battery current
I_{CH}	A	Charge current
I_{DIS}	A	Discharge current
I_{EM}	A	Electric motor current
I_{RMS}	A	Root mean square current
J	.	Performance index
$L(\cdot)$.	Cost function
L_{EM}	H	Electric motor inductance
M	Nm	Torque
M_{DEM}	Nm	Torque demand
M_{DEM}	Nm	Total torque demand
N	-	Number of stages
N_{BAT}	-	Number of batteries
N_{BRAKE}	-	Number of brakes
N_{CELLS}	-	Number of battery cells
N_{CYC}	-	Total number of driving cycles
N_{START}	-	Number of engine starts
P_{BAT}	W	Battery power
P_{BRAKE}	W	Braking power
P_{COOL}	W	Continuous cooling power
P_{DEM}	W	Power demand due to the driving cycle
P'_{DEM}	W	Total power demand
P_{ECH}	W	Electrochemical power
P_{EGU}	W	Electrical power of the engine-generator unit
P_{EL}	W	Electrical power

Symbol	Unit	Description
P_{EM}	W	Electric motor power
P_{EQV}	W	Equivalent power
P_F	W	Fuel power
P_{ICE}	W	Engine power
$P_{LOSS,BAT}$	W	Power loss battery
$P_{LOSS,EM}$	W	Power loss electric motor
$P_{LOSS,SC}$	W	Power loss supercap
P_{MECH}	W	Mechanical power
P_{PE}	W	Input power of the power electronics
$P_{R,EM}$	W	Power loss in the remaining parts
P_{TOTAL}	W	Total propulsion power
P_W	W	Power at the wheels
$P_{W,EM}$	W	Power loss in the windings
R_{BAT}	Ω	Internal battery resistance
R_{EM}	Ω	Electric motor resistance
R_{SC}	Ω	Internal supercap resistance
R_{TH}	K/W	Thermal resistance
U	V	Voltage
U_{EMF}	V	Counter-electromotive force
U_{NOM}	V	Nominal voltage
U_{OC}	V	Open-circuit voltage
U_{TERM}	V	Terminal voltage
\mathcal{J}	.	Cost-to-go
\mathcal{O}	-	Complexity
\mathcal{U}	.	Control space
\mathcal{X}	.	State space
c_{bat}	€/kWh	Battery costs per kWh
$c_{comp,bat}$	€	Component costs battery
$c_{comp,brake}$	€	Component costs brake
$c_{comp,egu}$	€	Component costs engine-generator unit
$c_{comp,em}$	€	Component costs electric motor
c_{fuel}	€/liter	Fuel costs per liter
c_{life}	€	Life cycle costs
c_{op}	€	Operating costs
c_{ov}	-	Overload factor
$c_{p,bat}$	J/(kg · K)	Specific heat capacity battery
$c_{p,w}$	J/(kg · K)	Specific heat capacity windings
$c_{p,r}$	J/(kg · K)	Specific heat capacity remaining parts
c_w	-	Drag coefficient
e_c	kWh	Energy consumption
e_{ec}	kWh	Electrical energy consumption
$f(\cdot)$.	System dynamics
f_c	liter	Fuel consumption

Symbol	Unit	Description
f_r	-	Rolling friction coefficient
g	m/s ²	Gravitational acceleration
$h(\cdot)$	·	Weighting function
h_{op}	h/year	Operating hours per year
h_r	-	Hybridization ratio
i_g	-	Ratio of the gear box
k	-	Index of the stage variable
m	kg	Mass
m_{bat}	kg	Battery mass
m_{egu}	kg	Mass of the engine-generator unit
m_r	kg	Mass of the remaining parts
m_{sc}	kg	Supercap mass
m_w	kg	Mass of the windings
\dot{m}_f	kg/s	Mass flow rate of fuel
n	rpm	Speed
n_{cor}	rpm	Corner speed
s	-	Equivalence factor
s_{ch}	-	Equivalence factor (charge mode)
s_{dis}	-	Equivalence factor (discharge mode)
t	s	Time
t_{idle}	s	Idle time
u	·	Control variable
u_s	-	Power-split
x	·	State variable
x_{ice}	-	Additional state variable for the engine
v	m/s	Velocity
\dot{v}	m/s ²	Acceleration
w	·	Disturbances

Bibliography

- [1] D. Ambühl. *Energy Management Strategies for Hybrid Electric Vehicles*. PhD thesis, ETH Zürich, 2009.
- [2] D. Ambühl and L. Guzzella. Predictive Reference Signal Generator for Hybrid Electric Vehicles. *IEEE Transactions on Vehicular Technology*, 58:4730–4740, 2009.
- [3] M. Back. *Prädiktive Antriebsregelung zum energieoptimalen Betrieb von Hybridfahrzeugen*. PhD thesis, Universität Karlsruhe (TH), 2005.
- [4] A. Barré, B. Deguilhem, S. Grolleau, M. Gérard, F. Suard, and D. Riu. A review on lithium-ion battery ageing mechanisms and estimations for automotive applications. *Journal of Power Sources*, 241:680–689, 2013.
- [5] S. Bashash and H. K. Fathy. Optimizing demand response of plug-in hybrid electric vehicles using quadratic programming. In *American Control Conference (ACC)*, pages 716–721, 2013.
- [6] R. E. Bellman. *Dynamic Programming*. Princeton University Press, 1957.
- [7] A. Bemporad, F. Borrelli, and M. Morari. Model predictive control based on linear programming - the explicit solution. *IEEE Transactions on Automatic Control*, 47:1974–1985, 2002.
- [8] D. P. Bertsekas. *Dynamic Programming and Optimal Control*, volume 1. Athena Scientific, 3rd edition, 2005.
- [9] D. P. Bertsekas. *Dynamic Programming and Optimal Control - Approximate Dynamic Programming*, volume 2. Athena Scientific, 4th edition, 2005.
- [10] D. Bianchi, L. Rolando, L. Serrao, S. Onori, G. Rizzoni, N. Al-Khayat, T. Hsieh, and P. Kang. A rule-based strategy for a series/parallel hybrid electric vehicle: an approach based on dynamic programming. In *ASME Dynamic Systems and Control Conference*, pages 507–514, 2010.
- [11] D. Bianchi, L. Rolando, L. Serrao, S. Onori, G. Rizzoni, N. Al-Khayat, T. Hsieh, and P. Kang. Layered control strategies for hybrid electric vehicles based on optimal control. *International Journal of Electric and Hybrid Vehicles*, 3:191–217, 2011.
- [12] R. Biasini, S. Onori, and G. Rizzoni. A near-optimal rule-based energy management strategy for medium duty hybrid truck. *International Journal of Powertrains*, 2:232–261, 2013.
- [13] Brusa, August 17th, 2016. <http://www.brusa.biz/produkte/antrieb.html>.
- [14] Busworld - Industry News, June 2nd, 2015. <http://www.busworld.org/articles/detail/387>.

- [15] E. Camacho and C. Bordons. *Model Predictive Control*. Springer, 2nd edition, 2007.
- [16] E. Cerruto, A. Consoli, A. Raciti, and A. Testa. Fuzzy Logic Based Efficiency Improvement of an Urban Electric Vehicle. In *20th International Conference on Industrial Electronics, Control and Instrumentation*, volume 2, pages 1304–1309, 1994.
- [17] K. T. Chau and Y. S. Wong. Overview of power management in hybrid electric vehicles. *Energy Conversion and Management*, 43:1953–1968, 2002.
- [18] H. Chen, T. N. Cong, W. Yang, C. Tan, Y. Li, and Y. Ding. Progress in electrical energy storage system: A critical review. *Progress in Natural Science*, 19:291–312, 2009.
- [19] Z. Chen, C. C. Mi, J. Xu, X. Gong, and C. You. Energy Management for a Power-Split Plug-in Hybrid Electric Vehicle Based on Dynamic Programming and Neural Networks. *IEEE Transactions on Vehicular Technology*, 63(4):1567–1580, 2014.
- [20] Data sheet Brusa - Asynchronous Motor, April 11th, 2016. http://www.brusa.biz/_files/drive/05_Sales/Datasheets/BRUSA_DB_EN_ASM1.pdf.
- [21] Data sheet Brusa - Hybrid Synchronous Motor, April 11th, 2016. http://www.brusa.biz/_files/drive/05_Sales/Datasheets/BRUSA_DB_EN_HSM1.pdf.
- [22] Data sheet Nesscap, December 16th, 2015. <ftp://218.210.72.90/product/Capacitor/Super%20Cap/Module/EMHSP%2051C0-340R0.pdf>.
- [23] B. de Jager, T. van Keulen, and J. Kessels. *Optimal Control of Hybrid Vehicles*. Advances in Industrial Control. Springer-Verlag London, 2013.
- [24] S. Delprat, T. Guerra, and J. Rimaux. Optimal control of a parallel powertrain: From global optimization to real time control strategy. In *55th Vehicular Technology Conference*, volume 4, pages 2082–2088, 2002.
- [25] e-transportation.eu, Data sheet Kokam, June 3rd, 2015. http://www.e-transportation.eu/catalog/Kokam-SLPB100216216H_40Ah_Grade.pdf.
- [26] S. B. Ebbesen. *Optimal Sizing and Control of Hybrid Electric Vehicles*. PhD thesis, ETH Zürich, 2012.
- [27] P. Elbert. *Noncausal and Causal Optimization Strategies for Hybrid Electric Vehicles*. PhD thesis, ETH Zürich, 2014.
- [28] P. Elbert, S. Ebbesen, and L. Guzzella. Implementation of Dynamic Programming for n -Dimensional Optimal Control Problems With Final State Constraints. *IEEE Transactions on Control Systems Technology*, 21:924–931, 2013.
- [29] Electric bus: Capabus, June 22nd, 2015. <http://electricbbus.blogspot.co.at/2012/05/capabus.html>.
- [30] enstroj.si, Data sheet Kokam, June 3rd, 2015. http://www.enstroj.si/download.php?f=images/stories/tech_spec_slpb100216216h_40ah_a1.pdf.
- [31] Enviro400H Low Floor Hybrid Double Deck Bus, June 2nd, 2015. http://www.alexander-dennis.com/wp-content/uploads/2012/11/e400h_spec_sheet.pdf.

- [32] European Environment Agency - Overview of electricity production and use in Europe, March 21st, 2016. <http://www.eea.europa.eu/data-and-maps/indicators/overview-of-the-electricity-production-1/assessment>.
- [33] Fernando Matia and G. Nicolas Marichal and Emilio Jimenez, editor. *Fuzzy Modeling and Control: Theory and Applications*. Atlantis Press, 1st edition, 2014.
- [34] J. Fuchs, B. Schweighofer, and H. Wegleiter. Cost-optimal Operational Strategies for Hybrid Vehicles. In *3rd International Conference on Energy Efficient Vehicles*, pages 31–40, 2014.
- [35] J. Fuchs, B. Schweighofer, and H. Wegleiter. Optimization of Life Cycle Costs for Hybrid Vehicles. In *11th Symposium: Hybrid and Electric Vehicles*, pages 172–187, 2014.
- [36] H. P. Geering. *Optimal Control with Engineering Applications*. Springer, 2007.
- [37] B. Gu and G. Rizzoni. An adaptive algorithm for hybrid electric vehicle energy management based on driving pattern recognition. In *ASME International Mechanical Engineering Congress and Exposition*, pages 249–258, 2006.
- [38] L. Guzzella and A. Sciarretta. *Vehicle Propulsion Systems*. Springer, 3rd edition, 2013.
- [39] H. Hannoun, D. Diallo, and C. Marchand. Energy Management Strategy for a parallel Hybrid Electric Vehicle using Fuzzy Logic. In *International Symposium on Power Electronics, Electrical Drives, Automation and Motion*, pages 229–234, 2006.
- [40] P. Hofmann. *Hybridfahrzeuge - Ein alternatives Antriebssystem für die Zukunft*. Springer, 2nd edition, 2014.
- [41] International Electrotechnical Commission: TC 2 - Rotating machinery, December 16th, 2015. http://www.iec.ch/dyn/www/f?p=103%3A23%3A0%3A%3A%3A3AFSP_ORG_ID%2CFSP_LANG_ID%3A1221%2C25.
- [42] International Electrotechnical Commission: TC 69 - Electric road vehicles and electric industrial trucks, March 21st, 2016. http://www.iec.ch/dyn/www/f?p=103:30:0::: FSP_ORG_ID,FSP_LANG_ID:1255,25.
- [43] S. Jeon, S. Jo, Y. Park., and J. Lee. Multi-mode driving control of a parallel hybrid electric vehicle using driving pattern recognition. *ASME Journal of Dynamic Systems, Measurement, and Control*, 124:141–149, 2002.
- [44] L. Johannesson, M. Asbogard, and B. Egardt. Assessing the Potential of Predictive Control for Hybrid Vehicle Powertrains using Stochastic Dynamic Programming. *IEEE Transactions on Intelligent Transportation Systems*, 8:71–83, 2007.
- [45] E. Karden, S. Ploumen, B. Fricke, T. Miller, and K. Snyder. Energy storage devices for future hybrid electric vehicles. *Journal of Power Sources*, 168:2–11, 2007.
- [46] G. Karmiris and T. Tengner. Control method evaluation for battery energy storage system utilized in renewable smoothing. In *IECON - 39th Annual Conference of the IEEE*, pages 1566–1570, 2013.

- [47] N. Kim, S. Cha, and H. Peng. Optimal Control of Hybrid Electric Vehicles Based on Pontryagin's Minimum Principle. *IEEE Transactions on Control Systems Technology*, 19:1279–1287, 2011.
- [48] N. Kim, S. W. Cha, and H. Peng. Optimal Equivalent Fuel Consumption for Hybrid Electric Vehicles. *IEEE Transactions on Control Systems Technology*, 20(3):817–825, 2012.
- [49] D. E. Kirk. *Optimal Control Theory: An Introduction*. Prentice-Hall, Englewood Cliffs, 1970.
- [50] M. Koot, J. T. B. A. Kessels, B. de Jager, W. P. M. H. Heemels, P. P. J. van den Bosch, and M. Steinbuch. Energy management strategies for vehicular electric power systems. *IEEE Transactions on Vehicular Technology*, 54:771–782, 2005.
- [51] K. Koprubasi. *Modeling and Control of a Hybrid-Electric Vehicle for Drivability and Fuel Economy Improvements*. PhD thesis, The Ohio State University, 2008.
- [52] T. Kousksou, P. Bruel, A. Jamil, T. El Rhafiki, and Y. Zeraouli. Energy storage: Applications and challenges. *Solar Energy Materials and Solar Cells*, 120:59–80, 2014.
- [53] S. Kutter. *Eine prädiktive und optimierungsbasierte Betriebsstrategie für autarke und extern nachladbare Hybridfahrzeuge*. PhD thesis, TU Dresden, 2013.
- [54] S. Kutter and B. Bäker. Predictive online control for hybrids: Resolving the conflict between global optimality, robustness and real-time capability. In *Vehicle Power and Propulsion Conference*, pages 1–7, 2010.
- [55] S. Kutter and B. Bäker. An iterative algorithm for the global optimal predictive control of hybrid electric vehicles. In *Vehicle Power and Propulsion Conference*, pages 1–6, 2011.
- [56] R. Larson. A survey of dynamic programming computational procedures. *IEEE Transactions on Automatic Control*, 12:767–774, 1967.
- [57] V. Larsson, L. Johannesson, and B. Egardt. Analytic Solutions to the Dynamic Programming Subproblem in Hybrid Vehicle Energy Management. *IEEE Transactions on Vehicular Technology*, 64:1458 – 1467, 2014.
- [58] V. Larsson, L. Johannesson, B. Egardt, and S. Karlsson. Commuter Route Optimized Energy Management of Hybrid Electric Vehicles. *IEEE Transactions on Intelligent Transportation Systems*, 15(3):1145–1154, 2014.
- [59] T. Leroy, F. Vidal-Naquet, and P. Tona. Stochastic Dynamic Programming based Energy Management of HEV's: an Experimental Validation. In *19th World Congress of the International Federation of Automatic Control*, volume 10, pages 7953–7958, 2014.
- [60] C.-C. Lin, H. Peng, and J. W. Grizzle. A Stochastic Control Strategy for Hybrid Electric Vehicles. In *American Control Conference*, volume 5, pages 4710–4715, 2004.
- [61] C.-C. Lin, H. Peng, J. W. Grizzle, and J. Kang. Power management strategy for a parallel hybrid electric truck. *IEEE Transactions on Control Systems Technology*, 11:839–849, 2003.

- [62] R. Luus. *Iterative Dynamic Programming*. Chapman & Hall/CRC, 2000.
- [63] T. M. I. Mahlia, T. J. Saktisahdan, A. Jannifar, M. H. Hasan, and H. S. C. Matseelar. A review of available methods and development on energy storage. *Renewable and Sustainable Energy Reviews*, 33:532–545, 2014.
- [64] MAN Bus International - MAN Lion's City Hybrid, June 3rd, 2015. <http://www.bus.man.eu/global/en/city-buses/man-lions-city-hybrid/overview/Overview.html>.
- [65] M. Matsuishi and T. Endo. Fatigue of Metals Subjected to Varying Stress. In *Japan Society of Mechanical Engineers: Fukuoka, Japan*, pages 37–40, 1968.
- [66] A. Millner. Modeling Lithium Ion Battery Degradation in Electric Vehicles. In *IEEE Conference on Innovative Technologies for an Efficient and Reliable Electricity Supply*, pages 349–356, 2010.
- [67] S. J. Moura, H. K. Fathy, D. S. Callaway, and J. L. Stein. A Stochastic Optimal Control Approach for Power Management in Plug-In Hybrid Electric Vehicles. *IEEE Transactions on Control Systems Technology*, 19:545–555, 2011.
- [68] H. Mukai. Algorithms for multicriterion optimization. *IEEE Transactions on Automatic Control*, 25(2):177–186, 1980.
- [69] Y. L. Murphey, P. Jungme, L. Kiliaris, M. L. Kuang, M. A. Masrur, A. M. Phillips, and W. Qing. Intelligent Hybrid Vehicle Power Control - Part II: Online Intelligent Energy Management. *IEEE Transactions on Vehicular Technology*, 62:69–79, 2013.
- [70] Y. L. Murphey, P. Jungme, C. Zhihang, M. L. Kuang, M. A. Masrur, and A. M. Phillips. Intelligent Hybrid Vehicle Power Control - Part I: Machine Learning of Optimal Vehicle Power. *IEEE Transactions on Vehicular Technology*, 61:3519–3530, 2012.
- [71] M. Musallam and C. M. Johnson. An Efficient Implementation of the Rainflow Counting Algorithm for Life Consumption Estimation. *IEEE Transactions on Reliability*, 61:978–986, 2012.
- [72] C. Musardo, G. Rizzoni, and B. Staccia. A-ECMS: an adaptive algorithm for hybrid electric vehicle energy management. In *44th Conference on Decision and Control and the European Control Conference*, pages 1816–1823, 2005.
- [73] oneelectriccars.com, Active-wheel Michelin, June 22nd, 2015. <http://www.oneelectriccars.com/tag/michelin-active-wheel/>.
- [74] S. Onori, L. Serrao, and G. Rizzoni. Adaptive Equivalent Consumption Minimization Strategy for Hybrid Electric Vehicles. In *Proceedings of the ASME 2010 Dynamic Systems and Control Conference DSCC2010 September 12-15, 2010, Cambridge, Massachusetts, USA*, pages 499–505, 2010.
- [75] G. Paganelli, S. Delprat, T. Guerra, J. Rimaux, and J. Santin. Equivalent consumption minimization strategy for parallel hybrid powertrains. In *55th Vehicular Technology Conference*, volume 4, pages 2076–2081, 2002.

- [76] R. Patil, Z. Filipi, and H. Fathy. Comparison of Supervisory Control Strategies for Series Plug-In Hybrid Electric Vehicle Powertrains Through Dynamic Programming. *IEEE Transactions on Control Systems Technology*, 22(2):502–509, 2014.
- [77] A. Pesaran. Battery thermal models for hybrid vehicle simulations. *Journal of Power Sources*, 110:377–382, 2002.
- [78] G. Pistoia. *Electric and Hybrid Vehicles*. Elsevier, 2010.
- [79] P. Pisu and G. Rizzoni. A Comparative Study of Supervisory Control Strategies for Hybrid Electric Vehicles. *IEEE Transactions on Control Systems Technology*, 15(3):506–518, 2007.
- [80] W. B. Powell. *Approximate Dynamic Programming*. Wiley-Interscience, 2007.
- [81] T. Prachar, A. Pöltenstein, L. Magerl, and S. Winter. Consideration of Different Hybrid Powertrains with the Help of a Model in Longitudinal Dynamic Using DymolaTM. In *SAE World Congress, Detroit, USA*, 2006. 2006-01-1126, SP-2008.
- [82] G. Ren, G. Ma, and N. Cong. Review of electrical energy storage system for vehicular applications. *Renewable and Sustainable Energy Reviews*, 41:225–236, 2015.
- [83] G. Rizzoni and S. Onori. Energy Management of Hybrid Electric Vehicles: 15 Years of Development at the Ohio State University. *Oil & Gas Science and Technology*, 70:41–54, 2015.
- [84] C. Romaus, K. Gathmann, and J. Böcker. Optimal Energy Management for a Hybrid Energy Storage System for Electric Vehicles Based on Stochastic Dynamic Programming. In *Vehicle Power and Propulsion Conference*, pages 1–6, 2010.
- [85] M. Salman, M. Chang, and J. Chen. Predictive Energy Management Strategies for Hybrid Vehicles. In *IEEE Vehicular Power and Propulsion Conference VPPC*, pages 21–25, 2005.
- [86] M. Salman, N. Schouten, and N. Kheir. Control Strategies for Parallel Hybrid Vehicles. In *Proceedings of the American Control Conference*, pages 524–528, 2000.
- [87] F. R. Salmasi. Control Strategies for Hybrid Electric Vehicles: Evolution, Classification, Comparison, and Future Trends. *IEEE Transactions on Vehicular Technology*, 56:2393–2404, 2007.
- [88] C. Schlasza, P. Ostertag, D. Chrenko, R. Kriesten, and D. Bouquain. Review on the aging mechanisms in Li-ion batteries for electric vehicles based on the FMEA method. In *IEEE Transportation Electrification Conference and Expo (ITEC)*, pages 1–6, 2014.
- [89] N. Schouten, M. Salman, and N. Kheir. Fuzzy Logic Control for Parallel Hybrid Vehicles. *IEEE Transactions on Control Systems Technology*, 10:460–468, 2002.
- [90] A. Sciarretta, M. Back, and L. Guzzella. Optimal Control of Parallel Hybrid Electric Vehicles. *IEEE Transactions on Control Systems Technology*, 12:352–363, 2004.
- [91] A. Sciarretta and L. Guzzella. Control of hybrid electric vehicles. *IEEE Control Systems*, 27:60–70, 2007.

- [92] L. Serrao. *A Comparative Analysis of Energy Management Strategies for Hybrid Electric Vehicles*. PhD thesis, The Ohio State University, 2009.
- [93] L. Serrao, S. Onori, and G. Rizzoni. ECMS as a realization of Pontryagin's minimum principle for HEV control. In *American Control Conference (ACC09)*, pages 3964–3969, 2009.
- [94] L. Serrao, S. Onori, and G. Rizzoni. A Comparative Analysis of Energy Management Strategies for Hybrid Electric Vehicles. *Journal of Dynamic Systems, Measurement, and Control*, 133:115–124, 2011.
- [95] L. Serrao, S. Onori, A. Sciarretta, Y. Guezennec, and G. Rizzoni. Optimal energy management of hybrid electric vehicles including battery aging. In *American Control Conference*, pages 2125–2130, 2011.
- [96] Siemens-SIMOTICS M-1PH8 Main Motor Configuration Manual, April 11th, 2016. https://cache.industry.siemens.com/dl/files/744/46484744/att_37319/v1/PH8S_0512_en_en-US.pdf.
- [97] Siemens Technology for the Environment, June 22nd, 2015. http://www.siemens.com/innovation/en/publikationen/publications_pof/pof_spring_2007/technology_for_the_environment/green_transportation.htm.
- [98] M. F. Stapelbroek. *Optimal Betriebsstrategie für Hybridfahrzeuge unter Berücksichtigung homogenisierter Brennverfahren*. PhD thesis, RWTH Aachen, 2012.
- [99] G. Steinmayer and L. del Re. Optimal control of dual power sources. In *IEEE International Conference on Control Applications (CCA)*, pages 422–427, 2001.
- [100] M. Sugeno. On stability of fuzzy systems expressed by fuzzy rules with singleton consequents. *IEEE Transactions on Fuzzy Systems*, 7:201–224, 1999.
- [101] O. Sundström. *Optimal Control and Design of Hybrid-electric Vehicles*. PhD thesis, ETH Zürich, 2010.
- [102] H. Tamaki, H. Kita, and S. Kobayashi. Multi-objective optimization by genetic algorithms: a review. In *Proceedings of IEEE International Conference on Evolutionary Computation, Nagoya*, pages 517–522, 1996.
- [103] M. A. Tankari, M. B. Camara, B. Dakyo, and G. Lefebvre. Use of Ultracapacitors and Batteries for Efficient Energy Management in Wind-Diesel Hybrid System. *IEEE Transactions on Sustainable Energy*, 4:414–424, 2013.
- [104] E. Tate and S. Boyd. Finding Ultimate Limits of Performance for Hybrid Electric Vehicles. In *Future Transportation Technology Conference*, pages 1–14, 2000.
- [105] M. A. L. Thathachar and P. Viswanath. On the stability of fuzzy systems. *IEEE Transactions on Fuzzy Systems*, 5:145–151, 1997.
- [106] P. R. Thie and G. E. Keough. *An Introduction to Linear Programming and Game Theory*. John Wiley & Sons, 2008.
- [107] F. Tianheng, Y. Lin, G. Qing, H. Yanqing, Y. Ting, and Y. Bin. A Supervisory Control Strategy for Plug-In Hybrid Electric Vehicles Based on Energy Demand Prediction and Route Preview. *IEEE Transactions on Vehicular Technology*, 64:1691–1700, 2015.

- [108] J. Todorović, Č. Duboka, and Ž. Arsenić. Operational life expectancy of rubbing elements in automotive brakes. *Tribology International*, 28:423–432, 1995.
- [109] E. Vinot, R. Trigui, Y. Cheng, C. Espanet, A. Bouscayrol, and V. Reinbold. Improvement of an EVT-Based HEV Using Dynamic Programming. *IEEE Transactions on Vehicular Technology*, 63(1):40–50, 2014.
- [110] Volvo buses: Volvo hybrid driveline, June 2nd, 2015. <http://www.volvobuses.com/SiteCollectionDocuments/VBC/Downloads/Volvo-D5K-Hybrid-Euro6-Fact-Sheet-EN.pdf>.
- [111] Vossloh-Kiepe, June 22nd, 2015. <http://vossloh-kiepe.at/electric-buses/hybrid-buses>.
- [112] H.-G. Wahl, K.-L. Bauer, F. Gauterin, and M. Holzäpfel. A Real-time Capable Enhanced Dynamic Programming Approach for Predictive Optimal Cruise Control in Hybrid Electric Vehicles. In *16th International Conference on Intelligent Transportation Systems*, pages 1662–1667, 2013.
- [113] H.-G. Wahl, M. Holzäpfel, and F. Gauterin. Approximate Dynamic Programming Methods Applied to Far Trajectory Planning in Optimal Control. In *Intelligent Vehicles Symposium*, pages 1085–1090, 2014.
- [114] H. Wegleiter. Comparison of energy storages for automotive applications. Internal document of the Institute of Electrical Measurement and Measurement Signal Processing.
- [115] S. S. Williamson. *Energy Management Strategies for Electric and Plug-in Hybrid Electric Vehicles*. Springer, 2013.
- [116] S. G. Wirasingha and A. Emadi. Classification and Review of Control Strategies for Plug-In Hybrid Electric Vehicles. *IEEE Transactions on Vehicular Technology*, 60:111–122, 2011.
- [117] S. You, J. Hu, A. B. Pedersen, P. B. Andersen, C. N. Rasmussen, and S. Cha. Numerical comparison of optimal charging schemes for Electric Vehicles. In *IEEE Power and Energy Society General Meeting*, pages 1–6, 2012.
- [118] S. You and C. N. Rasmussen. Generic modelling framework for economic analysis of Battery Systems. In *IET Conference on Renewable Power Generation*, pages 1–6, 2011.
- [119] R. Zhang and Y. Chen. Control of hybrid dynamical systems for electric vehicles. In *American Control Conference*, volume 4, pages 2884–2889, 2001.
- [120] X. Zhang and C. Mi. *Vehicle Power Management*. Springer, 2011.
- [121] Y. Zhu, Y. Chen, G. Tian, H. Wu, and Q. Chen. A Four-Step Method to Design an Energy Management Strategy for Hybrid Vehicles. In *American Control Conference*, volume 1, pages 156–161, 2004.